

III-N blue-emitting epi-structures with high densities of dislocations: Fundamental mechanisms for efficiency improvement and applications

Présentée le 12 avril 2024

Faculté des sciences de base
Laboratoire en semiconducteurs avancés pour la photonique et l'électronique
Programme doctoral en physique

pour l'obtention du grade de Docteur ès Sciences

par

Pierre Christophe LOTTIGIER

Acceptée sur proposition du jury

Prof. L. Villard, président du jury
Prof. N. Grandjean, directeur de thèse
Prof. F. Bertram, rapporteur
Dr F. Semond, rapporteur
Dr A. Hessler-Wyser, rapporteuse

Par tous ses défis,
la Vie enseigne l'équilibre :
c'est une arête effilée
et un laboratoire de Bonheur.
— P. L.

To Nature ...
À ma Belle D'Âme ...

Acknowledgements

Choosing the right place to pursue doctoral studies in Physics can be as complex as finding the most adapted itinerary on the Miroir d'Argentine. All this started during a Master's lesson about light-matter interaction in semiconductor nanostructures, where I saw the name of LASPE (ALPES?) for the first time — here I can thank Pr. Jacqueline Bloch for my discovery of the laboratory. I would like to thank Nicolas and Raphaël for having proposed a videocall after my spontaneous e-mail contact, which led to an in-person interview at EPFL. Thank you for having believed in me and for hiring me in the team. This led to the precise evaluation of my work by jury members Prof. Frank Bertram, Dr. Aïsha Hessler-Wyser, Dr. Fabrice Semond and Prof. Laurent Villard, to whom I express my gratitude.

I need to thank cheerfully all the staff of CMi and III-V cleanrooms and CIME; without you, this work would have been impossible: Zdenek, Nicolas L., Damien, Yoan, Adrien, Duncan, and all the others. Necessarily, thank you Jean-François for your world-class expertise in growing samples and discussing so sympathetically at your pause-clope. Thank you, François and Nadja, for your humanity.

A glorious team, with such a good mood and balance of competencies: thank you Camille, Gordon, Mayeul, Pirouz, Sebastian, Szymon, the super postdocs with always good advice about the Sat beers and the photoluminescence lasers of choice. Thank you Davide, for the brightness you brought to the optic labs when you helped me with tough measurements! and along the everyday life of a PhD path, sometimes underwater, sometimes memorably singing. Thank you my fellow PhD colleagues from the other room, Danxuan, Thomas, Yao, you were always there when I had interrogations, when I needed help for specific measurements (*e.g.*, cathodoluminescence) on weird samples or to share *enjoyable* lunchtimes. Thank you Guillaume, working with you brought its dose of joy, efficient engineering and cookies. I would also like to thank the interns and students I supervised, for their commitment. To Samuele, Alexandros and Anna, thank you for the fresh air you bring; I wish you all the best for the coming years. Thank you Hoda for the amazing ideas and organisations of get-togethers; you made yourself an inevitable social joint of the lab! Of course, even though I might have had enough of your face across my desktop, I will thank you too, Johann, for the amazing friendship we built through these four years — I won't forget all the games, the *a capella* choruses and all the random (more or less scientific but always insightful) conversations at nanopresso- or beer-time. Dear colleagues, I can proudly call you my friends.

Merci Nicolas pour tes conseils et points de vue avisés, qui m'ont enseigné plus que simplement la science des nitrures. Merci du fond du coeur pour ta sensibilité, ta compréhension et

Acknowledgements

ton soutien pendant ces années de thèse. J'ai trouvé un vrai manager scientifique, et mieux : un précieux *mentor*.

J'ai croisé trop de personnes géniales qui ont pris part à mon chemin de doctorant, mais je vais tenter de mentionner alphabétiquement au moins ceux qui risquent de lire cette partie de ma thèse. Merci les amis de Toulouse et d'avant, Benoît, Cloé, Eloa, Guillem, Jamie, Quentin, Sarah, Selim, Thomas, Vénice, Victor, pour ce long et beau chemin d'amitié. Merci l'Infini ! Alexis, Pierre *aka*. Pidel, Vincent *aka*. Pasto, toujours au rendez-vous ! Bien sûr, les Vikings, Jack et Marion ! merci pour nos belles aventures. Les journées dehors avec le Club Alpin entre autres, c'est autant de lumière qui m'a animé ces années : merci Antonin, Antonin, Alberto, Bru, Chloé, Christian, Colin, Eduardo, Héloïse, Jérémie, Lorenz, Martino, Pierre, Rebekah, Sébastien, Susy, Tobias, Valenvol, et *cie*. pour la joie partagée. Merci aussi aux colocs Omblin et Stan pour de chouettes moments de confiance. Un grand merci aussi Bruno, Daniel, Laurence, Marie, Romain, et les amis et famille, pour votre très bel accueil, ouvert et chaleureux.

Papi, je sais que d'où tu es, tu es fier de moi : merci d'avoir toujours cru en moi. Mamie, merci pour ton esprit affectueux qui ne cesse de m'enchanter. Maman, merci pour ton soutien indéfectible et si généreux; merci de m'avoir donné tes outils d'artiste pour ouvrir mon regard sur l'univers. Papa, je pense que les devoirs laborieux jusqu'à minuit (et au-delà) et les raids pyrénéens nocturnes ont porté leurs fruits. Merci pour tout ce que tu m'as appris — y compris lorsque tu râlais parce que je démontais toujours tout sur mon bureau ou dans ton atelier — et pour avoir cultivé ma propre sensibilité au monde. Merci Céleste pour tes belles aquarelles et ton affection vigilante, et, surtout, pour nos quatre-cent coups. Adèle, nos conversations et balades sont toujours des moments intenses et adorables, merci pour notre relation si sincère. Alvar, merci d'être là, simplement, avec ta tête sur les (solides) épaules et ton sourire au milieu, tu es le frère pour moi.

Merci à toi Margaux, avec qui je peux partager mes plus grandes joies et mes plus grandes peines — et bien plus que cela. Je chéris notre connection ontologique, qui a rendu ma vie de doctorant si chatoyante et m'offre le bonheur. Merci ma Belle D'Âme.

Lausanne, March 1, 2024

P. L.

Abstract

Since the dawn of humanity, human beings sought to light their surroundings for their well-being, security and development. The efficiency of ancient lighting devices, *e.g.* oil lamps or candles, was in the order of 0.03–0.04% and jumped to 0.4–0.6% with the use of gas during the first industrial revolution. Electricity allowed to reach 3–4% efficiency with incandescent bulbs, which contextualises the importance taken by III-nitrides (III-Ns) when > 10% external quantum efficiency (EQE) light-emitting diodes (LEDs) were first demonstrated in the 1990s. Nowadays, this technology is mature and state-of-the-art devices show > 80% EQE. This was only made possible through multidisciplinary research in the fields of semiconductor materials science, optics and photonics, and electronics. Of high interest is that such high efficiencies were obtained after numerous trial-and-error growth iterations, and we are still on the way to understand the intricacies of the underlying physics.

For the present work, we choose the Si(111) platform to grow thin III-N epilayers containing blue-emitting InGaN/GaN quantum wells (QWs). These systems present high threading dislocation (TD) densities > 10^{10} cm^{-2} which make them an ideal testbed for investigating the impact of point defects (PDs) *versus* TDs on the internal quantum efficiency. By using the common In-containing underlayer mitigation strategy of burying the deleterious PDs below the QW, we have control on their density in the active region. We first perform various mesoscopic photoluminescence (PL) measurements giving quantitative and comparative efficiency assessments for samples with and without a consequent density of $\sim 10^9 \text{ cm}^{-2}$ PDs. Our findings emphasize the importance of these defects, even when the TD density outpaces the PD density by one order of magnitude.

We then employ high resolution ($\sim 60 \text{ nm}$) cathodoluminescence (CL) tools to investigate the detrimental impact of PDs at the nanoscale. As suggested by scanning electron and atomic force microscopy, we discover that instead of being infinite two-dimensional landscapes featuring random energy variations, QWs are concatenated growth grain domains. This new, nuanced view was confirmed by time-resolved CL measurements, offering a deeper insight into the physical processes at play in InGaN/GaN QW.

We finally design and fabricate applicative demonstrator devices such as suspended membrane photonic crystal nanobeam lasers and microcavity LEDs, paving the way toward efficient and versatile integrated silicon photonics.

The outcomes of this work enlighten the impact of point defects in the regime of high dislocation density. By delving deeper into this unexpected finding, nanoscale studies and experiments reshape our understanding of quantum well properties.

Zusammenfassung

Seit den Anfängen der Menschheit haben die Menschen versucht, ihre Umgebung zu beleuchten, um ihr Wohlbefinden, ihre Sicherheit und ihre Entwicklung zu fördern. Der Wirkungsgrad alter Beleuchtungsvorrichtungen, z. B. Öllampen oder Kerzen, lag in der Größenordnung von 0,03 bis 0,04% und stieg mit der Verwendung von Gas während der ersten industriellen Revolution auf 0,4 bis 0,6% an. Strom ermöglichte eine Effizienz von 3–4% mit Glühlampen, was die Bedeutung von III-Nitrid (III-N) in den 1990er Jahren unterstreicht, als erstmals Leuchtdiode (LEDs) mit einer externen Quanteneffizienz (EQE) von $> 10\%$ gezeigt wurden. Heutzutage ist diese Technologie ausgereift und die modernsten Geräte weisen $> 80\%$ EQE auf. Dies war nur durch multidisziplinäre Forschung in den Bereichen Halbleitermaterialien, Optik und Photonik sowie Elektronik möglich. Besonders interessant ist, dass diese hohen Wirkungsgrade nach zahlreichen Versuch-und-Irrtum-Iterationen erreicht wurden und wir immer noch auf dem Weg sind, die Feinheiten der zugrunde liegenden Physik zu verstehen.

Für die vorliegende Arbeit haben wir die Si(111)-Plattform gewählt, um dünne III-N-Epilayer mit blau emittierenden InGaN/GaN Quantenbrunnen zu züchten. Diese Systeme weisen hohe durchwachsende Versetzungen DV-Dichten $> 10^{10} \text{ cm}^{-2}$ auf, die sie zu einem idealen Testfeld für die Untersuchung der Auswirkungen von Punktdefekten (PD) *versus* DV auf die interne Quanteneffizienz. Durch die Anwendung der üblichen In-haltigen Unterschicht Strategie zur Abschwächung von Defekten, die darin besteht, die schädlichen PD unter den Quantenbrunnen zu vergraben, haben wir die Kontrolle über ihre Dichte im aktiven Bereich. Wir führen zunächst verschiedene mesoskopische Photolumineszenz-Messungen durch, die quantitative und vergleichende Effizienzbewertungen für Proben mit und ohne eine konsequente Dichte von $\sim 10^9 \text{ cm}^{-2}$ PD liefern. Unsere Ergebnisse unterstreichen die Bedeutung dieser Defekte, selbst wenn die DV-Dichte die PD-Dichte um eine Größenordnung übersteigt.

Anschließend setzen wir hochauflösende ($\sim 60 \text{ nm}$) Kathodolumineszenz-Werkzeuge ein, um die schädlichen Auswirkungen von PD auf der Nanoskala zu untersuchen. Wie von der Rasterelektronen- und Rasterkraftmikroskopie nahegelegt, entdecken wir, dass Quantenbrunnen keine unendlichen zweidimensionalen Landschaften mit zufälligen Energievariationen sind, sondern verkettete Wachstumskorndomänen. Diese neue, nuancierte Sichtweise wurde durch zeitlich aufgelösten Kathodolumineszenz-Messungen bestätigt und bietet einen tieferen Einblick in die physikalischen Prozesse, die in InGaN/GaN Quantenbrunnen ablaufen.

Schliesslich entwerfen und fertigen wir anwendungsorientierte Demonstrationsbauteile wie Nanobeam-Laser mit photonischen Kristallen und Mikrokavität-LEDs, die den Weg zu einer effizienten und vielseitigen integrierten Silizium-Photonik ebnen.

Zusammenfassung

Die Ergebnisse dieser Arbeit erhellen die Auswirkungen von Punktdefekten im Bereich hoher Versetzungsdichte. Durch die Vertiefung dieser unerwarteten Entdeckung können Studien und Experimente im Nanomaßstab unser Verständnis der Eigenschaften von Quantenbrunnen neu gestalten.

Résumé

Depuis l'aube de l'humanité, les êtres humains ont cherché à éclairer leurs alentours afin d'assurer leur bien être, leur sécurité ainsi que leur développement. L'efficacité des techniques d'éclairages, comme par exemple lampes à huile ou bougies, était autour de 0.03–0.04% et a bondi aux alentours de 0.4–0.6% avec l'apparition de lampes à pétrole lors de la première révolution industrielle. Grâce à la découverte de l'électricité, des efficacités lumineuses ont atteint les 3–4% pour les ampoules halogènes. Dans ce contexte, les années 1990 voient l'avènement de sources de lumière bleue à base de nitrures d'éléments III (III-N) dont l'efficacité quantique externe (EQE) dépasse les 10%, ce qui explique l'engouement pour ces matériaux. De nos jours, cette technologie est mûre et porte ses fruits puisque des valeurs d' $EQE > 80\%$ sont couramment mesurées. Ces jalons ne furent atteints que grâce à une recherche multidisciplinaire à la croisée de la science des matériaux, de l'optique et la photonique, et de l'électronique. Il est d'intérêt notable le fait que de telles efficacités aient pu être atteintes *via* de nombreuses itérations d'essai-erreur de croissances de matériaux, ce qui explique que nous soyons toujours dans une logique de compréhension des mécanismes physiques sous-jacents. Pour les présents travaux, nous avons choisi pour plateforme des couches de III-N hétéroépitaxiées sur substrats de Si(111), contenant des puits quantiques (PQ) InGaN/GaN émettants dans la partie bleue du spectre visible. Ces systèmes présentent de hautes densités de dislocations traversantes (DT) ($> 10^{10} \text{ cm}^{-2}$), ce qui en fait une plateforme expérimentale idéale pour étudier l'impact des défauts ponctuels (DP) *versus* DT sur l'efficacité quantique interne. En faisant croître une sous-couche contenant de l'In avant la région active pour y piéger les DP, nous pouvons réduire drastiquement leur concentration dans les PQ. Nous commençons par effectuer des mesures mésoscopiques de photoluminescence (PL) afin d'obtenir des quantifications relatives de l'efficacité d'échantillons avec et sans cette concentration conséquente de $\sim 10^9 \text{ cm}^{-2}$ DP. Nous démontrons l'impact important de ces défauts, bien que leur densité soit un ordre de grandeur inférieure à celle des DT.

Dans un deuxième temps, nous appliquons des techniques de cathodoluminescence (CL) à haute résolution ($\sim 60 \text{ nm}$) afin d'explorer l'activité nanoscopique des DP. En accord avec nos mesures de morphologie par microscopies à balayage électronique et à force atomique, nous découvrons qu'au lieu d'être des espaces infinis à deux dimensions, les PQs sont en réalité un assemblage de domaines, délimités par les frontières de grains de croissance. Cette nouvelle vision est confirmée par des mesures de CL résolue en temps, offrant une perception plus profonde des phénomènes physiques en jeu dans les PQ InGaN/GaN.

Finalement, nous concevons, optimisons et fabriquons des dispositifs tels que des lasers à cris-

Résumé

taux photoniques unidimensionnels, ainsi que des diodes électroluminescentes à microcavité. Ces démonstrateurs jalonnent désormais le chemin du domaine d'avenir de la photonique intégrée sur silicium.

En résumé, ce travail met en lumière l'impact crucial des défauts ponctuels dans le régime de haute densité de dislocations; dans notre quête de compréhension de leurs mécanismes inhérents, nous avons découvert par sérendipité la réalité à l'échelle nanométrique des propriétés optiques et électroniques des puits quantiques à haute densité de dislocations.

List of acronyms and symbols

Acronyms

AFM atomic force microscopy	MBE molecular beam epitaxy
A-M Auger-Meitner	MOCVD metal-organic chemical vapour deposition
BF bright-field	MQW multiple quantum well
BSE backscattered electron	NRC nonradiative recombination center
CAD computer assisted design	PD point defect
CL cathodoluminescence	PhC photonic crystal
CW continuous-wave	PL photoluminescence
DBR distributed Bragg reflector	PML perfectly matched layer
DF dark-field	QCSE quantum-confined Stark effect
DH double heterostructures	QW quantum well
DOF depth of focus	RCLED resonant cavity light-emitting diode
EBL e-beam lithography	SD surface defect
EL electroluminescence	SE secondary electron
EQE external quantum efficiency	SEM scanning electron microscopy
FDTD finite-difference time-domain	SL superlattice
FEG field emission gun	SQW single quantum well
FIB focused ion beam	SRH Shockley-Read-Hall
FWHM full width at half maximum	TD threading dislocation
HSQ hydrogen silsesquioxane	TE transverse electric
III-N III-nitride	TEM transmission electron microscopy
IQE internal quantum efficiency	TRPL time-resolved PL
IR infra-red	UL underlayer
LD laser diode	UV ultra-violet
LED light-emitting diode	

Symbols

Π_{exc} excitation irradiance	ϕ_e electron wavefunction
n excess carrier density	ϕ_h hole wavefunction
C ABC C coefficient	P total polarisation
A ABC A coefficient	σ^+ positive charge sheet
B ABC B coefficient	σ^- negative charge sheet
Q quality factor	F_{QW} QW electric field
\mathbf{c} crystallographic axis	$\boldsymbol{\sigma}_{\mathbf{p}}$ charge sheet vector
P_{sp} spontaneous polarisation	ϵ_0 vacuum permittivity
x group-III fraction (usually In)	ϵ_r relative permittivity
ϵ strain	q elementary charge constant
a_s substrate lattice constant	N_{loc} 3D localisation center density
a_l layer lattice constant	E_{loc} localisation energy
\mathbf{b} Burgers vector	D carrier diffusivity
\mathbf{a} crystallographic axis	τ total carrier lifetime
a lattice constant	d number of dimensions
E_{F} Fermi level	L_{D} carrier diffusion length
[SD] 2D surface defect concentration	σ_n point defect (PD) capture cross-section for electrons
R_{GaN} surface defect GaN segregation fraction	σ_p PD capture cross-section for holes
p surface-defect-In interaction efficiency	ΔE_{cap} energy barrier for carrier capture by PD
E_{V} valence band energy	R_{SRH} Shockley-Read-Hall (SRH) recombination rate
E_{C} conduction band energy	N_{PD} 3D PD density
Γ center of the Brillouin zone	v_n electron thermal velocity
E_{g} bandgap	v_p hole thermal velocity
α Varshni coefficient	v carrier thermal velocity
T temperature	σ PD capture cross-section
β Varshni coefficient	τ_{SRH} carrier SRH lifetime
L_{QW} quantum well (QW) thickness	R_{R} radiative recombination rate
L epilayer thickness	R_{AM} Auger-Meitner recombination rate
λ_{DB} De Broglie wavelength	τ_{R} carrier radiative lifetime
\hbar reduced Planck constant	η_{int} internal quantum efficiency (IQE)
m_{e^*} electron effective mass	η_{inj} injection efficiency
k wavevector	η_{extr} light extraction efficiency
x lateral direction (in QW plane)	η external quantum efficiency (EQE)
y lateral direction (in QW plane)	n refractive index
$E_{\text{g, QW}}$ QW material bandgap	k_0 vacuum wavevector
$E_{\text{ph, min}}$ minimum photon energy	λ_0 vacuum wavelength
e electron confinement energy	θ incidence angle
h hole confinement energy	
f_{osc} oscillator strength	

List of acronyms and symbols

ω light pulsation c light speed \mathcal{A} Airy function ζ antinode factor n_{ext} refractive index of the external medium θ_c critical angle m_c cavity order λ light wavelength δ cavity detuning δ_{opt} optimal cavity detuning N_A p -type dopant concentration N_D n -type dopant concentration V_D p - n junction built-in potential k_B Boltzmann constant n_i intrinsic carrier density J current density D_p hole diffusivity τ_p hole carrier lifetime D_n electron diffusivity τ_n electron carrier lifetime η_i ideality factor NA numerical aperture r minimal distance between resolvable points h Planck constant p_e electron momentum E_b electron beam energy m_0 electron rest mass V_{acc} Acceleration voltage $d_{V\text{-pit}}$ V-pit diameter	$N_{V\text{-pit}}$ 2D V-pit density N_{TD} 2D threading dislocation (TD) density \mathbf{g} diffraction vector E_{PL} photoluminescence (PL) emission energy $T_{\text{del, i}}$ delocalisation initial temperature $T_{\text{del, f}}$ delocalisation final temperature W_0 beam waist λ_{exc} excitation laser wavelength M^2 beam propagation ratio z_0 Rayleigh length I_{PL} PL luminescence intensity Π_{max} Π_{exc} at maximum IQE γ_{conv} Π_{exc} to n conversion k empirical C to A coupling E_a SRH nonradiative recombination centers (NRCs) activation energy τ_{eff} luminescence effective lifetime τ_{NR} carrier nonradiative lifetime G_{QW} carrier generation rate in the QW I_p cathodoluminescence (CL) probe current t time $g^{(2)}$ second-order correlation function V optical mode volume β spontaneous emission coupling factor f focal length Ω_{det} detected solid angle $\delta\Omega$ elementary solid angle S_{LED} light-emitting diode (LED) surface i current
---	---

Contents

Acknowledgements	i
Abstract (English/Français/Deutsch)	iii
List of acronyms and symbols	ix
Introduction	1
1 Background information	5
1.1 III-nitrides	5
1.1.1 Structural and polarisation properties	5
1.1.2 Optical properties	10
1.2 Quantum well	12
1.3 Localisation in quantum wells	15
1.4 ABC model	17
1.5 Microcavity effects	23
1.5.1 Fabry-Perot cavity	23
1.5.2 Transmission of a Fabry-Perot cavity	23
1.5.3 Fabry-Perot cavity with an embedded light source	24
1.5.4 Light extraction and cavity order	25
1.5.5 Detuning	27
1.6 Electrical injection	28
1.7 Current understanding of InGaN quantum well efficiency	29
1.7.1 Threading dislocations and V-pits in bulk materials	29
1.7.2 Localisation in InGaN as a threading dislocation protection	30
1.7.3 Threading dislocations and V-pits in InGaN quantum wells	30
1.7.4 Threading dislocations and V-pits in devices	31
2 Sample fabrication and basic properties	33
2.1 Growth	33
2.2 Structural properties	35
2.2.1 Scanning electron microscopy	35
2.2.2 Transmission electron microscopy	38
2.2.3 Atomic force microscopy	41

Contents

2.3	Optical properties	42
2.3.1	Experimental method	42
2.3.2	Photoluminescence mapping	44
2.3.3	Temperature-dependent PL	45
3	Impact of the underlayer on InGaN QWs grown on Si	49
3.1	Power-dependent photoluminescence	49
3.1.1	Setup description	49
3.1.2	Measurement challenges for sample comparison	53
3.1.3	Temperature dependence of the power-dependent measurements	54
3.2	Results and discussion	55
3.2.1	Semi-quantitative considerations	55
3.2.2	Quantitative ABC modelling	58
3.3	Time-resolved photoluminescence	61
4	Nanoscale optical properties of InGaN quantum wells	65
4.1	Cathodoluminescence	65
4.1.1	Experimental method	65
4.1.2	Cathodoluminescence mappings	67
4.1.3	Carrier domain simulations	72
4.1.4	Spatially resolved cathodoluminescence and associated carrier lifetimes	74
4.2	Discussion	75
5	GaN on Si photonic devices	77
5.1	Nanobeams	77
5.1.1	Growth	78
5.1.2	Photonic crystal simulation	80
5.1.3	Clean-room fabrication	80
5.1.4	Micro-photoluminescence	82
5.2	Thin buffer LEDs	84
5.2.1	Growth	84
5.2.2	Clean-room fabrication	87
5.2.3	Electroluminescence	88
	Conclusion	93
	Appendices	97
A	μ PL setup	97
B	Process flow: Photonic Crystals	99
C	Process flow: LEDs	104
D	Sample list	111
	Bibliography	113

Curriculum Vitae

Introduction

After centuries of research aimed at improving the efficiency of lighting, a groundbreaking technology has been introduced with the invention of bright, candela-class III-nitride (III-N) blue-emitting light-emitting diodes (LEDs)[1], based on InGaN/GaN quantum wells (QWs). Although heteroepitaxially grown on c-plane sapphire substrates — which caused the apparition of threading dislocation (TD) densities $> 10^9 \text{ cm}^{-2}$ — these QWs exhibited exceptional efficiencies.[2–4] This observation was somehow surprising, as it had been previously observed that TD densities as low as 10^3 cm^{-2} caused a tenfold efficiency decrease in AlGaInP LEDs[3] and GaAs devices.[5, 6] In this historical consideration of TDs as main nonradiative recombination centers (NRCs), extensive research delved into their role in the decrease of efficiency.[7, 8] The relative insensitivity of InGaN/GaN QWs to TDs has been tentatively explained by two mechanisms: First, the random alloy potential fluctuations in the QWs could create localisation centers for carriers, thereby limiting their diffusion toward NRCs.[9, 10] Second, the formation of V-shaped pits from TDs could generate a potential barrier around them, which would screen NRCs. On the other hand, other defects, such as crystallographic point defects (PDs) or impurities, can also degrade the QW efficiency; correlatively recent studies have pointed out their importance in the degradation of the QW performance.[11, 12] This question of the activity of TDs and PDs is an ongoing debate, to which the present work aims to add new perspectives.

To do this, we must find a method to tailor the PD density in InGaN/GaN QWs. Hopefully, the defects generated at the GaN surface during high-temperature growth tend to be incorporated when an In-containing layer is grown, which would explain why InGaN QWs can become plagued by NRCs if no mitigation strategy is undertaken.[12–14] It was demonstrated that growing InAlN or InGaN underlayers (ULs) before the growth of the active region allows to bury defects, thereby greatly enhancing the efficiency of the QWs.[11, 15, 16] These experiments have shed light on the practical way to reduce PD densities in high-quality InGaN/GaN QW LEDs.

In the present study, our approach to investigate the relative impact of TDs and PDs is to generate on purpose TD densities as high as $\sim 2 \times 10^{10} \text{ cm}^{-2}$ by heteroepitaxially growing the epilayers on Si(111) substrates. In this way, the TD density can exceed the PD density by one order of magnitude in samples with no UL,[12, 14] providing a testbed of choice for the intended study.

Introduction

After the description of the scientific background, this thesis is articulated around three main axes, and ends with photonic devices:

- **Chapter 1: Background information** is provided in order to settle the necessary foundations to understand the work of the present thesis. After describing the III-N materials family, we present both the electrical and optical properties of InGaN/GaN QWs before going to the presentation of the framework of optical planar cavities. This chapter ends with a review of the literature about the impact of TDs and PDs.
- **Chapter 2: Sample fabrication and basic properties** are presented. Their analysis in regard of the knowledge from Chapter 1 concludes on a 1:1 correspondence between TDs and V-pits and shows hints for growth grains that could have an impact on the QW properties. In addition, we see from the first photoluminescence (PL) investigations the effect of interference due to the Si substrate. It seems that there is a luminescence improvement by using an In-containing UL, which needs to be quantitatively studied. This chapter ends with temperature-dependent PL measurements allowing to extract the temperature variation of the B coefficient in the framework of the ABC model.
- **Chapter 3: Impact of the underlayer on InGaN QWs grown on Si** is proven, by advanced temperature- and power-dependent PL measurements. We describe the arcana of these complex measurements owing to the presence of interference. The evident conclusion on the impact of the UL is drawn and related to the importance of PDs in the regime of high TD-density. We model precisely the efficiency curves we acquired, using a home-developed numerical tool using a comprehensive framework based on David *et al.* [17]. From additional mesoscopic time-resolved PL (TRPL) characterisations, we give an estimate of the internal quantum efficiency (IQE) of the samples.
- **Chapter 4: Nanoscale optical properties of InGaN quantum wells** are investigated in order to answer to the question of growth grain impacts on the QWs. This appears to be confirmed by the sole aspect of the cathodoluminescence (CL) intensity maps. Corroborated findings from the energy mappings and from CL lifetime mappings confirm that growth grain boundaries are crystallographically materialised and fractionate the QWs — *i.e.*, the carriers are confined in areas of $\sim 0.5\mu\text{m}$ in diameter. We develop a numerical simulation of these carrier energy barrier features, which supports our phenomenological understanding.
- **Chapter 5: GaN on Si photonic devices** are designed, simulated, fabricated and characterised. We first report on the achievement of high- Q nanobeam photonic crystal (PhC) with embedded PD mitigation superlattice (SL)-UL in monomode thin suspended membranes. Second, we take advantage of the challenging Fabry-Perot effects to conceive and fabricate microcavity LEDs. We detail a home-built automated angle-resolved electroluminescence (EL) setup and present the results on the LEDs.

The conclusion links up all the results and provides perspectives for further research and developments.

Part of the present investigations was published in Lottigier *et al.* [18].

1 Background information

This chapter presents the general information needed to fully understand the context of the research led during the whole project. It features a description of the structural and optical properties of III-Ns, their growth challenges, a section about microcavity effects, another one presenting technological applications, and a review about the current understanding of InGaN QW efficiency and the impact of V-shaped pits.

1.1 III-nitrides

1.1.1 Structural and polarisation properties

III-Ns main binary compounds are AlN, GaN and InN. They can then combine into ternary alloys (AlInN, InGaN, AlGaN) or even the quaternary one (AlInGaN). During growth, they crystallise into either the zincblende or the wurtzite structure, but the first is metastable and turns into the second.[19, 20] This is an important asset of the III-N family, which in the wurtzite phase (represented in Figure 1.1) possess a direct bandgap. III-N have two peculiarities regarding their polarisation, mainly due to the absence of inversion symmetry: First, the metal - nitride bond is creating a vertical dipole moment (along the **c**-axis) which in turn generates a *spontaneous* polarisation field P_{sp} . This field can be interpolated for a general ternary alloy $A_xB_{1-x}N$: [21]

$$P_{sp, A_xB_{1-x}N} = xP_{sp, AN} + (1 - x)P_{sp, BN} - b_{A,B}x(1 - x) \quad (1.1)$$

with x the alloying fraction and $b_{A, B}$ the polarisation bowing parameter between A and B. All relevant parameters are reported in Table 1.1.

The second consequence of the lack of inversion symmetry comes from the growth of III-Ns which can be along the $\langle 0001 \rangle$ direction (Ga-polar) or $\langle 000\bar{1} \rangle$ direction (N-polar). This has important consequences on impurity concentration and surface morphology. All optoelectronic devices are grown on the Ga-polar face.

These compounds are grown mainly by metal-organic chemical vapour deposition (MOCVD)

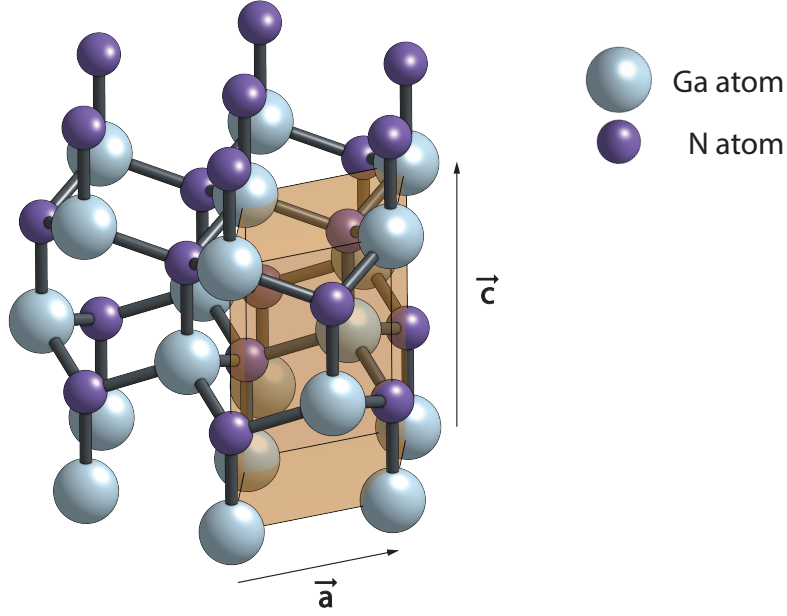


Figure 1.1: Crystallographic wurtzite structure of GaN.

Table 1.1: Spontaneous polarisation parameters.

	AlN	GaN	InN
P_{sp}	-0.090	-0.034	-0.042
	AlGaN	AlInN	InGaN
$b_{A, B}$	0.037	0.021	0.070

or molecular beam epitaxy (MBE), on foreign substrates, and/or for a final heteroepitaxial design — which means, the successive epilayers do not have the same lattice parameters and thermal coefficients, for example.[22] This is the reason why an epilayer contains a basal strain given by:

$$\epsilon = \frac{a_s - a_l}{a_l} \quad (1.2)$$

with a_s the substrate lattice constant and a_l the one of the considered layer. From this strain state, compressive ($\epsilon < 0$) or tensile ($\epsilon > 0$), a piezoelectric field appears in the layer. In III-Ns, the *piezoelectric* polarisation for a growth along the **c**-axis is given by:[23]

$$P_{AlN}^{pz} = \begin{cases} -1.808\epsilon + 5.624\epsilon^2, & \text{for } \epsilon < 0 \\ -1.808\epsilon - 7.888\epsilon^2, & \text{for } \epsilon > 0 \end{cases} \quad (1.3)$$

$$P_{GaN}^{pz} = -0.918\epsilon + 9.541\epsilon^2$$

$$P_{InN}^{pz} = -1.373\epsilon + 7.559\epsilon^2$$

In the same way as for the spontaneous polarisation, the piezoelectric polarisation of a ternary

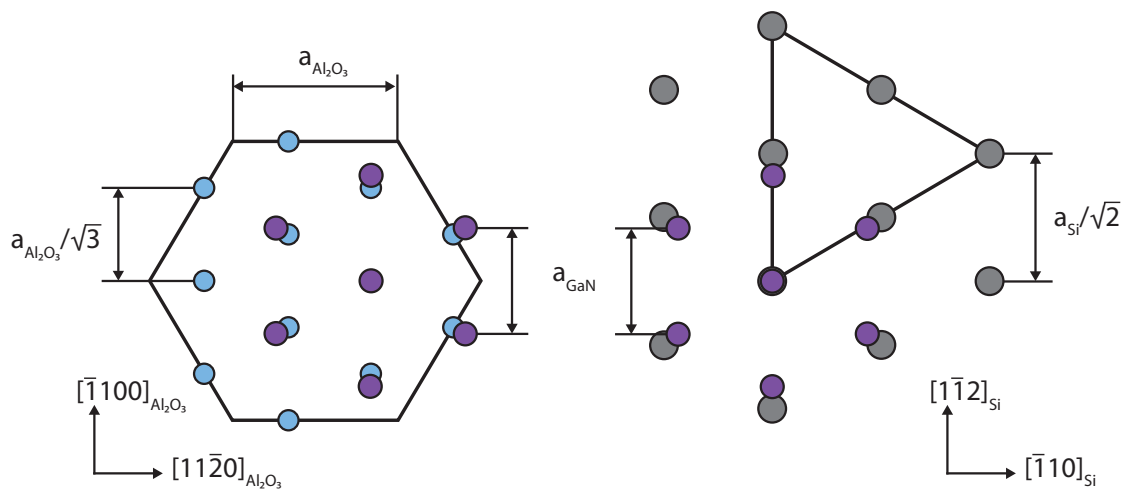


Figure 1.2: Crystalline 2D-projection of GaN on the aluminium atoms of sapphire (left) and Si(111) (right) substrates. The lattice mismatch is 16% resp. -17% for sapphire resp. Si.

compound can be interpolated with a bowing.

Substrates

Historically, the first demonstration of high brightness GaN-based LEDs was achieved in 1994 by S. Nakamura using sapphire substrates.[1] This set such substrates as reference ones, notably because Al₂O₃ possess a great thermal stability and a thermal expansion coefficient higher than that of GaN. In addition to this, sapphire substrates are transparent, which enables light emission through the substrate at the back of the device. Also, the Al sublattice transforms into AlN upon nitridation which helps for the subsequent III-N growth. Major drawbacks for sapphire start with the fact that this material cannot be etched easily. As a consequence, integration of photonic devices on Si platforms is made difficult. Second, since sapphire is electrically insulating, it is not possible to take contact from the substrate. Finally, sapphire has a rather low thermal conduction, which could cause heat dissipation problems for high-power devices.

The first drawback of sapphire is the main reason why growing III-Ns on Si is studied. Indeed, for some applications exemplified in the present thesis, underetching the substrate below III-N structures is needed to create suspended membranes. Under two other considerations, Si is much worse than sapphire: the thermal and the chemical stabilities are diminished. In particular, GaN reacts with Si under the so-called *melt-back etching* which needs to be considered during the epilayer design.[24–26]

Si presents a lattice mismatch to GaN of -17% (versus 16% for sapphire) which causes tensile strain (on sapphire, GaN is under compressive strain) as sketched on Figure 1.2. Such a strain state of GaN on Si(111) causes the apparition of *threading dislocations* (TDs) at densities higher than 10^{10} cm^{-2} in thin epilayers. Finally, since Si has a very low thermal expansion coefficient,

Chapter 1. Background information

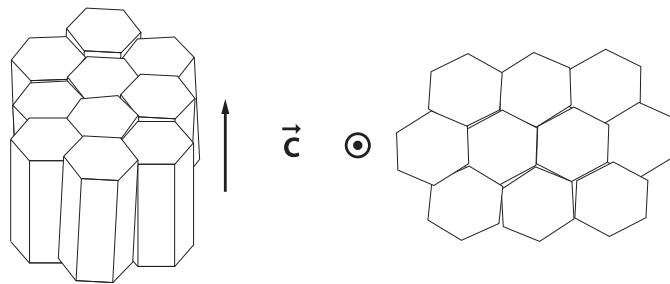


Figure 1.3: Grains formed at the start of the growth process. Adapted from Feltin [27].

the cooldown after growth can yield cracking of epilayers, even for thin epilayers ($\sim 1 \mu\text{m}$).

Threading dislocations

At the beginning of the growth, nucleation forms grains at the surface of the substrate. Many grains eventually coalesce but there are remaining low angle grain boundaries. The growth continues vertically, with high coherence along the \mathbf{c} -axis. This process is depicted in Figure 1.3. As shown on the scheme, some grains can be tilted (out of plane) and join vertical grains *via* a so-called screw or c-type dislocation. These are called like this because the Burgers vector, *i.e.* the direction in which the atoms are shifted, is along \mathbf{c} (see Figure 1.4). This shift can be written in terms of crystallographic direction as $\mathbf{b} = \langle 0001 \rangle$. Such pure screw TDs are rare at the surface, because they are prone to neutralise during growth. On the other hand, the in-plane misorientation of the grains, the twist, leaves edge or a-type dislocations in the structure. Their Burgers vector follows \mathbf{a} , or $\mathbf{b} = \frac{a}{3} \langle 11\bar{2}0 \rangle$. There exists a third type of TDs, the combination of the two former ones: mixed a+c-dislocations are along $\mathbf{b} = \frac{a}{3} \langle 11\bar{2}3 \rangle$. On

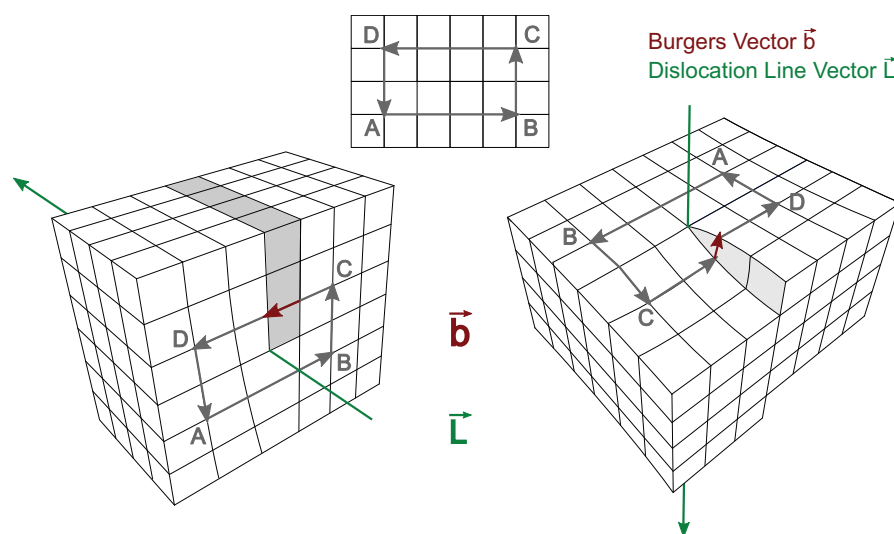


Figure 1.4: Burgers vectors of edge (left) and screw (right) dislocations. Adapted from Fleck [28].

sapphire substrates, dislocation densities are in the 10^8 cm^{-2} range, which might be slightly higher when growing on Si substrates. This has to be compared to the TD densities in samples homoepitaxially grown on GaN templates, that amounts to $\sim 10^6 \text{ cm}^{-2}$.

Point defects

In a crystal, there can be defects at the atomic scale. Such defects can be intended — due to doping — or unintended. Let us review briefly what these *point defects* (PDs) can be, and how they appear.

During growth of the material, impurities present in the reactor can be incorporated, perturbing the ideal sequence of Ga and N atoms for GaN. These can be, for example, C, Si, H, O, Be, Mn, Cd, among others. When substituted to Ga sites, C, Si and Ge are so-called shallow donors, because they bring additional electrons — O, S and Se are the same when substituting N atoms. Conversely, Be, Mg, Ca, Zn and Ca will act as acceptors when replacing Ga, while C, Si and Ge would be substitutional acceptors in N sites. Hence, theoretically, some substituents could be used as both donors and acceptors. Nonetheless, their behaviour depends on the position of the Fermi level E_F . Let us take the examples of Mg and Si, two good candidates for doping due to their low formation energies. Under standard conditions, the rather high E_F position leads to a low formation energy of Mg_{Ga} acceptors (substituted to Ga). However, as the concentration of Mg increases the formation energy of Mg_{Ga} increases while it decreases for V_{N} leading to Mg passivation.[29] On the other hand, under standard Ga-rich conditions, Si acts preferentially as substitutional donor Si_{Ga} than as acceptor Si_{N} , due to the lower formation energy (0.9 eV *versus* 3.0 eV).[30–32] Si and Mg are so far the most common dopants for n-type and p-type GaN, respectively.

On the other hand, there are also native PDs, interstitial, antisite and substitutional defects or vacancies. In GaN, the first two happen when one Ga or N atom lies in between normal crystallographic positions or at the other atom's position, respectively. Vacancies (Ga or N vacancies, divacancies) are maybe the most problematic PDs when it comes to efficiency, as we will see later. Because these have been proposed to have such a strong footprint on optical properties of III-Ns, specific studies have been made to understand their formation mechanism by designing specific growth recipes.

Surface defects

As a result, it has been observed by Haller [33] and further by Chen *et al.* [13], that the most detrimental PDs stem from growth-generated surface defects (SDs). In these studies, it has been shown that when growing GaN at high temperature (HT-GaN, $> 870^\circ\text{C}$), SDs (supposed to be nitrogen vacancies) are created and maintained at the growing surface, as sketched in Figure 1.5 (center). Their density $[\text{SD}]_0$ is estimated to be in the 10^9 – 10^{10} cm^{-2} range.[14, 33] If low temperature GaN ($< 800^\circ\text{C}$) is grown on top of such a layer, new SDs will no longer be

Chapter 1. Background information

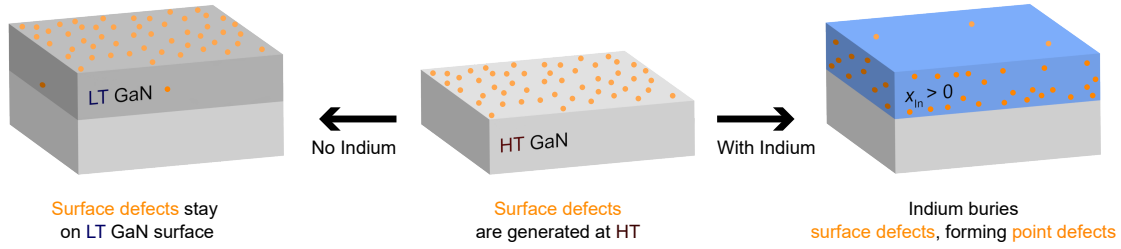


Figure 1.5: Formation of point defects (PDs). Surface defects are generated during high-temperature growth of GaN. If low temperature GaN is grown, these defects stay at the sample's surface (left). Else, if an In-containing layer is grown, these SDs are incorporated, forming PDs (right).

generated, however the existing ones will stay at the surface *via* a surface segregation process (*cf* Fig. 1.5, left). Now, if an In-containing layer is grown instead, the SDs are buried in this layer as PDs (probably in the form of N-Ga divacancy complexes [13]), thereby massively reducing the amount of SDs at the end of the UL growth. These PDs create a defect state at mid-gap.[34] This phenomenon has been modeled by Haller [33] to account for the remaining density of SDs after M monolayers of $\text{In}_x\text{Ga}_{1-x}\text{N}$:

$$[\text{SD}]_M = [\text{SD}]_0 (R_{\text{GaN}} - px)^M \quad (1.4)$$

with R_{GaN} the SD segregation coefficient of GaN and p the indium-SD interaction efficiency. Of course, if another HT-GaN layer is grown afterwards, SDs will be created again.

Optical properties can be very powerful to indirectly understand material properties. This is where our attention now goes.

1.1.2 Optical properties

Since III-Ns are crystals, they mutualise the quantised energy states of their constituent atoms into continuous valence E_v and conduction E_c energy bands as sketched in Figure 1.6(a). This transformation takes place in a periodic structure, which in turn forbids electronic states to form over a given energy range, known as the bandgap. A primordial asset of GaN and alloys is a direct bandgap, *i.e.* the position of the E_v maximum and the E_c minimum being at the same place in the reciprocal space. This specificity allows for efficient light emission due to both momentum and energy conservations. By using a modified Vegard's law, just as for the polarisation fields in the previous section, one can interpolate the bandgap of any alloy to predict its bandgap energy:

$$E_{g, A_xB_{1-x}N} = xE_{g, AN} + (1-x)E_{g, BN} - b_{A,B}x(1-x) \quad (1.5)$$

From the bandgaps listed in Table 1.2 from Vurgaftman *et al.* [20], Wu *et al.* [36], Feneberg *et al.* [37], and Leroux *et al.* [38], we can construct a graphical representation of the bandgap *versus*

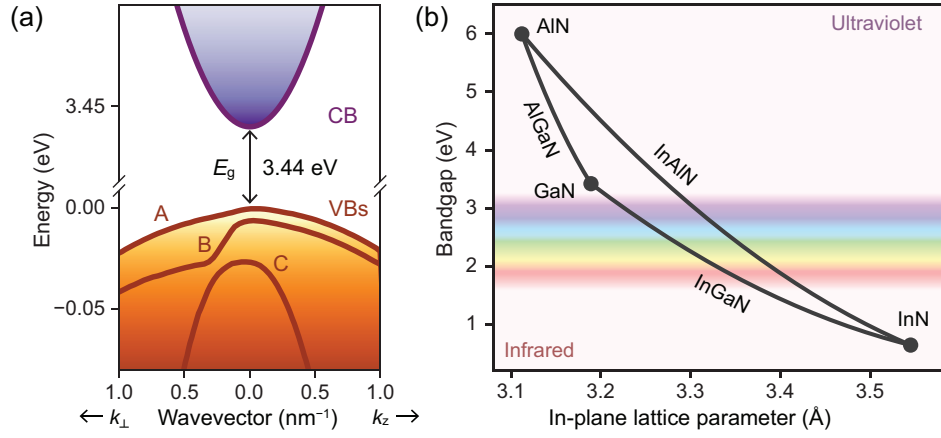


Figure 1.6: (a) Band structure of GaN near the Γ point (*i.e.*, where $\mathbf{k} = \mathbf{0}$). (b) Bandgap *versus* lattice parameter a of the three main III-Ns and their alloys, at room-temperature. Adapted from Weatherley [35].

Table 1.2: Energy bandgap and temperature coefficients for different III-N semiconductors.

	AlN	GaN	InN
E_g (~0 K) [eV]	6.09 [37]	3.51 [39]	0.69 [36]
E_g (300 K) [eV]	6.00	3.44	0.64
α [meV/K]	1.799 [20]	0.887 [38]	0.414 [36]
β [K]	1462 [20]	874 [38]	454 [36]

in-plane lattice parameter a , represented in Figure 1.6(b).

We can stop to contemplate the broad range of E_g accessible with III-N materials: alloying allows to span the bandgap from infra-red (IR) to ultra-violet (UV), covering the whole visible spectrum with InGaIn alone. Although valuable progress was made, notably in the green region (previously known as the "green-gap"), fabricating light-emitters in specific parts of this spectrum remains challenging, notably in the red part of the visible spectrum — mainly due to the difficulties of obtaining good-quality materials with higher In content — and in deep UV.

In addition, since strain modifies the interatomic distance, the band structure hence the bandgap changes as well. Consequently, an increase in temperature produces a tensile strain on Si substrate due to the thermal expansion coefficient mismatch. Temperature-induced variation of E_g is shown in Figure 1.7 for both Si(111) and sapphire substrates. The total variation ΔE_g are 60 meV and 72 meV, respectively. For the modelling of this phenomenon, an empirical law named after Varshni is used:[40]

$$E_g(T) = E_{g,0\text{K}} - \frac{\alpha T^2}{T + \beta} \quad (1.6)$$

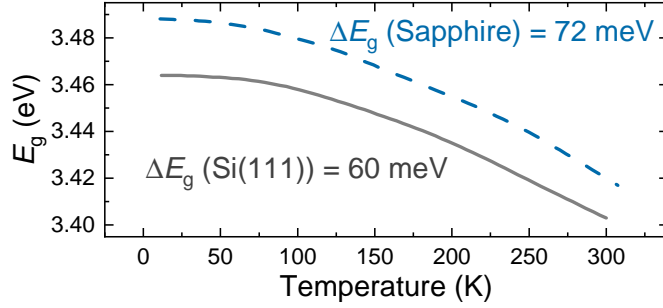


Figure 1.7: Variation of GaN bandgap E_g versus temperature. The grey (respectively dashed blue) curve is for GaN grown on Si(111) (resp. on sapphire). The difference of the two curves stems from different substrate thermal expansions. Adapted from Feltin [27].

with T the temperature, while α and β are experimental fitting parameters.

1.2 Quantum well

The availability of alloys allows to create heterostructures, by growing different layers one after the other. These heterostructures can have very interesting properties, because they produce a variation of the bandgap, hence of the energy experienced by carriers in the materials. Specific designs (QWs) can be used to enhance the interaction of electrons and holes in order to make radiative recombination more probable. For example, by using a L_{QW} -thick layer of a material with a lower bandgap compared to that of the surroundings (the barrier), carriers are kept with a higher density in a 2D-landscape. In the beginnings of III-N emitters, InGaN/AlGaIn double heterostructures (DHs) with $L = 50 - 150$ nm thicknesses were used to build LEDs.[7] It was found very soon that by reducing the DH size down to 2 nm, much better efficiencies were possible: 7.3% compared to 2.7%.[1] Not to be overlooked, when the typical size L_{QW} of such a bandgap variation reaches the de Broglie wavelength $\lambda_{DB} = \frac{2\pi\hbar}{\sqrt{2m_{e^*}E}}$ of carriers (effective mass m_{e^*} , energy E), quantisation of the carrier energy levels happens as sketched in Figure 1.8. In the present thesis, the confinement of carriers happens exclusively along the \mathbf{c} -axis (along the z -direction of the figure), in a lower-bandgap material $\text{In}_{0.17}\text{Ga}_{0.83}\text{N}$. Such a quantum structure relying on 1D-confinement is called a *quantum well*, but there exist also structures with 2D-confinement (*quantum wires*) and 3D-confinement (*quantum dots*).

The conduction subband number j can be expressed in case of infinite barrier heights as:

$$E_{c,j}(k_x, k_y) = E_{g,QW} + \frac{(\hbar\pi j)^2}{2m_{e^*}L_{QW}^2} + \frac{\hbar^2(k_x^2 + k_y^2)}{2m_{e^*}} \quad (1.7)$$

where $E_{g,QW}$ is the bandgap of the QW material, in our case $\text{In}_{0.17}\text{Ga}_{0.83}\text{N}$, and m_{e^*} is the effective mass of an electron in the well.[41] Subsequently, the minimum energy of a photon

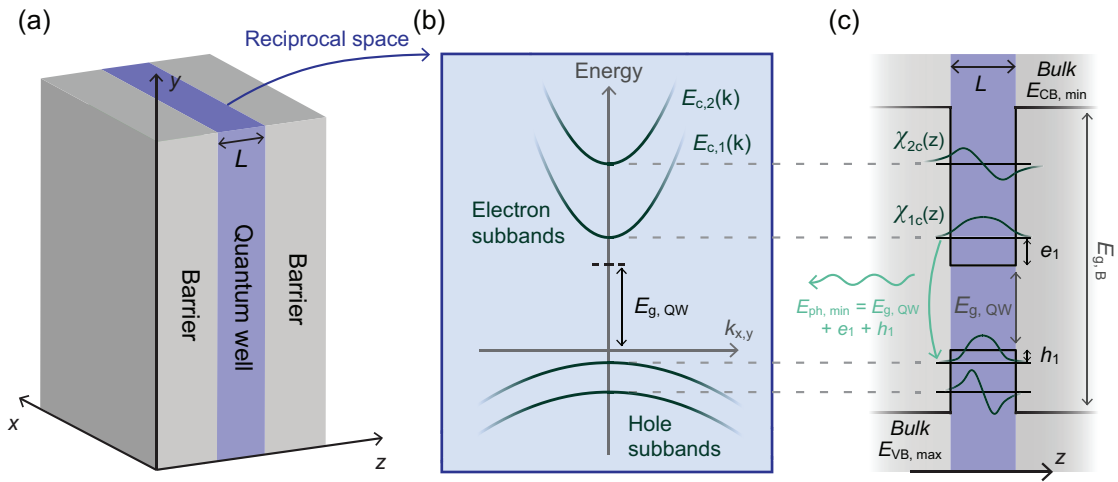


Figure 1.8: (a) Scheme of a QW with width L_{QW} . (b) In reciprocal space, confined carriers see their states quantised in the form of subbands. (c) The photons emitted by such a quantum heterostructure have a minimum energy of $E_{\text{ph, min}} = E_{\text{g, QW}} + e_1 + h_1$. Adapted from Weatherley [35].

emitted by carrier recombination in such a QW is¹

$$E_{\text{ph, min}} = E_{\text{g, QW}} + e_1 + h_1 \quad (1.8)$$

with e_1 the confinement energy for the $j = 1$ conduction (electron) subband, and h_1 the confinement energy for the highest $j = 1$ valence subband.

Oscillator strength

To quantify the probability for a photon to be emitted in a QW we refer to the oscillator strength

$$f_{\text{osc}} \propto |\langle \phi_e | r \rangle \langle r | \phi_h \rangle|^2 \quad (1.9)$$

where r is the position vector and $\phi_{e, h}$ are the wavefunctions of the electron and the hole, respectively.[41] This is why the reduction in L_{QW} , by enhancing the overlap of ϕ_e and ϕ_h , boosts f_{osc} hence the probability for light-emission.

Quantum-confined Stark effect

In the contrary, there is a subtlety which could act in an opposite way by separating electrons and holes: the quantum-confined Stark effect (QCSE). As mentioned earlier, a polarisation field exists along the \mathbf{c} -axis of III-Ns. Heteroepitaxial growth causes polarisation discontinuities ΔP , which in turn create sheets of charge densities σ^+ and σ^- . From these sheets, we can compute

¹This is formulated in the framework of free electrons and holes. To consider the formation of excitons, we also have to remove their binding energy E_B .

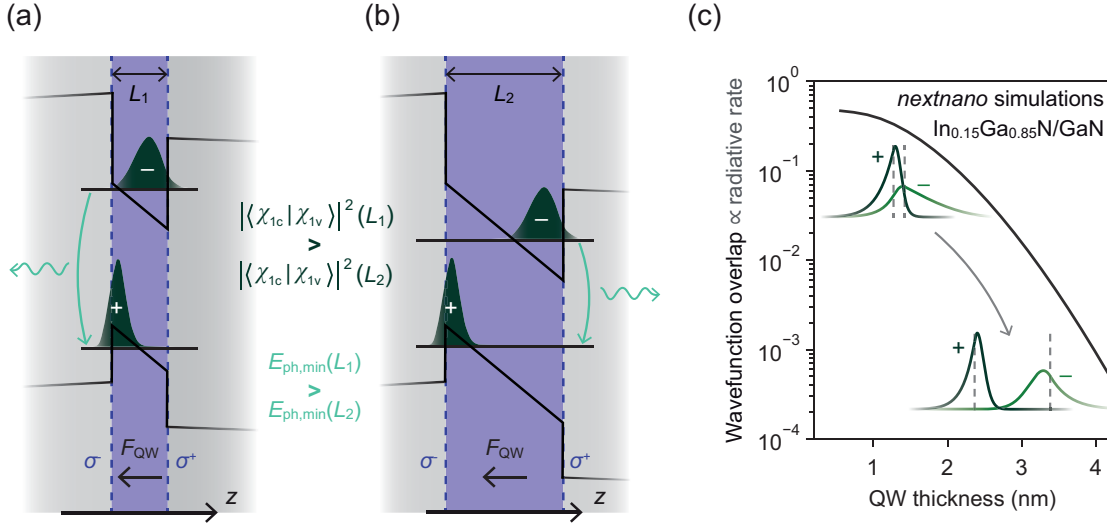


Figure 1.9: (a) Sketch of wavefunctions in a QWs under QCSE effect. (b) Sketch of wavefunctions in a thicker QWs where the overlap is reduced. (c) Example of wavefunction overlap simulations using the commercial software nextnano. Adapted from Weatherley [35].

the field generated in the QW:

$$F_{QW} = \frac{\sigma_{\mathbf{p}}}{\epsilon_w} \mathbf{n} \quad (1.10)$$

with $\sigma_{\mathbf{p}} = -\Delta P \cdot \mathbf{n}$, \mathbf{n} the unit vector perpendicular to the interface plane, and $\epsilon_w = \epsilon_0 \cdot \epsilon_r$ the product of vacuum and QW relative permittivities. From the polarisation contributions, we have:

$$\Delta P = (P_{sp, B} + P_{pz, B}) - (P_{sp, QW} + P_{pz, QW}) \quad (1.11)$$

where subscript "B" stands for barrier. In InGaN/GaN or GaN/AlGaIn QWs, F_{QW} can reach several MV/cm.[42–44]

In turn, this built-in field distorts the bandstructure, thereby creating a triangular-shaped potential in the QWs, as sketched in Figure 1.9(a)-(b). The wavefunctions of the carriers (marked as + for holes and - for electrons) are impacted, displaced and even compressed, which leads to changes in the oscillator strength and the confinement energy. As a consequence, the emission energy after recombination of two carriers also changes, and is now written:

$$E_{ph, min} = E_{g, QW} + e_1 + h_1 - qF_{QW}L_{QW} \quad (1.12)$$

with q the elementary charge.

The reduction of the oscillator strength due to the separation of electron and holes, calculated and represented in Figure 1.9(c), is the main deleterious consequence. The reduction in the overlap of wavefunctions increases the radiative lifetime of the carriers, thereby potentially decreasing light emission efficiency if one considers a standard model with competing nonradiative channels. This is luckily not the only consequence of QCSE. This effect allows to tune

the emission energy of QWs by changing their thickness L_{QW} . Advantageously, it is possible to fabricate QWs with a lower bandgap than the bulk material, and reach wavelengths beyond the In incorporation limit (25–30% in pseudomorphic layers), up to 510–550 nm (2.43–2.25 eV, *versus* 2.54 eV in the bulk).

In addition to this mechanism allowing bandgap engineering, the choice of materials also plays a role. Indeed, the increase of In content yields a decrease in the emission energy, by both decreasing the bulk bandgap and increasing the QCSE. Of course, this comes with a reduction in the oscillator strength. Here we see that a trade-off has to be found between QWs thickness and In content, to achieve the desired emission wavelength without sacrificing too much on the efficiency side.

1.3 Localisation in quantum wells

Incorporating indium in GaN during growth happens at the atomic scale, and even under the best conditions, is subject to disorder. Therefore, there exist random fluctuations of the In distribution in the InGaN QWs. Such random alloy fluctuations yield fluctuations in the potential energy, as exemplified in Figure 1.10(a). As a consequence, potential minima create localised states for the carriers in the QWs.[45, 46] As deduced from previous studies, potential minima are around 3 nm in diameter,[46] which corresponds to a 2D-density of $\sim 10^{13} \text{ cm}^{-2}$ localisation states, or $N_{\text{loc}} \sim 4 \times 10^{19} \text{ cm}^{-3}$ for a standard 2.6 nm QWs. When the injected carrier density is above this value, we could hypothesize that due to exclusion principles, all the additional carriers are delocalised. Conversely, one shall consider carrier localisation effects in III-N QWs up to a carrier density of 10^{19} – 10^{20} cm^{-3} , *i.e.* under almost all usual experimental conditions. It means that the minimum emitted photon energy has to be adapted to consider the localisation energy E_{loc} of these states:

$$E_{\text{ph, min}} = E_{\text{g, QW}} + e_1 + h_1 - qF_{\text{QW}}L - E_{\text{loc}} \quad (1.13)$$

Statistical distribution of the localisation centers potential depths leads to broadening of the absorption edge and emission spectrum. Experimentally, it can impact devices in a substantive manner.[45]

The second phenomenon within QWs that is highly impacted by localisation is carrier diffusion. In non-alloyed materials *i.e.* not subject to random alloy potential fluctuations, the diffusion coefficient D decreases with increasing temperature from cryogenic values to room-temperature. Two good examples are GaAs (from 170 to 20 cm^2s^{-1}) and GaN (4 to 0.8 cm^2s^{-1}).[47–49] This is due to carrier scattering being thermally activated. In opposition to such a trend, in InGaN QWs, D values start below 0.01 cm^2s^{-1} at 10 K and increase toward room-temperature, as measured by Ruzicka *et al.* [47] and displayed in Figure 1.10(b). The small D coefficient speaks for a close-to-complete localisation of carriers at low temperature in the potential minima.[50] Delocalisation from these dips is only possible with enough thermal energy. Figure 1.10(c) shows the second hint for localisation-impacted diffusivity. As will be

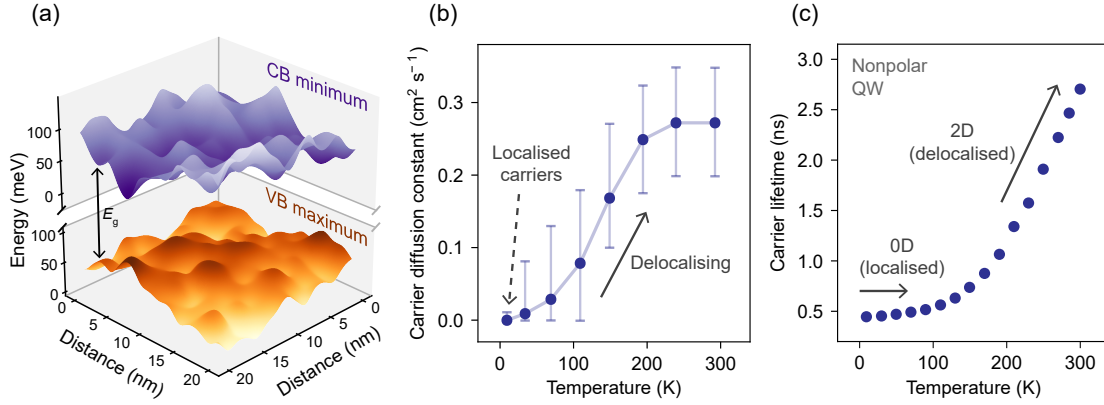


Figure 1.10: (a) Real-space energy landscape simulated for $x = 17\%$. The fluctuating potential landscape is due to In incorporation random distribution.[46] For this simulated landscape, unit cells have been filled with an averaged indium content following a binomial probability law. (b) Carrier diffusion data for InGaN, from Ruzicka *et al.* [47]. The small D coefficient in InGaN QWs at low temperatures suggests close-to-complete carrier localisation in the potential minima.[50] Delocalisation from these dips is only possible with enough thermal energy. (c) Here we have another significant insight into the impact of localisation on carrier diffusion. As elaborated in Section 1.4, a QWs typically exhibits a carrier radiative lifetime that should follow a linear variation with temperature. However, the carrier lifetime τ versus temperature T observed by Ščajev *et al.* [48] presents an intriguing contrast, especially at low temperatures. This behaviour hints at the quasi-insensitivity of τ to cryogenic temperature variations. The explanation for this anomaly lies in the fact that, up to a certain delocalisation temperature (approximately in the range 70–100 K), carriers are effectively confined within pseudo-0D centers.[48].

discussed in Section 1.4, in a QW, the carrier radiative lifetime should follow a linear variation with temperature, contrarily to the carrier lifetime τ versus T observed by Ščajev *et al.* [48] at low temperatures. The way to explain this quasi-insensitivity of τ to cryogenic temperature variation is that up to the delocalisation temperature (here, in the range 70–100 K), carriers are trapped in 0D centers, the potential fluctuation minima.

In a d -dimensional system, the diffusion length can be expressed as $L_D = \sqrt{2dD\tau}$. Hence in two dimension systems like QWs,

$$L_D = 2\sqrt{D\tau}. \quad (1.14)$$

Considering the maximum values observed at room-temperature for both D (diffusion coefficient) and τ (carrier lifetime) in high-quality InGaN QWs, it would be reasonable to anticipate a significant diffusion length at 300 K. Nevertheless, the extent of carrier diffusion within InGaN QWs at room-temperature has been a topic of debate over the last decade. Some have asserted that, even at 300 K, localisation still plays a role.[8, 51] In the historical framework of strong deleterious effect of TDs in light-emitting semiconductors, this localisation phenomenon was called to explain why high efficiency was observed in InGaN-based emitters — by preventing

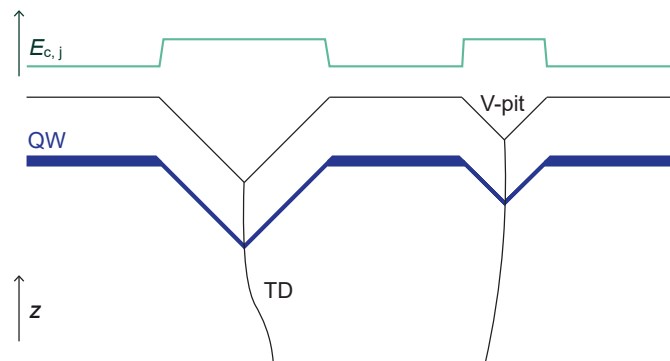


Figure 1.11: Within V-pits, the QW thickness may be reduced, thereby lifting the energy of the quantised bands, represented in green (*cf* Equ. 1.7). In turn, this can create an energy barrier preventing carriers to reach the TD within the pit.

carriers to diffuse toward TDs.[9] One of the common arguments supporting this was the observation of rather short range diffusion in InGaN QWs. This paradigm has recently been more and more questioned, as diffusion lengths were measured to be above hundreds of nanometers to microns.[52, 53]

Such localisation effects are due to energy dips, at the atomic scale. There also exist other energy variation features, on larger scales. Specifically, energy variations due to morphology-related indium incorporation can appear. It has been observed that meandering or step-bunching (*cf* Fig. 2.8) can *e.g.* reduce In content, thereby creating energy barriers for carriers in InGaN QWs.[54]

Additionally, at an intermediate scale, V-shaped pits, deep enough to contain the QWs, can also create barriers for carriers and impact the emission efficiency, as illustrated on Figure 1.11. This will be discussed in Section 1.7. To correctly understand light-emission efficiency, we first need to have a clear vision of the processes at play once carriers are injected in the active material.

1.4 ABC model

In this section, we will discuss the *IQE* of InGaN/GaN QWs. To acknowledge the various processes a carrier can experience in a semiconductor, a model was developed with the influences of 1, 2 and 3 carrier-dependent processes, represented by *A*, *B* and *C* coefficients, respectively.

A coefficient

The first processes happen proportionally to the carrier density. Studied by Shockley, Read and Hall, initially for germanium, the so-called Shockley-Read-Hall (SRH) processes, are essentially

Chapter 1. Background information

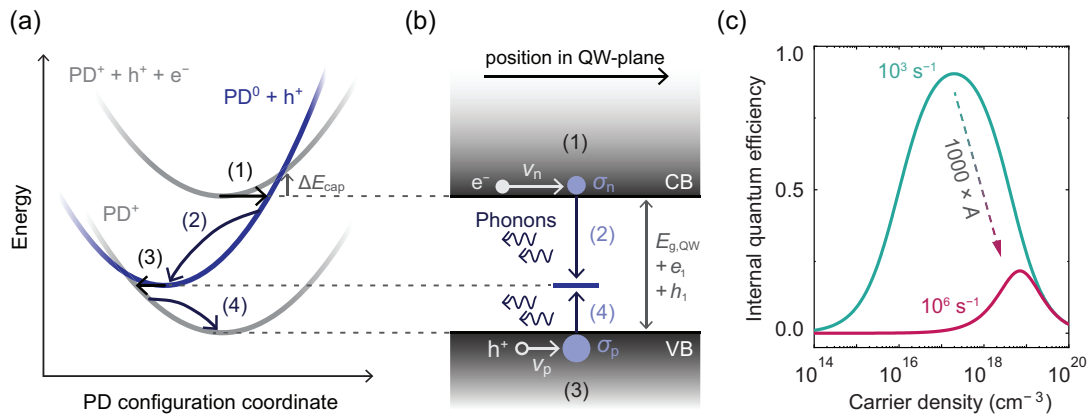


Figure 1.12: (a) SRH mechanism schematised on the band-diagram completed by a deep-defect, (b) situated in the middle of the material's bandgap. Adapted from Weatherley [35]. (c) Consequence in terms of IQE of a thousandfold increase in SRH recombinations, hence in the A coefficient. Note that the peak IQE moves toward higher carrier-densities.

linked to deep-defects in the bandgap, as sketched in Figure 1.12.[55, 56] Being nonradiative, they are very deleterious for optoelectronic materials, be it for light-emission or solar cells.[57, 58] As seen on the schematic representation of SRH, to fully understand this phenomenon, we need to delve into atomic-scale processes. The defects most prone to act as SRH centers are located near the middle of the bandgap, as shown in Figure 1.12(b), because their nonradiative recombination rates are the highest.[57] Of course, the energy of the defect is not fixed but depends on atomic arrangements. From the possible PDs described in Section 1.1.1, vacancies — *i.e.*, incorporated SDs — could be good candidates as major SRH centers, with their deep energy levels in the bandgap. This has to be kept in mind when developing growth methods, detailed in Section 2.1, to reduce the amount of these defects. In the vicinity of such a defect, SRH processes decompose into four-stages.

1. Electron capture: this leads to a change in the charge state of the PD.
2. Relaxation of the PD *via* the emission of multiple phonons.
3. Hole capture: the PD captures a hole and returns to its original charge state.
4. PD relaxation *via* phonons, which makes it available for another SRH process.

Since the PD can be in several natural charge states, SRH recombinations can also start with the capture of a hole. In fact, the carrier captures are the limiting steps,[57] therefore the whole process can be theoretically modeled as solely steps 1 and 3.

We can also define cross-sections σ_n and σ_p centered on the PD location in a QWs, to quantify its probability of capturing an electron or a hole. These quantities are subject to change accordingly with the charge state of the defect, since a very positively charged PD would attract more electrons; the strength of electron-phonon coupling; the energy barrier ΔE_{cap}

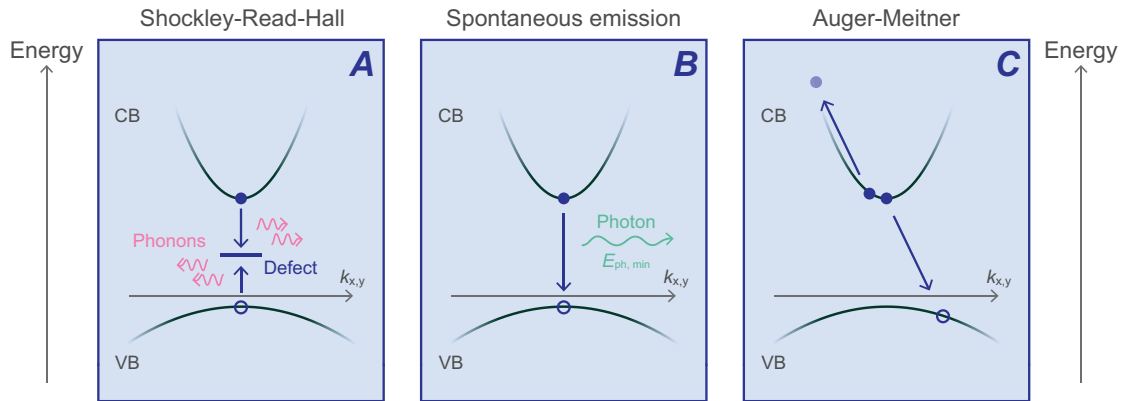


Figure 1.13: This figure illustrates the fundamental processes influencing the IQE in semiconductors. The A coefficient relates to SRH recombination, a nonradiative process primarily driven by deep defects in the bandgap. The B coefficient accounts for radiative recombination, which involves the interaction of electrons and holes. The C coefficient represents the Auger-Meitner (A-M) process, responsible for nonradiative recombination at high carrier densities. Defects can influence A and C . Additionally, localisation, carrier density, and temperature impact A , B and C , ultimately affecting the IQE of optoelectronic devices. The interplay between these coefficients is central to optimizing device efficiency.

relative to the capture of the carrier; and finally, the temperature, which can help to overcome this energy barrier (Arrhenius law).

Figure 1.12(b) is a simplified picture of such a SRH recombination, with perfect and equal carrier injection and no localisation in the well. Within this model, the total SRH rate can be linked to the carrier density n :

$$R_{\text{SRH}} = N_{\text{PD}} n \frac{\nu_n \sigma_n \nu_p \sigma_p}{\nu_n \sigma_n + \nu_p \sigma_p} \quad (1.15)$$

where ν_n , ν_p stand for the electron and hole thermal velocities and N_{PD} is the 3D PD concentration in the QWs.[59] This relationship can usually be simplified to $R_{\text{SRH}} = N_{\text{PD}} n \nu \sigma$, for one of the two carrier captures is the rate-determining step.[58]

With the previous definitions, we can now construct the expression of the A coefficient, embedding a comprehensive physical meaning:

$$A = N_{\text{PD}} \nu \sigma \quad (1.16)$$

The lifetime associated to these nonradiative recombinations is $\tau_{\text{SRH}} = \frac{1}{A}$.

The contribution of SRH recombinations only (*cf* Fig. 1.12(a), schematised in Fig. 1.13, A) to the IQE is depicted in Figure 1.12(c); a thousandfold increase in A , that could be multifactorial, leads inevitably to a stark reduction in efficiency. Carefully note that such a SRH-caused efficiency decrease comes with a displacement of the IQE peak toward higher carrier densities.

Temperature dependence of A

If we now consider N_{PD} as constant but let the temperature vary, which happens as soon as temperature-dependent measurements are conducted on a given sample, we observe an evolution of the SRH recombinations impacted by the temperature-related change in ν and σ . The thermal velocity of the carriers is naturally impacted by the thermal energy of the environment, following a square-root relationship: $\nu \propto \sqrt{T}$. Simultaneously, the area impacted by a PD is larger at higher temperatures, which translates into larger values of σ . [60] Altogether, increasing the temperature will lead to a shorter SRH nonradiative lifetime τ_{SRH} .

B coefficient

Photon emission in semiconductors are essentially interband emissions, a form of spontaneous emission happening when one electron of the conduction band recombines with a hole from the valence band (*cf* Fig. 1.13, B). The direct bandgap nature of GaN (and InGaN) is important since because the bands minimum and maximum both lie in the Γ point, the emission probability is roughly five orders of magnitude higher than for indirect bandgap materials. The rate of radiative recombination is linked to the carrier density n by the B coefficient:

$$R_{\text{R}} = Bn^2 \quad (1.17)$$

The squared carrier density comes from the fact that a recombination involves two carriers. B is called the radiative coefficient, and is proportional to the oscillator strength f_{osc} . [61]

Temperature dependence of B

There is also a temperature dependence for B , function of the structure's dimensionality:

$$B \propto T^{-d/2} \quad (1.18)$$

where d is the dimensionality of the structure. As a consequence, $B_{\text{3D}} \propto T^{-3/2}$ in bulk materials, [62, 63] whereas in QWs $B_{\text{2D}} \propto T^{-1}$ [64, 65] and in quantum dots B_{0D} is independent of T . [66]

Carrier-density dependence of B

The variation of the parameter B as a function of carrier density (n) has been tailored to the specific QWs investigated in this study, drawing from the insights of David *et al.* [17]. In Figure 1.14, the blue curve represents a scenario where Coulomb interactions are negligible. However, the dashed grey curve illustrates a notable rise in B at lower carrier densities, attributed to the phenomenon known as Coulomb enhancement (*cf* Fig. 1.14). This increase is a consequence of the mutual attraction between carriers of opposite charges within the QWs. [67–70] This effect is especially present in thin QWs where electron and hole wavefunctions overlap strongly.

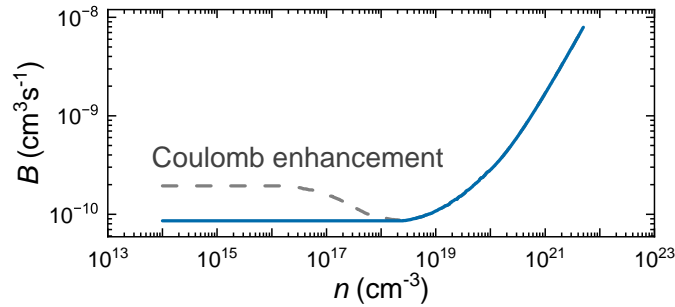


Figure 1.14: B variation against carrier density n for the QWs of the present study, adapted from David *et al.* [17]. The blue curve is a version where Coulomb interactions are not at play. In dashed grey, the increase of B at low carrier density is due to so-called Coulomb enhancement, due to the mutual attraction of opposite charge carriers.

When the carrier density increases, this effect disappears (here, above $\sim 1 \times 10^{17} \text{ cm}^{-3}$). As further explained in Section 3.2.2, we can neglect the Coulomb enhancement over the carrier densities we probe in the present study.

At even higher carrier densities, $> 1 \times 10^{19} \text{ cm}^{-3}$, the very high carrier density allows to screen the built-in electric field in the QWs, thereby allowing larger electron-hole overlap and increasing B .

C coefficient

The third phenomenon to be considered in the ABC model is a 3-body process, called Auger-Meitner (A-M), or simply Auger effect, whose rate is proportional to n^3 :

$$R_{AM} = C n^3 \quad (1.19)$$

A hole h and an electron e_1 recombine nonradiatively, by transferring their energy to another electron in the QWs, e_2 (eeh A-M). e_2 is promoted to a higher energy level, or even ionised (*cf* Fig. 1.13, C). The process can also be reversed, and involve instead one electron and two holes (hhe A-M). Of course, such recombinations are nonradiative hence deleterious to light-emission efficiency. Since this effect involves three carriers, it is dominant at high carrier-densities, and is responsible for the so-called "droop-regime" in LEDs.

A-M processes can also be enhanced by carrier localisation, in the sense that concentration of carriers in potential minima increases the probability of A-M recombination events.[71] Therefore, when the temperature is decreased, C increases.

Chapter 1. Background information

Carrier-density dependence of C

The C coefficient has a relationship to B : [72–74]

$$C(n) \sim B(n)^{1.2} \quad (1.20)$$

which can be understood in terms of wavefunction overlap, which impacts both radiative recombinations and A-M processes.

Finally, note that recent studies have also pointed out that defects can influence the A-M process, further affecting device efficiency. [17, 75] This intricate, defect-assisted A-M process happens when the trapping of a carrier in the vicinity of a defect increases the interaction with other carriers. As such, the C coefficient could be related to the A coefficient:

$$C = C_0 + kA \quad (1.21)$$

where C_0 is usually in the $10^{-29} \text{ cm}^6 \text{ s}^{-1}$ range for our QWs, and k values around $\sim 10^{36} \text{ cm}^6$ have been reported. [17]

IQE formulation

Now that we understand the different phenomena at play when carriers are injected in a QW, we can define the concept of IQE for light emission. All recombination processes can gather into an effective carrier lifetime:

$$\frac{1}{\tau} = R_{\text{SRH}} + R_{\text{R}} + R_{\text{AM}} \quad (1.22)$$

to which we can relate the radiative recombination we seek in a light emitter, namely $\tau_{\text{R}} = 1/Bn^2$. Therefore, we define the IQE as:

$$\eta_{\text{int}} = \frac{\tau}{\tau_{\text{R}}} = \frac{B}{A + Bn + Cn^2} \quad (1.23)$$

External quantum efficiency

We attract the attention on the fact that this is only the *internal* efficiency. To compute the external quantum efficiency (EQE) of a device, we have to take into account the *injection* efficiency η_{inj} of the carriers into the QWs, and the *extraction* efficiency η_{extr} quantifying which proportion of the emitted photons are outcoupled to the environment:

$$\eta = \eta_{\text{inj}} \eta_{\text{int}} \eta_{\text{extr}} \quad (1.24)$$

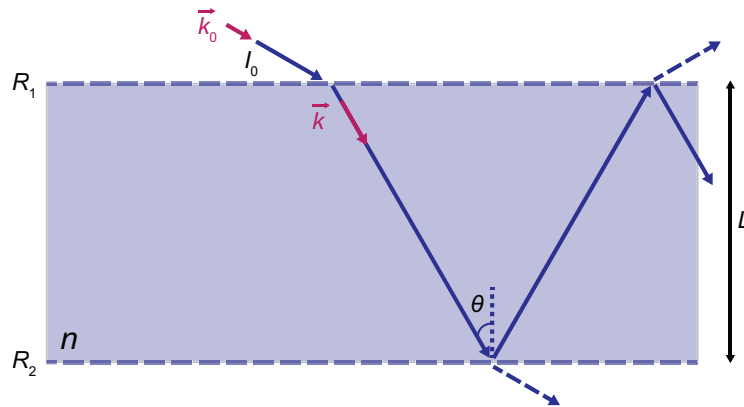


Figure 1.15: We schematize a basic Fabry-Perot cavity, consisting of a planar medium of index n and thickness L . The reflecting surfaces have intensity reflection coefficients R_1 and R_2 , respectively, and can either be specifically designed mirrors, or simply changes in refractive indexes.

1.5 Microcavity effects

To understand how impactful η_{extr} can be, we need to delve into the physics of cavities.

1.5.1 Fabry-Perot cavity

One of the most basic cavities, extensively studied, consists of a dielectric of index n and thickness L between two mirrors or reflecting surfaces, as sketched in Figure 1.15. This structure can act on an incident wave and modify it before reflecting or transmitting it. We will start by considering a plane wave characterised by its vacuum wavevector k_0 and wavelength λ_0 , forming an incident angle θ with the normal to the surface. Since the Fabry-Perot cavity is a medium of index n , the wavevector norm of the incident wave is transformed into:

$$k = nk_0 = \frac{n2\pi}{\lambda_0} \quad (1.25)$$

The pulsation of light, ω , is defined as

$$\omega = k_0 c = \frac{2\pi c}{\lambda_0} \quad (1.26)$$

in the $c = 1$ convention.

1.5.2 Transmission of a Fabry-Perot cavity

At each interface, the incident electromagnetic field (respectively intensity) is partially reflected at a ratio of $r_{1,2}$ (resp. $R_{1,2}$) and the other part is transmitted (the transmission coefficients for field and intensity are respectively denoted $t_{1,2}$ and $T_{1,2}$). The Fabry-Perot transmits a plane

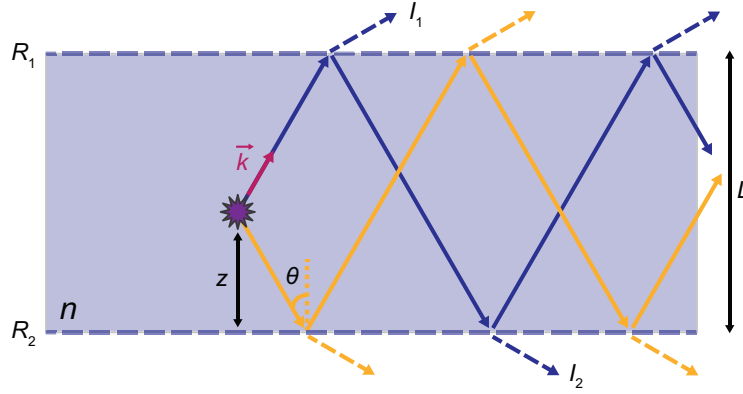


Figure 1.16: Here, we build upon the previous Fabry-Perot cavity, by adding an internal emitter located at position z .

wave whose expression is:

$$E_t = E_0 t_1 t_2 \left(1 + r_1 r_2 e^{2i\phi} + (r_1 r_2 e^{2i\phi})^2 + \dots \right) = E_0 \frac{t_1 t_2}{1 - r_1 r_2 e^{2i\phi}} \quad (1.27)$$

where 2ϕ represents the phase shift of the wave during a round-trip in the cavity, given by:

$$2\phi = 2nk_0 L \cos(\theta) \quad (1.28)$$

Now calculating the transmitted intensity of the Fabry-Perot, we have:

$$T_{\text{FP}} = \frac{|E_t|^2}{|E_0|^2} = \frac{T_1 T_2}{1 + R_1 R_2 - 2r_1 r_2 \cos 2\phi} = \frac{T_1 T_2}{(1 - r_1 r_2)^2} \mathcal{A}(\phi) \quad (1.29)$$

where \mathcal{A} represents the Airy function:

$$\mathcal{A}(\phi) = \frac{1}{1 + \Xi \sin^2 \phi} \quad (1.30)$$

and $\Xi = \frac{4r_1 r_2}{(1 - r_1 r_2)^2}$.

1.5.3 Fabry-Perot cavity with an embedded light source

A vast majority of light-emitting devices based on III-Ns can be considered as such Fabry-Perot cavities, since they consist in a medium of optical index sufficiently different from that of the environment (air or substrate), to create partially reflective surfaces at the top and the bottom. The major difference for such cavities is that they embed the light-emitter: the QWs. We sketch this new configuration in Figure 1.16, where the wave emission position is schematised by a star. Such a difference results in the fact that we now have to add the "blue" wave to the "orange" wave, both starting their propagation in a different direction, but with the same angle in the cavity. We define a dephasing ϕ' as the phase stemming from the position z of the

emitter:

$$\phi' = nk_0 z \cos(\theta) \quad (1.31)$$

From this point, we can compute the sum of the fields, transmitted by, *e.g.*, the top of the cavity:

$$E_t = E_0 e^{i\phi - \phi'} t_1 (1 + r_1 r_2 e^{2i\phi} + \dots) + E_0 e^{i\phi + \phi'} r_2 t_1 (1 + r_1 r_2 e^{2i\phi} + \dots) = E_0 t_1 \frac{1 + r_2 e^{2i\phi'}}{1 - r_1 r_2 e^{2i\phi}} \quad (1.32)$$

If we define the antinode factor $\zeta(\phi') = 1 + R_2 + 2r_2 \cos 2\phi'$, *i.e.*, the density of the electromagnetic field inside the cavity, the intensity emitted above the cavity writes:

$$I_1 = |E_1|^2 = I_0 \frac{T_1}{(1 - r_1 r_2)^2} \mathcal{A}(\phi) \zeta(\phi') \quad (1.33)$$

and its counterpart emitted below the cavity:

$$I_2 = I_0 \frac{T_2}{(1 - r_1 r_2)^2} \mathcal{A}(\phi) \zeta(\phi') \quad (1.34)$$

Physically, the emission intensity in a specific direction stems from two phenomena. First, the Airy function reflects the resonant characteristics of the bare Fabry-Perot cavity. Second, the physics behind the antinode factor is the coupling efficiency between light and the Fabry-Perot modes. The latter, ζ , reaches its maximum value when the source position coincides with an antinode of a given mode, thereby significantly enhancing the external emission of this mode.

To illustrate this concept, we can consider a source position in the middle of the cavity: $z = L/2$. In this case, \mathcal{A} reaches its maximum value for $\phi \equiv 0 \pmod{\pi}$, thereby creating constructive interferences within the cavity. Note that all the odd Fabry-Perot modes, *i.e.*, when ϕ is an odd multiple of π , have a minimal coupling to the light source: $\zeta = 1 + R_2 - 2r_2$ is at its minimal value.

1.5.4 Light extraction and cavity order

To engineer the cavity such that light extraction is maximised, we need to consider a more general case, where the outer medium can have an index n_{ext} . Due to this change, we need now consider total internal reflection. There exists a critical angle θ_c above which the wave stays in the cavity, with no coupling to the external medium. The critical angle writes:

$$\theta_c = \arcsin\left(\frac{n_{\text{ext}}}{n}\right) \quad (1.35)$$

Additionally, we introduce several simplifying assumptions. Firstly, we set the reflectivities of both interfaces to be constant functions of the incident angle, equal to $r_1 = 0.43$ and

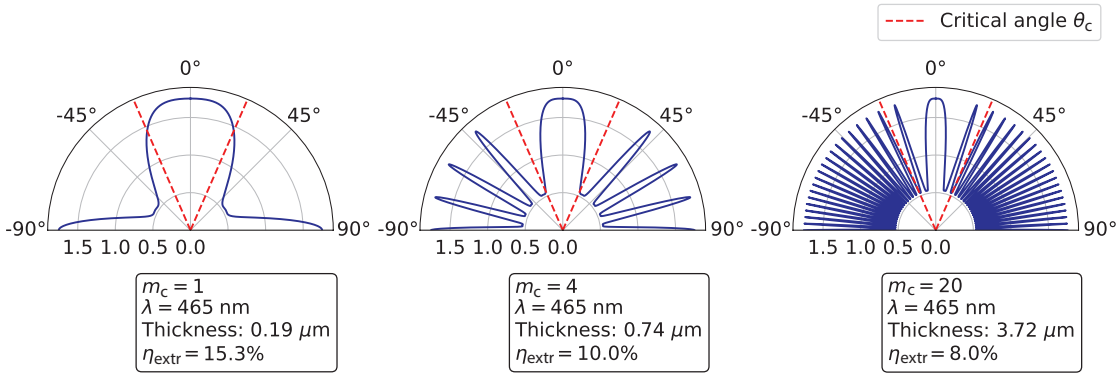


Figure 1.17: Variation of Fabry-Perot cavity thickness: We explore the impact of cavity thickness variation (L) on field intensity within a Fabry-Perot cavity. In this scenario, the reflectivities of both interfaces are fixed ($r_1 = 0.43$ and $r_2 = 0.29$), the light source is placed at the cavity center ($z = \frac{L}{2}$), and $n = 2.5$. The red dashed line represents the critical angle, dividing the region where intensity couples effectively to free space. The three subfigures correspond to specific integer cavity orders: $m_c = 1, 4,$ and 20 , from left to right. On each subfigure we see m_c Fabry-Perot modes excited by the embedded emitter (in each quarter space). The transition from thick-cavity to microcavity regimes is evident as the cavity size decreases: the two left cavities couple only one mode to the light cone.

$r_2 = 0.29$.² Secondly, we position the light source at the center of the cavity ($z = \frac{L}{2}$). Under these conditions, we calculate the intensity at the top of the cavity, and show the results in Figure 1.17. The values used for this calculation are $n = 2.5$, $n_{\text{ext}} = 1$, and we vary the cavity thickness. Note that only the intensity corresponding to $\theta < \theta_c$ is effectively coupled to the free space above the cavity, because $r_1(\theta > \theta_c) = 1$. The red dashed line corresponds to this condition, thereby delimiting what is called the *light cone*.

The three given values of the cavity thickness are specific. They correspond to integer cavity orders m_c , defined as:

$$m_c = \frac{nL}{\lambda} \tag{1.36}$$

Conditioning this quantity to be an integer forces the intensity of the field to be maximal when $\theta = 0$. Here, from left to right, $m_c = 1, 4$ and 20 . The rightmost subfigure shows many peaks, *i.e.* many Fabry-Perot modes excited by the embedded emitter. More precisely, this cavity length supports exactly $m_c = 20$ modes. As we decrease the cavity size, we transition from the thick-cavity regime ($L \gg \lambda$) to the *microcavity regime*. The transition happens when estimating the extraction efficiency from solely the ratio between the solid-angle below and above the critical angle does not hold anymore. This happens when we start to support few modes in a cavity, when mainly one mode remains coupled to the free-space. As a matter of fact, the first two cases of Figure 1.17 correspond to microcavities.

²These values correspond to the reflectivities we expect when the cavity medium is GaN on Si, with air above, at $\theta = 0^\circ$.

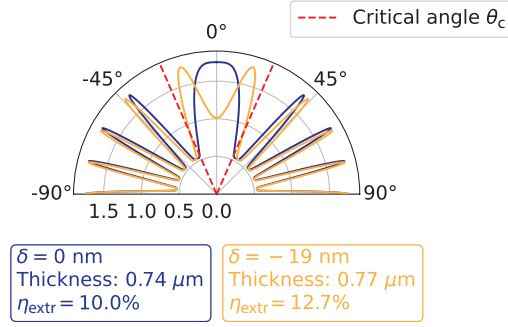


Figure 1.18: Optimal detuning impact on the same cavity as in Figure 1.17 with $m_c = 4$. The $\sim 30 \text{ nm}$ cavity detuning implementation is critical, since applied in the wrong direction it can change a 27% η_{extr} enhancement into a 38% degradation, in the present case.

We can now calculate the extraction efficiency η_{extr} in a more precise manner. This quantity is simply defined as the intensity coupled to the external medium to the total intensity within the cavity:

$$\eta_{\text{extr}} = \frac{\int_0^{\theta_c} I_1 \sin\theta \, d\theta}{\int_0^{\pi/2} I_1 \sin\theta \, d\theta} \quad (1.37)$$

We used this analytical formula to compute the values of η_{extr} given in the figure, but there are two approximations for the two regimes. In the thick cavity regime $L \gg \lambda$, the ratio of the solid-angles yields $\eta_{\text{extr}} \approx \frac{n_{\text{ext}}^2}{n^2}$. When the cavity is thin enough, $L \sim \lambda$, we can estimate $\eta_{\text{extr}} = \frac{1}{m_c}$. From this, we can conclude that the thinner the cavity, the better it is regarding extraction efficiency. This is well exemplified in Figure 1.17, where we see that from $\eta_{\text{extr}} = 8.0\%$ in the thick-cavity regime we jump to $\eta_{\text{extr}} = 15.3\%$ for the thinnest microcavity, almost doubling the light extraction. Of course, extraction can be enhanced by roughening the surface.

1.5.5 Detuning

Another way of maximizing the light extracted to the light cone is to detune the cavity length from the ideal value of $\frac{m_c \lambda}{n}$, such that a considerable portion of two symmetric modes lie within θ_c . We define the detuning δ as:

$$\delta = \lambda - \frac{nL}{m_c} \quad (1.38)$$

whose optimal value can be expressed as:[76]

$$\delta_{\text{opt}} = -\lambda \frac{n_{\text{ext}}^2}{4n^2} \quad (1.39)$$

Note that here, the light is not extracted with $\theta = 0$, but diagonally, thereby affecting the far-field pattern of the device, as shown in Figure 1.18. Another important consideration is that such cavity detuning must be very accurately applied: it consists of only $\sim 30 \text{ nm}$, and the

Chapter 1. Background information

modification in the wrong direction (removing material instead of adding, in the present case) would have a dramatic impact on the extraction efficiency — from increasing η_{extr} by 2.7%, $-\delta$ would reduce it by 3.8%.

Finally, the whole considerations of this section dealt with a monochromatic light source. To take into account the emission of a QW from the present study — whose full width at half maximum (FWHM) usually spans 20–30 nm — the present extraction calculation needs to be conducted and ponderated by the relative emission at each wavelength value. To do these more complex simulations, we use an open-source software, the principle of which is described in Section 5.2. The advantage of such a numeric solver is that it enables the consideration of the complete epilayer design, with all interfaces and index variations.

1.6 Electrical injection

To build real-world light-emitting devices such as LEDs or laser diodes (LDs), electrically injecting the active region is needed. This can be achieved by growing the active region (in our case, QWs) between an electron-reservoir (the n -type doped material) and a hole-reservoir (the well-known p -type material). The dopant concentrations are respectively noted N_A (p) and N_D (n). Bringing these two materials together in the same device is why we call it a p - n junction. From the rather abrupt junction, the semiconductor bands bend, which in turn provokes diffusion of carriers, hence a field. Around the junction, the specific region where diffusion and drift balance each other is called the space-charge region. As a consequence, there exists a built-in potential writing:[77]

$$V_D = \frac{k_B T}{q} \ln \left(\frac{N_A N_D}{n_i^2} \right) \quad (1.40)$$

with n_i the intrinsic concentration of carriers in the semiconductor and k_B is the Boltzmann constant. When one applies an external bias V , the width of the depletion region (where mobile carriers are absent) changes. To inject electrons and holes in the active region, a forward bias has to be applied, which creates a current density J through the diode:[78]

$$J = q \left(N_A \sqrt{\frac{D_p}{\tau_p}} + N_D \sqrt{\frac{D_n}{\tau_n}} \right) \exp \left(q \frac{V - V_D}{k_B T} \right) \quad (1.41)$$

where D_n , D_p are the electron and hole diffusion coefficients and τ_n , τ_p the minority carrier lifetimes.

In reality, a device can behave differently. To model real-world devices, an empirical law is used:[59]

$$J \approx J_s \exp \left(\frac{qV}{\eta_i k_B T} \right) \quad (1.42)$$

where η_i is the ideality factor. From the value of this factor, we can draw conclusions about the injection regimes: when diffusion dominates, $\eta_i = 1$ while as the current density decreases and

1.7 Current understanding of InGaN quantum well efficiency

nonradiative SRH processes take over, $\eta_i = 2$. We find the latter value also in QW-based LEDs.

1.7 Current understanding of InGaN quantum well efficiency

Now that we have a comprehensive knowledge of the context of III-Ns and of the main concepts relative to the present study, let us spend this last section on a review about the current state of the research specific to InGaN/GaN QWs efficiency.

Since the first report of candela-class blue LEDs [1], a question appeared. The samples used to demonstrate such efficiencies, with InGaN/GaN QWs heteroepitaxially grown on *c*-plane sapphire substrates, exhibited TD densities $> 10^9 \text{ cm}^{-2}$ [2–4]. Nonetheless, such a density did not hinder efficient light emission, contrasting with other historically studied photonic devices such as red-emitting AlGaInP-based LEDs, where a dislocation density higher than 10^3 cm^{-2} causes a tenfold drop in efficiency[3], or GaAs-based devices [5, 6]. This observation of high efficiency in defective III-Ns was the genesis of a debated topic in our field, questioning the nonradiative behaviour of TDs.[7, 8]

1.7.1 Threading dislocations and V-pits in bulk materials

Dislocations in GaN

Shortly after the focus on III-Ns for blue light emission, Wu *et al.* [79] studied the morphology of samples, and found that growth grains are surrounded by mostly a-type and a+c-type TDs. Adding on this observation, Hino *et al.* [80] found also samples embedding mostly a-type and a+c-type TDs forming small V-shaped pits. The presence of some c-type TDs was correlated with the formation of nanopipes, leading to bigger pits at the surface. The samples under scrutiny had approximately the same a-type TD density, while the variation in c-type TD density had no influence on the efficiency, contrarily to changes in a+c-type TD densities. Hence, the researchers concluded that a+c-type TDs are NRCs. *A contrario*, three years later, Yamamoto *et al.* [81] performed transmission electron microscopy (TEM)-CL, and concluded that from the observation of mainly a-type and some a+c-type TDs, a-type TDs were to be inculcated as NRCs. Later, Albrecht *et al.* [82] issued a consensual finding from CL measurements: both a-type and a+c-type TDs are active NRCs.

On the nanoscale structural properties of TDs, Moram *et al.* [83] built upon the considerations of Wu *et al.* [79] about nucleation islands. From this study, a+c-type TDs form a-type TDs after 100 nm, or merge into loops and do not cluster, while a-type TDs move during growth and cluster into more stable low-energy arrays. This clustering was also observed by Naresh-Kumar *et al.* [84], on the other hand finding all types of TDs in isolated positions. The relative proportions of TDs they observed are reported in Table 1.3

Chapter 1. Background information

Table 1.3: TD nature proportion observed by Naresh-Kumar *et al.* [84].

	Edge (a-type)	Screw (c-type)	Mixed (a+c-type)
TD proportion	60%	<2%	38%

1.7.2 Localisation in InGaN as a threading dislocation protection

The consideration of InGaN alloys adds a variable to this already complex problematic of dislocations and V-pits. The research by Chichibu *et al.* [9] led to hypothesizing that localisation centers due to In inhomogeneities, further modeled by Filoche *et al.* [10], reduce the diffusion of carriers and prevent their nonradiative recombination in the vicinity of TDs. Completing this version, Massabuau *et al.* [85] pointed out that one should not consider solely the geometric effects from V-pits forming barriers around TDs (see the next section). Rather, researchers proposed that the tensile region due to edge component (higher energy for a+c-type TDs than a-type TDs) leads to In segregation, forming In-N-In chains prone to localise carriers. Their results also show a-type TD bundles at V-pits facets, as was previously observed.[79, 83, 84] They concluded that all TDs are active NRCs in InGaN, like Albrecht *et al.* [82].

1.7.3 Threading dislocations and V-pits in InGaN quantum wells

The structural correlation between TDs and V-pits was observed early, as the latter form upon the former.[80] This can have consequences in samples containing QWs: Sharma *et al.* [86] observed that if V-pits contain QWs (their sample embeds multiple quantum wells (MQWs)), these are likely broken. Researchers went further, and ascribed the opening of V-pits to QWs growth. Cherns *et al.* [87] join Sharma *et al.* [86] on the fact that QWs in V-pits are disrupted. They add that a-type TDs do not form V-pits and are more detrimental than a+c-type TDs upon which V-pits simply act as dead layers. The finding of Sharma *et al.* [86] shows that there is, as observed by Massabuau *et al.* [85], a complex intricacy between TD-caused strain, In content and V-pits. Further evidence came from Watanabe *et al.* [88] who performed TEM morphological analyses, showing evidence that V-pits form from TDs. Furthermore, their study shows that the V-pits are generated at positions where there is hint for In-segregation. Their findings also point toward thinner QWs in the vicinity of V-pits. Adding to TEM studies, Henley and Cherns [89] performed also CL analyses. From TEM, they saw a very vast majority of a-type TDs and observed that small V-pits originate just below the QWs, while bigger ones are already present almost from the substrate. From the CL measurements, the authors attribute the decrease of luminescence toward the center of the V-pits to (i) a perfect nonradiative behaviour of TDs (mainly a-type) and (ii) the diffusion of carriers outside the V-pit, due to its inherent energy barrier. On the other hand, these researchers also performed high e-beam current irradiation of the wells, and observed an increase in the carrier diffusion lengths. They conclude that this leads to temporary electronic changes in the material, *e.g.* charging trap states, thereby preventing carriers to reach and stay in potential minima. These authors attribute these minima to small-scale fluctuations of the In content, but do not exclude the

1.7 Current understanding of InGaN quantum well efficiency

eventuality of the presence of impurities.

Contender of the In-caused transformation of TDs into V-pits are Tomiya *et al.* [90], who revisit the study of Watanabe *et al.* [88], and from their non-observation of In-segregation at V-pits apices, attribute the generation of V-pits to low temperature growth of GaN. Nonetheless, such constataions paved the way to V-pit engineering by giving methods to act on V-pits. For example, Takahashi *et al.* [91] found that intentional V-pits can be beneficial for room-temperature PL, and a tentative mechanism emerged: Hangleiter *et al.* [92] conclude from TEM observations and V-pit engineering considerations that since QWs are thinner within V-pits, a larger f_{osc} and a lower QCSE lead to potential barriers, screening the nonradiative TDs from the carriers. Netzel *et al.* [93] built upon the previously developed picture, by drawing conclusions on localisation phenomena from PL measurements, taken on a wide range of morphologically characterised samples. Eight years later, Okada *et al.* [94] performed atomic force microscopy (AFM) morphological assessments, and PL and scanning near-field optical microscope measurements, on samples with varying V-pit sizes. What they found is an optimal V-pit size of 100 nm, which they explain by a trade-off between a sufficient energy barrier around the TDs and formation of dead surfaces, and contribute thereby to the visions of quite a few other teams, *e.g.* Sharma *et al.* [86], Cherns *et al.* [87], Henley and Cherns [89], Hangleiter *et al.* [92], and Netzel *et al.* [93]. This topic remains debated, and recent articles still add interesting insights. Bojarska-Cieślińska *et al.* [95] performed scanning electron microscopy (SEM), TEM and CL studies and concluded that the larger V-pits they observed form upon a+c-type TDs, whereas the small ones are due to a-type TDs. From their observations, mainly the latter are responsible for nonradiative recombinations. It has to be noted that contrarily to other studies, their QWs do not exhibit V-pits at edge dislocations, hence pit-induced energy barriers are unlikely. On the localisation topic, their study points toward an In-dependent carrier diffusion length, in the same idea as Henley and Cherns [89].

1.7.4 Threading dislocations and V-pits in devices

It is of crucial importance not to forget that all these studies are conducted on laboratory samples with optical injection methods, and that the implementation of these materials into devices can open other challenges with regard to the afore-mentioned defects. For example, Usami *et al.* [96] concludes that pure c-type TDs have closed cores (as previously observed by Hino *et al.* [80]) and lead to considerable leakage currents in LEDs, lost for QWs injection: η_{inj} is thereby greatly degraded. On the other hand, Ewing *et al.* [97] observed a bimodal distribution of V-pits, where some form deep in the structure, at an In-containing SL, while the others, smaller, form during the MQW growth. They conclude that "neutralising" TDs, responsible for current leakage, by transforming them early into V-pits, is a good strategy.

Recently, another interesting idea emerged: using V-pits to inject QWs more efficiently and uniformly. Quan *et al.* [98] have done numerical simulations, confirming the overall nonradiative nature of TDs, and showing that V-pits effectively build energy barrier around them.

Chapter 1. Background information

Noteworthy, it is explained that the lower In content in V-pit sidewalls as well as their semi-polar nature facilitates lateral hole injection into the QWs. This study was completed by further work from Zhou *et al.* [99], using the technique of low temperature growth documented by Tomiya *et al.* [90] to open V-pits on purpose. Ho *et al.* [100] have demonstrated that this is especially beneficial for greener emitters, where random alloy fluctuation does not help vertical carrier injection anymore, which makes lateral injection of QWs through V-pits a good option. This method of V-pit engineering was demonstrated to be an efficient approach for red wavelengths.[97]

2 Sample fabrication and basic properties

In this chapter, we will discuss the design, growth and characterisation of the main samples of the present study. *De facto*, these steps are tackled each time one needs samples to test an idea: from the hypothesis, we design a sample challenging the thought experiment. From there, Dr. J.-E. Carlin grows the epilayers with a specific set of requirements (*e.g.*, emission wavelength, thickness, QW thickness, etc.), by MOCVD. Then, we field-check the sample by first performing photoluminescence mappings. If the characterisation appears to be in line with the scope of the study, we proceed with further measurements so as to determine the specificities of each of the samples (*e.g.*, electron microscopy, AFM, temperature-dependent PL — and, in the next chapter, power-dependent PL).

2.1 Growth

In this study, we prepared III-N samples grown on Si(111) substrates by MOCVD in an Aixtron 200/4 RF-S low-pressure horizontal reactor, the operating principle of which is sketched in Figure 2.1. The metalorganic precursors, carried by H_2 or N_2 , introduce the metallic atoms into the growth chamber, where a reaction with ammonia NH_3 at the sample surface produces the crystalline III-Ns.

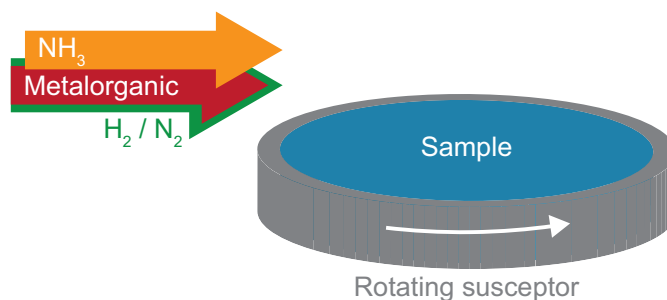


Figure 2.1: Principle scheme of a MOCVD horizontal growth reactor.

Chapter 2. Sample fabrication and basic properties

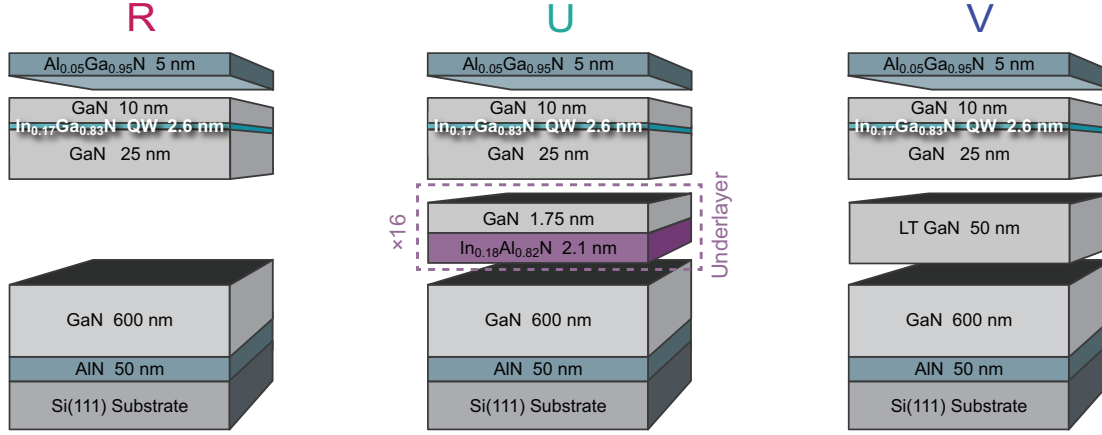


Figure 2.2: Thickness of the layers in the three samples. Notice the presence of a 16-period In-containing SL-UL below the QW as an exclusivity of sample U.

In the design of a Si-grown GaN epilayer, the problem of melt-back etching is mitigated through the first growth of a thin 50 nm AlN buffer.[24–26] Note that using such a nucleation layer also proved to help for growth on sapphire.[101]

Above the AlN nucleation layer, a 600 nm-thick GaN buffer is deposited. A minimum thickness is needed to planarize the surface. Obviously, such a 600 nm thickness will not allow to reach the lowest TD densities obtained *via* strain-mitigation methods with low temperature AlN interlayers, that needs usually a few microns.[24] We should therefore be in the interesting regime of high TD densities, $> 10^{10} \text{ cm}^{-2}$. The ~ 700 nm total thickness of our layers also allows to stay below the thickness where layers exhibit cracking.

The active region of the three main samples of the study, extensively examined in Chapter 3, consists of a 2.6 nm $\text{In}_{0.17}\text{Ga}_{0.83}\text{N}$ single quantum well (SQW). The bottom and top barriers are GaN layers of thicknesses 25 nm and 10 nm, respectively. To hinder surface recombination, the growth was terminated by a 5 nm-thick $\text{Al}_{0.05}\text{Ga}_{0.95}\text{N}$ cap. The thickness of this cap was chosen to allow for high spatial CL measurements detailed in Chapter 4. The growth temperature for the layers, from bottom to top (AlN, GaN buffer, InGaN QW, AlGaN) were $T_{\text{AlN}} = 950^\circ\text{C}$, $T_{\text{GaN}} = 970^\circ\text{C}$, $T_{\text{InGaN}} = 750^\circ\text{C}$, and $T_{\text{AlGaN}} = 770^\circ\text{C}$. Let this reference sample be called R, represented in Figure 2.2 (left).

We describe two more samples: U embeds an InAlN/GaN SL-UL below the QW, to reduce the PD density in the active region. Indeed, as discussed in Section 1.1.1 and described in Armstrong *et al.* [15] and Haller *et al.* [16], an In-containing UL allows to trap the growth-generated SDs. Growing this layer below the QW hence drastically reduces the density of PDs in the active region, as sketched in Figure 2.3. We chose a SL-UL design with 16-period of lattice-matched $\text{In}_{0.18}\text{Al}_{0.82}\text{N}$ (2.1 nm)/GaN(1.75 nm), which has proven to be an efficient trapping system.[16, 102] A third sample, V, instead of a SL-UL, integrates a 50 nm low-temperature (750°C) grown GaN layer, on purpose opening larger V-pits.[90, 99] The structure of the samples

2.2 Structural properties

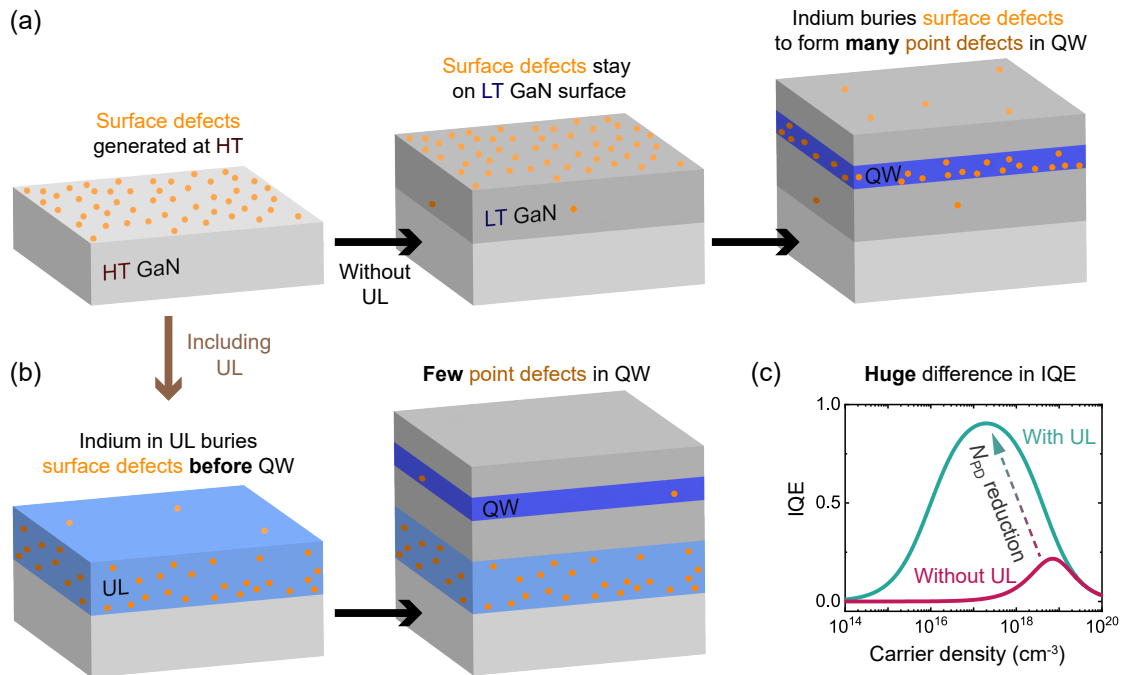


Figure 2.3: Mechanism of the UL. (a) Without an UL, SDs generated during high-temperature growth of GaN are incorporated when the In-containing InGaN QWs are grown. (b) Adding an In-containing UL allows to trap these defects below the QWs. (c) This allows to drastically increase the emission efficiency. Adapted from Weatherley [35].

is shown in Figure 2.2.

2.2 Structural properties

This section is dedicated to the morphological analyses of the presented samples.

2.2.1 Scanning electron microscopy

Experimental method

To have a high-resolution information about the samples' surface exhibiting features of the order of 1–10 nm, we need to ensure the resolution limit is below. Simply from the wavelength λ and the numerical aperture NA , we can estimate the diffraction-limited resolution r of the system:

$$r = \frac{1.22\lambda}{NA} \quad (2.1)$$

where $NA < 1$. As a consequence, resolving 10 nm features would require $\lambda < 8.2$ nm, even in the limit of $NA \sim 1$. Therefore, optical microscopy is not an option. Hopefully, we can consider again the de Broglie wavelength we introduced in Section 1.2, for electrons. This quantity can

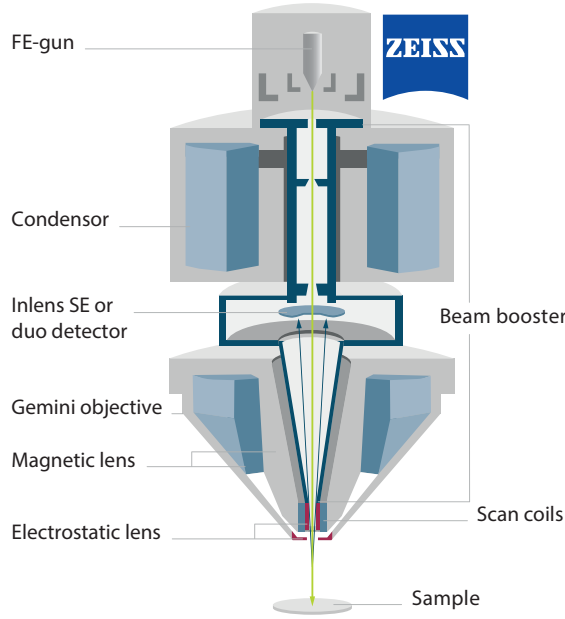


Figure 2.4: Gemini II SEM column, integrated in the Merlin microscope used for the present thesis. Adapted from Zeiss.

also be expressed as:

$$\lambda_{DB} = \frac{h}{p_e} \quad (2.2)$$

where $p_e = \frac{1}{c} \sqrt{E_b^2 + 2E_b m_0 c^2}$ is the electron momentum expressed as a function of its kinetic energy $E_b = 3 \text{ keV}$ and mass $m_0 = 9.11 \times 10^{-31} \text{ kg}$. If we assume λ_{DB} to be an upper bound of the theoretical resolution for an electron microscope, we deduce a resolution of $\sim 0.02 \text{ nm}$, well better than the optical resolution limit. Naturally, such an estimation does not take into account electron scattering phenomena, which usually degrade the resolution by adding noise in a few nanometers of diameter. Monte-Carlo simulations can take this into account, as will be seen in Chapter 4 for CL measurements.

For the measurements, we used a Zeiss Merlin SEM, which embeds a Gemini II column, reproduced in Figure 2.4. The electron source is a Schottky field emission gun (FEG), a heated filament to which an extraction voltage is applied. The acceleration voltage is applied to the whole column, $V_{acc} = 3 \text{ kV}$ for the precedent calculation. The detectors either collect secondary electrons (SEs) and backscattered electrons (BSEs). This thesis' measurements rely principally on SEs.

Image analysis

Once images were acquired, we performed statistical analysis on the V-pits visible at the surface. The method was to image different places of the samples, and do (i) pit counting and (ii) pit diameter d_{V-pit} estimation. In Figure 2.5, we show five areas for each sample.

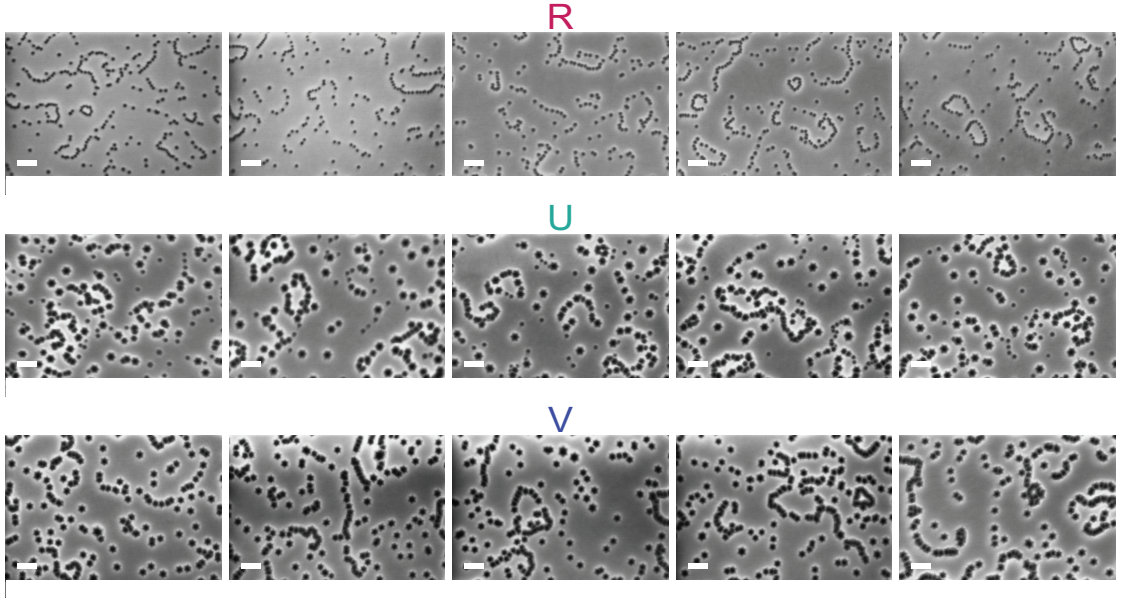


Figure 2.5: Series of SEM images of the three above-mentioned samples R, U and V. The acceleration voltage was set to $V_{\text{acc}} = 3 \text{ kV}$ and the magnification was $100'000\times$. The scalebars are all 100 nm.

Table 2.1: V-pit surface density $N_{\text{V-pit}}$ and mean diameter $d_{\text{V-pit}}$ for the three samples R, U, V.

Sample	R	U	V
V-pit density ($\times 10^{10} \text{ cm}^{-2}$)	3.3 ± 0.4	2.5 ± 0.3	2.4 ± 0.2
V-pit mean diameter (nm)	20.0 ± 2.4	21.4 ± 3.0 and 41.4 ± 4.6	40.2 ± 3.7

Results and discussion

The above-mentioned microscopy technique is a top-view method, which means that we only have a surface morphology assessment. Nonetheless, as described in the precedent chapter, the V-pits visible at the samples' surface originate from TDs. We can therefore assess a lower bound for TD densities N_{TD} in our samples by performing SEM imaging. The measurements of Figure 2.5 yield the data reported in Table 2.1. The TD densities are all in the low 10^{10} cm^{-2} regime, as expected from the growth of thin GaN on Si. We can see that sample R has the smallest V-pits of the three: $d_{\text{V-pit, R}} = 20.0 \pm 2.4 \text{ nm}$. In sample U, we observe a clear bimodal distribution of the V-pit sizes, one centered on $21.4 \pm 3.0 \text{ nm}$ and the other on $41.4 \pm 4.6 \text{ nm}$. We propose that In in the SL-UL triggers the opening of the larger V-pits, as hypothesised by Watanabe *et al.* [88], while the smaller ones undergo the same formation mechanisms as the V-pit population of Sample R (see Section 1.7). On the other hand, sample V only has V-pits of size $d_{\text{V-pit, V}} = 40.2 \pm 3.7 \text{ nm}$, indicating that the low temperature GaN layer (at the same depth as the SL-UL of sample U) successfully opens the V-pits deeper in the epilayer, generating larger V-pits at the surface. The fact that $d_{\text{V-pit, V}}$ is similar to the mean diameter of the largest

Chapter 2. Sample fabrication and basic properties

V-pit population of sample U confirms that the presence of an In-containing UL generates the opening of the larger V-pits. Note that from these observations, a low temperature GaN layer is a more reliable way than In-containing layers to transform TDs into V-pits.

Another interesting feature of our micrographs is the distribution of V-pits along loops, as already documented by other groups. We suppose these V-pit loops to form from TD arrays in the structure, corresponding to grain boundaries.

There remains a question: is there a one-to-one correspondence between surface V-pit densities $N_{V\text{-pit}}$ and TD densities N_{TD} ?

2.2.2 Transmission electron microscopy

To answer this question, we need to have insight into the structural properties of the epilayers. To do so, cross-sectional TEM is well-suited.¹

Sample preparation and general aspects

First, a very thin layer of material is prepared by focused ion beam (FIB). A Zeiss NVision 40 instrument was used to lift-out 180 nm-thick lamellas parallel to the $(1\bar{1}00)$ crystallographic plane. Such a complex sample preparation and heavy equipment is paid-back in terms of a very high resolution, down to the atomic scale. This is enabled by the highly energetic electron beam generated in the FEI Talos F200S TEM, above 100 keV. The principle of the TEM column is similar to that presented in Figure 2.4, with a design adapted to two orders of magnitude increase in the electron energy. When the electrons interact with the lamella, diffraction happens and an image is formed onto a detector beyond. The analysis of the diffraction patterns, through complex methods more detailed in Oveisi [103], allows to produce real-space images of the atomic arrangements in the sample. To fully understand the analyses we provide hereafter, we need to detail some aspects of TEM imaging of crystals.

Diffraction patterns and crystal TEM imaging

Usually in TEM, the sample is illuminated by a uniform, coherent electron beam. To form a so-called bright-field (BF) image as in Figure 2.6 (left), only the minimally scattered electrons are transmitted after the objective lens. This corresponds to selecting electrons undergoing $0\mathbf{g}$, where \mathbf{g} is the diffraction vector. The TDs create the wavy, longline bright and dark contrast changes by diffracting electrons. In dark-field (DF) imaging mode, the transmitted electrons are the diffracted ones, having $1\mathbf{g}$ along the optical axis, leading to a dark background and bright features corresponding to electrons being deflected by TDs (*cf* Fig. 2.6, center). From the figure, it is clear that these two modes do not allow for maximal TD contrast. In the third

¹The imaging was performed at the Interdisciplinary Centre for Electron Microscopy with the expertise of Dr. D. Alexander.

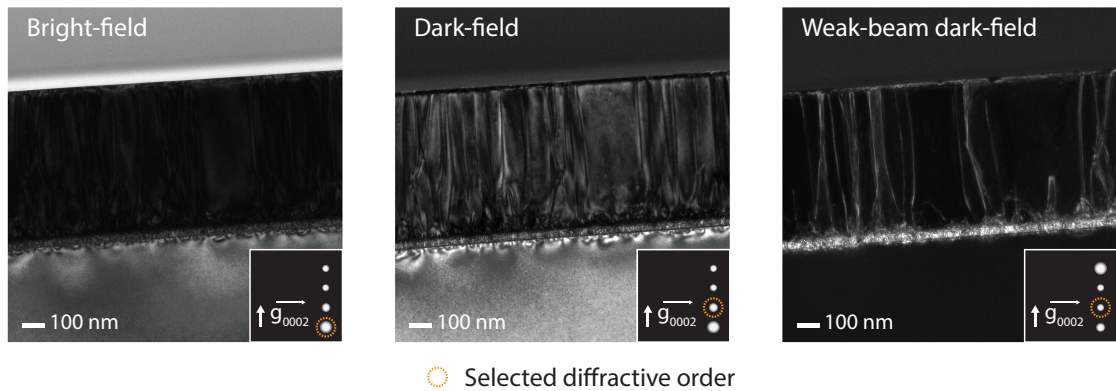


Figure 2.6: In TEM, (a) BF imaging captures minimally scattered electrons, (b) DF imaging uses diffracted electrons for contrast, and (c) tilted samples under the Bragg condition for $3\mathbf{g}$ reflection maximize TD contrast. The insets show the corresponding diffraction patterns. The *invisibility criterion* links \mathbf{g} orientation to TD contrast, allowing $\mathbf{g} \cdot \mathbf{b}$ analysis for selective TD studies.

image of Figure 2.6, we still select the $1\mathbf{g}$ electrons, but this time we tilt the sample to realise the Bragg condition for $3\mathbf{g}$ reflection. On a diffraction pattern (*cf* Fig. 2.6, rightmost inset), the $3\mathbf{g}$ spot is now the brightest. The consequence of this is that fewer electrons reach the detector, being more strictly selected: the contrast of TDs is maximised.

The condition to see dislocations is to orient the operative diffraction vector \mathbf{g} in the same direction as the TD's Burgers vector \mathbf{b} . On the contrary, having $\mathbf{g} \cdot \mathbf{b} \sim 0$ will cause electrons to be minimally affected by the given dislocation, causing a total loss of contrast, and invisibility of this TD. This is called the *invisibility criterion*, allowing so-called $\mathbf{g} \cdot \mathbf{b}$ analysis: by choosing along which crystallographic orientation \mathbf{g} is oriented, it is possible to select a given type of TDs. Therefore, to perform such analyses, there is a constraint on the way to fabricate the sample lamellas, parallel to the $(1\bar{1}00)$ crystallographic plane in our case.

Application to TDs in III-N

In our study, we are interested in visualising three types of TDs. Edge or a-type TDs, with a Burgers vector along $\mathbf{b} = \frac{a}{3}\langle 11\bar{2}0 \rangle$, can be made invisible with $\mathbf{g} = (0002)$, like in Figure 2.6. Screw or c-type TDs have their Burgers vector following $\mathbf{b} = \langle 0001 \rangle$, yielding $\mathbf{g} \cdot \mathbf{b} = 0$ for $\mathbf{g} = (11\bar{2}0)$. Hence, mixed TDs can be seen under both imaging conditions.[104] On the example of Figure 2.6, the only TDs we can see are screw and mixed ones. By comparing the same region under the two imaging conditions, it is possible to identify each type of TD and count them. I performed a statistical investigation over a few microns on samples R and U, whose example of TEM images are shown in Figure 2.7. The results are reported in Table 2.2 and compared to the SEM $N_{V\text{-pit}}$ values.

From the analysis, the total TD densities amount to $2.3 \pm 0.3 \times 10^{10} \text{ cm}^{-2}$ and $2.1 \pm 0.3 \times$

Chapter 2. Sample fabrication and basic properties

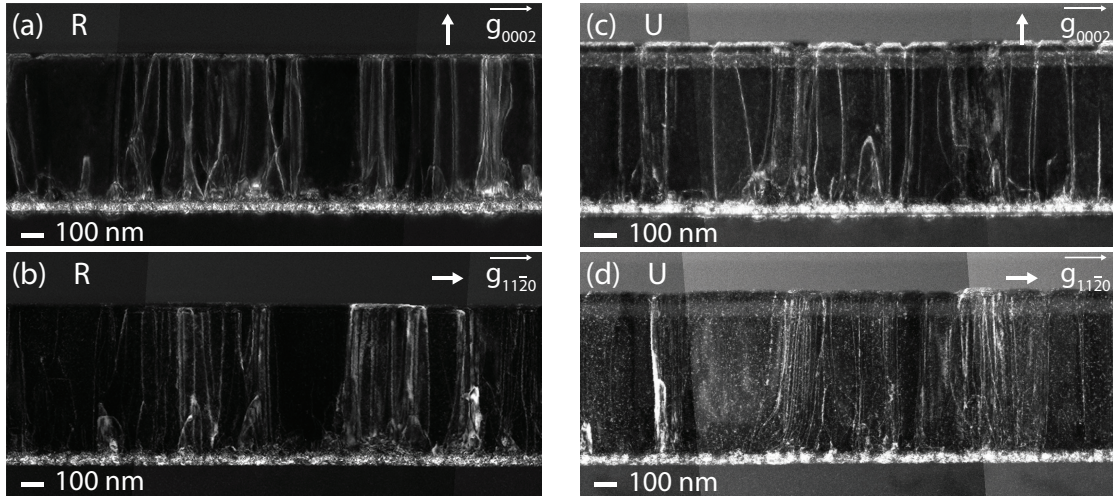


Figure 2.7: Same regions of the samples R (a)-(b) and U (c)-(d) under two different TEM measurement conditions. (a),(c) a-type edge TDs are made invisible with $\mathbf{g} = (0002)$ while (b),(d) c-type screw TDs vanish with $\mathbf{g} = (1120)$. Mixed TDs are visible under both conditions.

Table 2.2: V-pit density, TD densities, and dislocation nature, assessed from top-view SEM and cross-sectional TEM analyses.

Sample	SEM		TEM		
	V-pit Density (10^{10} cm^{-2})	TD Density (10^{10} cm^{-2})	Mixed	Screw	Edge
R	3.3 ± 0.4	2.3 ± 0.3	37%	18%	45%
U	2.5 ± 0.3	2.1 ± 0.3	44%	8%	48%

10^{10} cm^{-2} for samples R and U, respectively. To explain the slight decrease of N_{TD} compared to the SEM $N_{\text{V-pit}}$ values, we invoke the fact that TDs may overlay in the 180 nm-thick FIB lamellas. We can therefore conclude:

$$N_{\text{TD}} \approx N_{\text{V-pit}} \quad (2.3)$$

In our samples, we found that nearly half of the TDs were pure edge, and that only a minority were pure screw. These observations are in line with the literature, as stated in Section 1.7.

In addition, there is evidence of growth grain misorientation in the TEM images. The hint for this is that there are some parts of the image, here on sample R, where the contrast vanishes. A misoriented grain could cause such a phenomenon because the diffracted electrons would not be selected by the image-forming optics, aligned for the main class of grain orientations. As explained in Section 1.1.1, the higher coherence along the c-axis explains why misorientations can remain throughout the epistructure.

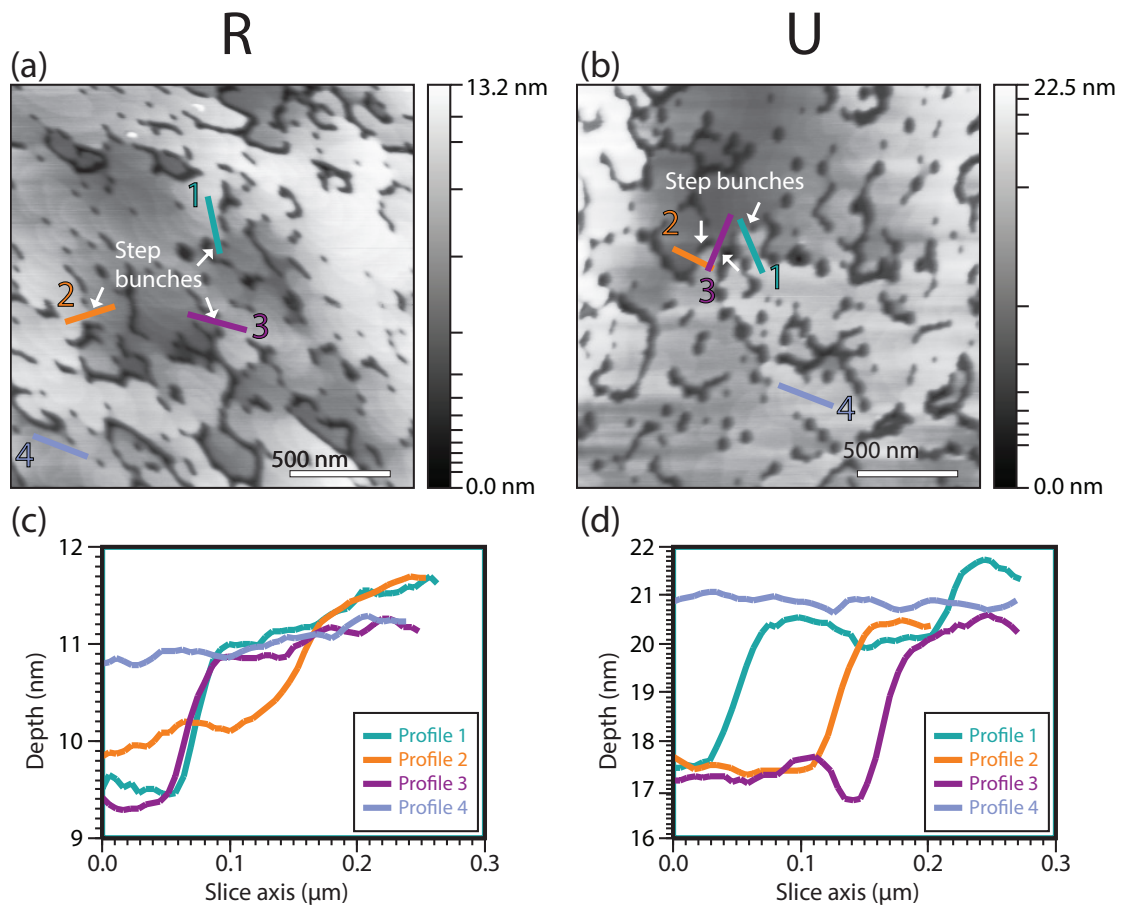


Figure 2.8: (a)-(b) AFM measurements showing the topography of the samples R and U. The arrows present growth-generated domain limits, coinciding with clear step-bunching. (c)-(d) Vertical profiles along the colored lines in (a)-(b).

2.2.3 Atomic force microscopy

A complementary surface-morphology measurement method is AFM, allowing to probe the topology of the surface in a precise manner. This scanning probe microscopy technique is based on the interaction of an atomically sharp tip mounted on a cantilever — whose bending is monitored by a laser — and the sample surface. Van der Waals or electrostatic interactions, for example, will cause the scanned tip to change heights, which in turn forms quite straightforwardly a topography of the sample. The resolution of this method can reach sub-nanometer levels, both laterally and vertically — mainly depending on the tip size and geometry.

We reproduce in Figure 2.8 the results of AFM measurements performed on samples R and U. Both surfaces exhibit regions of a few tens of nanometers in diameter, delimited by V-pits. These regions are supposed to have formed from growth grains. From the blue-grey linescan of Figure 2.8(c)-(d), these domains are approximately flat. On the other hand, from one domain to another the height can change quite abruptly, as deduced from the green, violet and orange

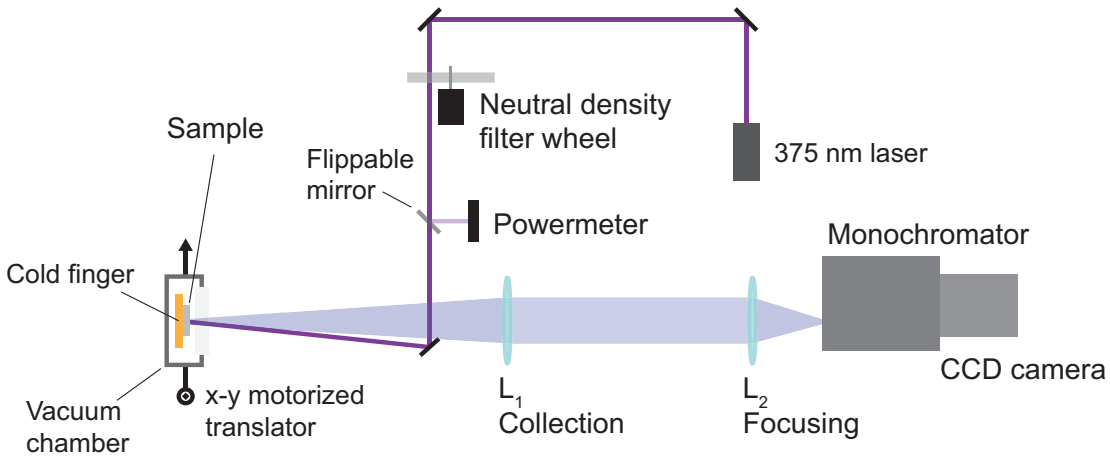


Figure 2.9: Illustration of the macro-PL setup. It involves a vacuum chamber housing a cold finger connected to a closed-cycle helium cryostat. The sample, affixed to the cold finger, can be investigated over the temperature range 12–300 K.

lines. 1–4 nm height changes correspond to 4–15 atomic layers. This happens within 10–30 nm laterally, indicating step-bunching phenomena. We attribute the steps to the coalescence of grains whose heights were close but not equal.

We could wonder what consequences these features would have on the electronic properties of the QW within these samples. It has been documented that such misorientations reduce the incorporation of In in the QWs,[54] in turn creating energy barriers for the carriers. From this observation, we could question whether if the carriers injected in the QWs overcome the domain delimitations or not, and what type of potential landscape they experience. This question is investigated in detail in Chapter 4.

2.3 Optical properties

Let us now turn toward the optical characterisations of the samples. PL is useful to investigate how a sample behaves while excited by a pump laser. The physical principle is simple: the excitation laser generates electron-hole pairs in the material, that eventually fall in the QW. Once in the QW, these pairs undergo one of the processes described in Section 1.4: SRH-, radiative-recombination or A-M process. PL is the result of radiative-recombinations from laser-excited materials.

2.3.1 Experimental method

The optical measurements of this chapter rely on a macro-PL setup, depicted in Figure 2.9. The wavelength of the pump laser is crucial: we choose a 375 nm commercial LD to excite quasi-resonantly the QW. Such an emission wavelength, corresponding to ~ 3.3 eV, should be slightly

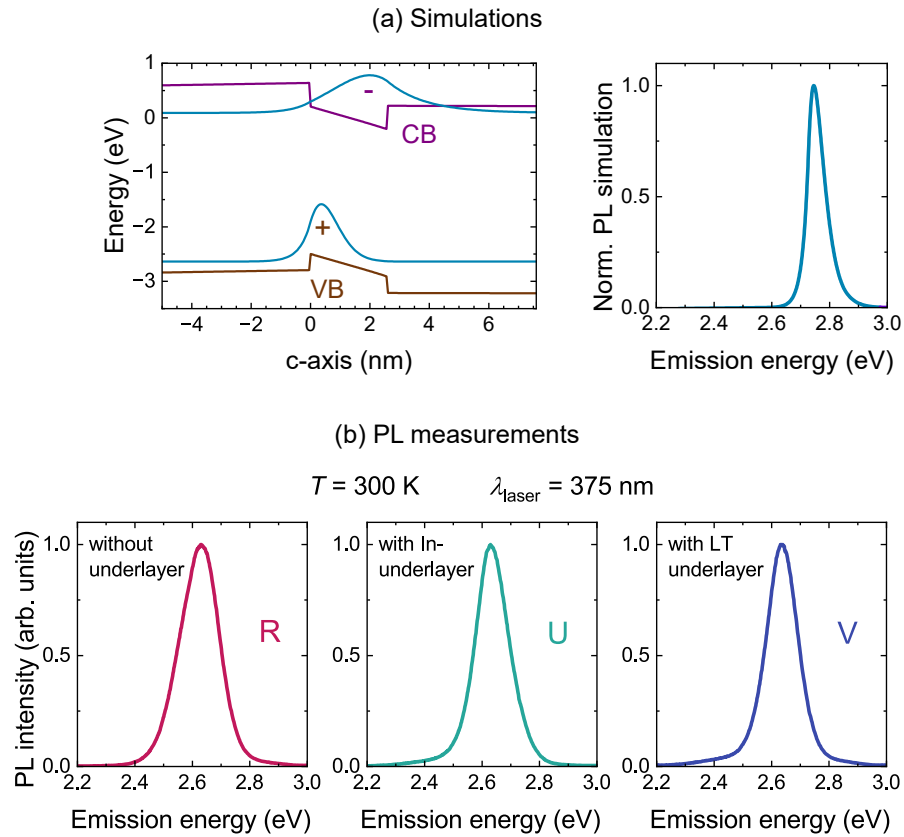


Figure 2.10: (a) Simulations for 2.6 nm-thick QW with 17% In. (b) Room-temperature PL-spectra of the sample set R, U, V, showing emission energies comprised between 2.6 and 2.7 eV. Light was collected from the cross-section of the samples to avoid interference effects.

(300-400 meV) above the absorption edge of the QWs under study.[105] This is confirmed by the PL-spectra of the above-presented samples R, U and V, shown in Figure 2.10(b), proving emission energies comprised between 2.6 and 2.7 eV at 300 K.² After being excited, the light emitted from the samples is redirected through two 2-inch lenses to a spectrometer consisting of a Jobin Yvon iHR320 monochromator coupled to a Peltier-cooled CCD detector.

Interestingly, the experimental PL spectrum is (i) at a lower emission energy than the simulated one (*cf* Fig. 2.10(a)) and (ii) broadened. First, we can explain the redshift by the Stokes shift induced by the carrier localisation in low energy potential disorder minima.[106] Second, the presence of these inhomogeneities (*cf* Fig. 1.10(a)), leads to a broadening of the experimental emission linewidth.

In the following, we will describe two measurement modes: first, PL mapping of the samples, and second, temperature-dependent PL measurements. Both measurements rely on the setup from Figure 2.9. To switch from mapping mode to temperature-dependence, the sample has

²These spectra were taken with another setup, from the side of the samples, to avoid the cavity effects mentioned in Section 1.5 to distort the measurements.

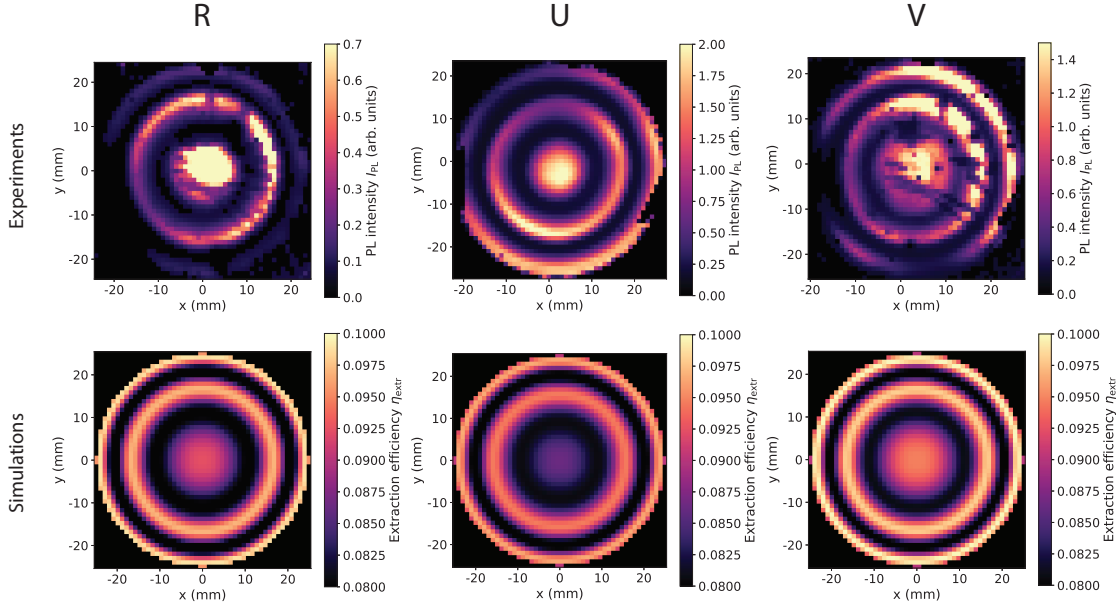


Figure 2.11: Top: Automated scanning of the entire 2-inch wafer-sized sample on the x-y motorised stage reveals concentric variations in PL intensity. Bottom: Simulations based on the Fabry-Perot cavity model with an embedded emitter, considering the designs of samples R, U, and V, provide insights into the observed concentric pattern in the PL intensity distribution.

to be transferred from the x-y motorised stage to the closed-circuit He cryostat, operating under vacuum.

2.3.2 Photoluminescence mapping

When the sample is mounted on the x-y motorised stage, it is possible to automatically scan the sample, over the whole 2-inch wafer size. Such measurements are reported in Figure 2.11 (top). The striking feature of these mappings is the concentric repartition of PL-intensity. To understand this, we need to refer to the model of a Fabry-Perot cavity with embedded emitter, described in Section 1.5. By applying this model to the actual designs of samples R, U and V (*cf* Fig. 2.2), it was possible to generate the simulations reported in Figure 2.11 (bottom) under two interesting conditions.

The first condition is to account for a thickness variation from the wafer center to the edge. This variation can be ascribed to inhomogeneities in the horizontal reactor's flux, and in the radial temperature of the sample during growth. I used a quadratic model for the thickness:

$$L = \frac{L_{edge} - L_{center}}{r_{wafer}^2} r^2 + L_{center} \quad (2.4)$$

where L_{edge} is the epilayer thickness at a distance of one wafer radius r_{wafer} from the center. To simulate the interference patterns, we need to consider a relative epilayer thickness at the

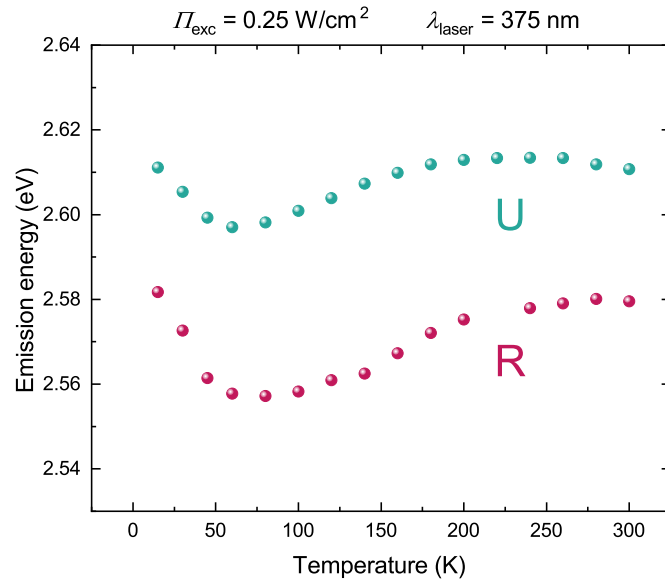


Figure 2.12: Temperature-dependent PL measurements for samples R and U. Contrary to the expected monotonic behaviour predicted by Varshni's law, the plotted curve exhibits an S-shaped trend.

sample edge $\frac{L_{\text{edge}}}{L_{\text{center}}}$ of 71%, 75% and 69% for samples R, U and V, respectively. These values show a higher radial thickness variation than the expected 10%. This discrepancy can be partially due to the voluntary simplification of considering a constant radial emission energy in our simple Fabry-Perot model.

The second output of the modelling is the deviation of the layer thicknesses for the three samples. To accurately simulate the microcavity effects observed in the PL mappings, the total thicknesses of the samples R, U and V needed to be adapted by respectively +2%, +4% and 0%, yielding cavity orders of 3.67, 4.13 and 3.69, respectively.

In conclusion, the present modelling confirms that these thin films grown on Si place the samples in the microcavity regime. As a consequence, these structures do not behave as Lambertian emitters, *i.e.*, sources of isotropic radiance. This feature will complexify the further PL analyses.

2.3.3 Temperature-dependent PL

From Section 1.1.2, we expect $E_{\text{PL}} \sim E_{\text{ph, min}}$ to essentially follow the monotoneous variation of E_{g} versus temperature, described with Varshni's law. Taking the maximum of each emission spectrum versus temperature, for samples R and U, we end up with the curve reported in Figure 2.12. The S-shaped curve does not at all follow the monotoneous Varshni's law. This was long time ago observed and studied by Cho *et al.* [107]. The conclusion of this study is that localisation effects cause the carriers to be trapped in the energy minima of the QW, including

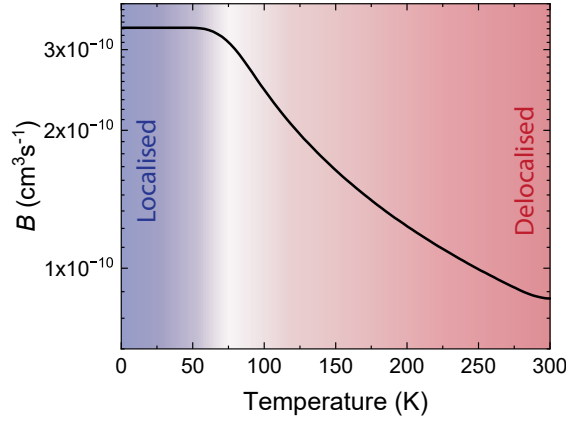


Figure 2.13: Variation of the B coefficient with T , calculated for sample R. At temperatures below $T_{\text{del, i}}$, carriers in the quantum wells (QW) are confined and experience 0D environments, leading to a constant B . As the temperature surpasses $T_{\text{del, i}}$, carriers begin to delocalise, triggering a transition to an inverse proportionality of B with temperature (T).

higher relative ones — which is why the emission energy is higher at lower temperatures but decreases as higher cryogenic temperatures allow carriers to find absolute minima. Once the temperature is enough for delocalisation to start, around $T_{\text{del, i}} \sim 70$ K and ~ 60 K for samples R and U, respectively, the emission energy increases again, due to carriers present in the whole potential landscape. Finally, temperature variation of E_g takes over at higher temperatures, above the so-called delocalisation temperatures $T_{\text{del, f}} = 280$ K (R) and 240 K (U). From the present measurements, we can roughly estimate a localisation energy of the order of 40–50 meV, which is in agreement with recent reports.[46]

Knowing the first minimum of the S-shape, we can create a simple model to compute the temperature dependence of the B coefficient in the framework of ABC model. Below $T_{\text{del, i}}$, only localised carriers can be found in the QWs, experiencing 0D confinement. Therefore, B is constant. Above $T_{\text{del, i}}$, the carriers start to delocalise, hence a transition operates toward an inverse proportionality of B to T :

$$B(T) = \begin{cases} \frac{300B_{300}}{T}, & \text{for } T > T_{\text{del, i}} \\ B(T_{\text{del, i}}), & \text{for } T < T_{\text{del, i}} \end{cases} \quad (2.5)$$

By calculating the oscillator strength of the present samples' active region from the simulation shown in Figure 2.10(a) and comparing it to what was documented on similar QWs,[33] we conclude that the value for B_{300} should be the same. This can be explained by the decrease in emission energy being compensated by the decrease in QW thickness. We show the result of the modelling of B for sample R in Figure 2.13. We will build upon this modelling in the next chapter.

Summary

We started with the description of the samples' growth method, including important aspects specific to Si(111) substrates.

We then describe and analyse the morphology of the samples, concluding that V-pit surface densities account well for the TD densities, and that edge and mixed dislocations are dominant. Also, the surface morphology determined by the AFM technique confirms the presence of growth grain boundaries materialised by TD/V-pit arrays and step-bunching. This raises questions regarding the electronic and optical consequences.

We have presented the standard PL setup. The measurements show that the samples experience critically thickness-, hence wavelength-dependent light-extraction patterns. This could prevent us from directly comparing their absolute PL intensity.

Finally, from the temperature-dependent PL measurements, we extracted localisation / delocalisation temperatures, allowing to model the temperature variation of the B coefficient.

The present characteristics of the samples ask to first investigate rigorously their relative efficiencies to determine the impact of growth method differences (see Chapter 3), and, second, try to understand electronic and optical phenomena at the scale of the defects (see Chapter 4).

3 Impact of the underlayer on InGaN QWs grown on Si

In this chapter, we will present power-dependent PL measurements, giving the possibility to rigorously compare sample efficiencies. As a cross-verification, we will also present TRPL results.

3.1 Power-dependent photoluminescence

In the first chapter, we presented in Section 1.4 the ABC model, a way to estimate the relative impact of different processes on the light emission efficiency of a semiconductor. Two of these processes are nonradiative, but happen predominantly at low (SRH processes) and high (A-M recombinations) active region carrier densities. Hence, there exists a region in-between high- and low-carrier density where the predominant process is radiative recombination, yielding maximal light emission efficiency. To analyse the emission efficiency of a given QW sample, it is therefore needed to first find the carrier density associated to the maximum IQE. To this purpose, power-dependent measurements are needed. More specifically, the particular excitation irradiance at which the IQE peaks contains a key information regarding the sample's efficiency, allowing sample-to-sample comparison.

3.1.1 Setup description

The setup used for the power-dependent continuous-wave (CW) PL is shown in Fig. 3.1. In this setup, lasers with emission wavelengths of 375 nm and 405 nm are routinely used. To measure the power during the series, the ratio of the transmitted light through a beam-splitter to the incident light on the sample was measured (see table 3.1). To access the excitation irradiance Π_{exc} on the samples, we first estimate the focused laser spot diameter, $\Phi = 2W_0$ (where W_0 is the beam waist radius), which is given by:

$$\Phi = \frac{4\lambda_{\text{exc}} f_{\text{obj}} M^2}{\pi D} \quad (3.1)$$

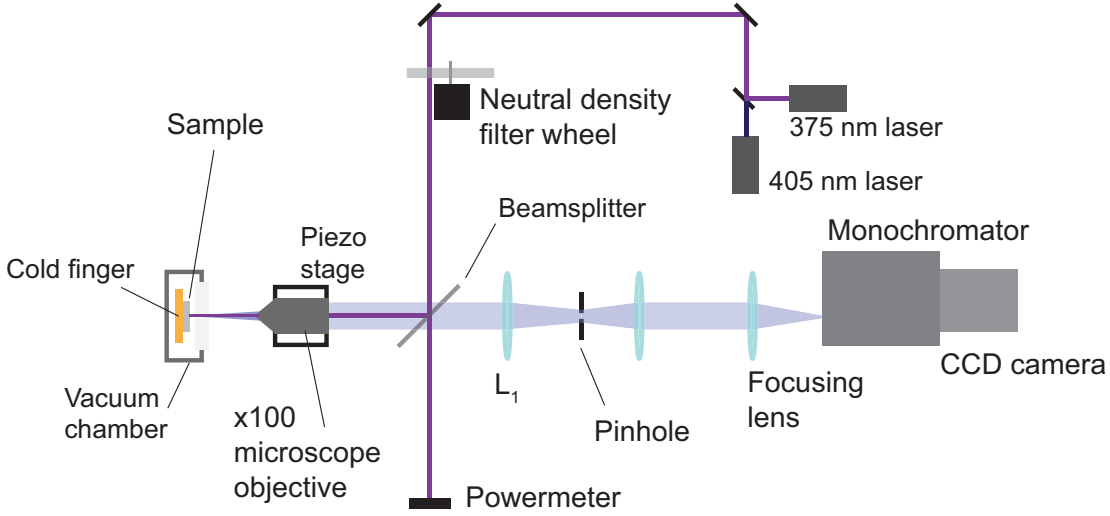


Figure 3.1: The setup used for power-dependent CW PL measurements is shown schematically; the sample, potentially in a cryostat, is excited by lasers emitting at $\lambda_{\text{exc}} = 375 \text{ nm}$ or $\lambda_{\text{exc}} = 405 \text{ nm}$. The microscope objective used to focus the laser also collects the luminescence. The spatial filtering consists in an afocal doublet whose shared focal plane contains a $d = 50 \mu\text{m}$ pinhole. A final lens directs the PL signal into a spectrometer for spectral analysis.

Table 3.1: Laser transmission

Laser wavelength λ_{exc}	Transmission ratio
375 nm	0.125
405 nm	0.19

where $\lambda_{\text{exc}} = 375 \text{ nm}$, respectively 405 nm , is the laser wavelength, $f_{\text{obj}} = 2.0 \text{ mm}$ is the focal length of our near-UV $\times 100$ Mitutoyo microscope objective of numerical aperture $NA = 0.5$, $M^2 = 1.12$ (respectively 1.1) is the beam quality factor, and $D = 1.2 \text{ mm}$ (respectively 0.8 mm) is the diameter of the collimated laser beam at the entrance of the microscope objective, [108] yielding $\Phi_{375} \approx 0.9 \mu\text{m}$ and $\Phi_{405} \approx 1.4 \mu\text{m}$. From these findings, one can also have an idea of the depth of focus (DOF) defined as two times the Rayleigh range z_0 :

$$DOF = 2z_0 = \frac{2\pi W_0^2}{M^2 \lambda_{\text{exc}}} \quad (3.2)$$

giving $DOF_{375} = 3.0 \mu\text{m}$ and $DOF_{405} = 7.1 \mu\text{m}$. We reproduce a scheme of a focused gaussian beam in Figure 3.2. The above-calculated values for the DOF suggest to make sure that the sample is in the focal plane of the objective before starting a power series. This was made possible by mounting the objective on a piezo-stage. Controlling the position of the latter through a panel included in the LabView control of the setup allows to reach a good precision. A loop recording the PL intensity at each piezo-stage position allows to optimally position the objective. Such an auto-focus curve is shown in Figure 3.3. Under the strong hypothesis of a

3.1 Power-dependent photoluminescence

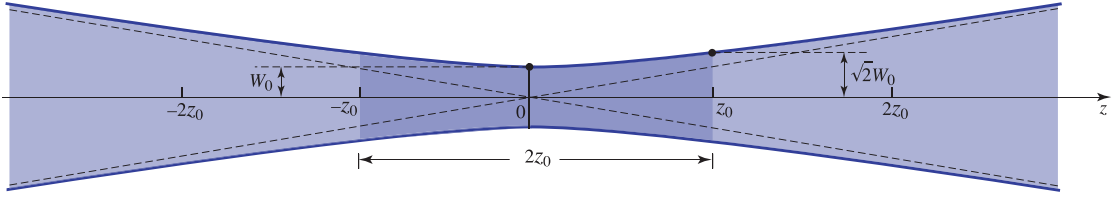


Figure 3.2: A focused gaussian beam: the waist W_0 is where the beam is thinnest, and the DOF of length $2z_0$ corresponds to the darker area. Adapted from Saleh and Teich [108].

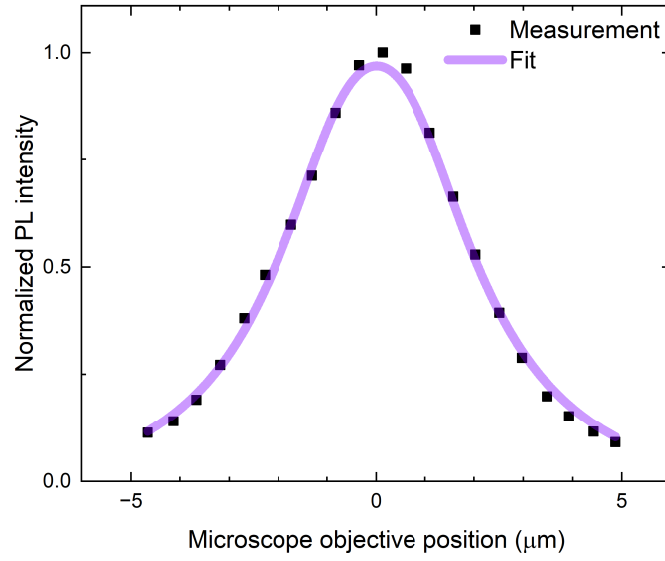


Figure 3.3: Autofocus curve: PL intensity as a function of the position of the piezo-stage supporting the microscope objective in front of the sample. The laser excitation wavelength is 375 nm.

linear response from the sample, it is possible to fit this data with a Gaussian beam model. We know that the power of the laser within a circle of radius ρ_0 (the system pupil) transversally to the propagation axis z is

$$\int_0^{\rho_0} I(\rho, z) 2\pi\rho d\rho = P_0 \left[1 - \exp\left(-\frac{2\rho_0^2}{W^2(z)}\right) \right] \quad (3.3)$$

with P_0 the total power and the beam width

$$W(z) = W_0 \sqrt{1 + \left(\frac{z}{z_0}\right)^2} \quad (3.4)$$

The relevant fitting parameters are reported in table 3.2. These values are in very good agreement to the calculated beam waist radius and DOF. From a practical point of view, the PL excitation spot size ($\sim 1\mu\text{m}$) allows to be barely sensitive to the sub-micron surface morphology fluctuations of the samples as a large number of V-pits is averaged (see Sec. 1.1.1).

Table 3.2: Auto-focus fitting parameters

W_0	4.3 μm
z_0	1.3 μm
ρ_0	0.47 μm
R^2	0.995

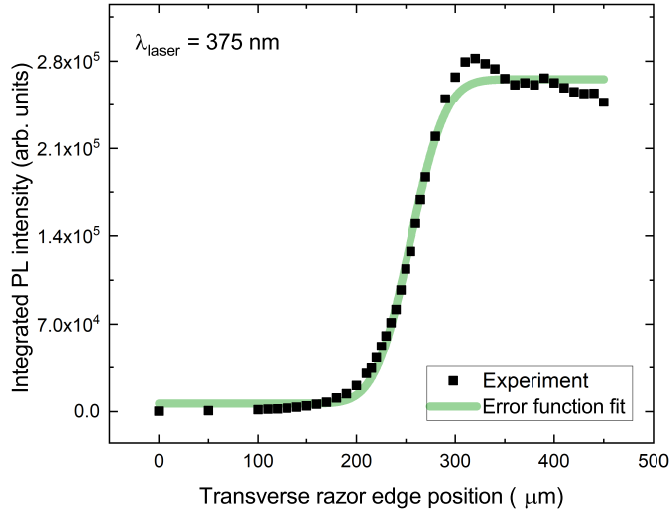


Figure 3.4: PL profile measurements: PL intensity as a function of the position of a razor-edge cutting the PL spot imaged at the focal plane after the lens L_1 (cf Fig. 3.1). The laser excitation wavelength is 375 nm. The green curve is an error function fit giving a PL waist radius of 56 μm .

Note that if the auto-focus is to be made once before a power series, it is more precise at medium to low excitation irradiances since the system is then more selective to the central part of the excited spot.

Let us now turn toward the system pupil. Without any further components than the objective and the lenses for light collection, the field of view of the sample is solely limited by the monochromator slit (set to 5 mm for the present measurements), *i.e.* $\sim 70 \mu\text{m}$. This would mean that the PL signal is collected from areas of the sample subject to very different laser excitation irradiances Π_{exc} hence from a QW zone experiencing a considerable radial carrier density gradient. To counteract this, we place a pinhole in the first image plane after the objective, small enough to be the pupil of the whole system and to select light emitted from a sufficiently homogeneously irradiated part of the sample. Therefore, it is needed to precisely know the size of the PL spot image in the above-mentioned plane, after the $f_1 = 180 \text{ mm}$ lens L_1 following the objective (cf Fig. 3.1). Profile measurements described in Purvis *et al.* [109] are reported in Figure 3.4. In first approximation, the transverse variation of the PL intensity follows the excitation density, which is Gaussian. Hence, the transverse cropping of the PL

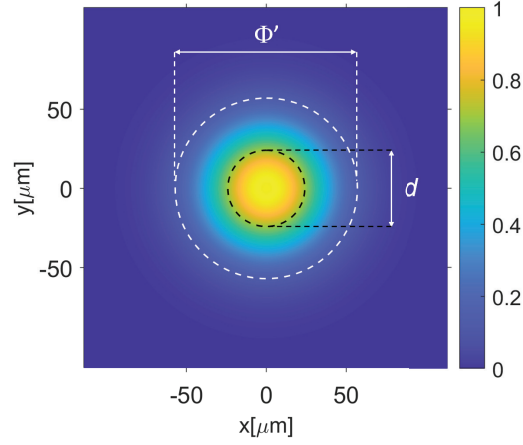


Figure 3.5: Simulated spatial distribution of I_{PL} in the plane of the pinhole.

image by a razor edge would be as follows:

$$\int_{-\text{inf}}^{+\text{inf}} \int_d^{+\text{inf}} I(x, y) dx dy \propto \frac{1 - \text{erf}\left(\sqrt{2} \frac{d}{W_0'}\right)}{\sqrt{2}/W_0'} \quad (3.5)$$

From these measurements, we deduce a diameter of $\Phi' = 2W_0' \sim 112 \mu\text{m}$ for the image of the PL spot at the lens focal plane. Then, we calculated the pinhole diameter allowing a compromise between a proper cropping of the most homogeneous part of the excitation irradiance and enough signal transmitted to the monochromator. This compromise was found by selecting the sample area subject to excitation intensities of at least 70% of the maximum intensity (see the intensity profile shown in Fig. 3.5). Therefore, the chosen spatial filtering configuration on the collection line consists of a lens L_1 with a focal length of $f_1 = 180 \text{ mm}$ and a pinhole with a diameter of $d = 50 \mu\text{m}$ placed at the lens focal plane. Such a configuration enables a light transmission of 30%.

3.1.2 Measurement challenges for sample comparison

It can be challenging to have an idea of the emission efficiency from thin epilayer samples exhibiting critically wavelength-dependent extraction efficiencies such as described in Section 1.5. This is inherent to different light extraction efficiency η_{extr} from one sample to another.

The first challenge appears during a single power-dependent PL series and originates from the QCSE. Indeed, since the carrier density changes over the power series, the electric field carriers experience in the QW varies. This causes a change of the PL emission energy $\Delta E_{PL} \sim 150 - 180 \text{ meV}$ for the 2.6 nm-thick QWs under study. The second challenge is that the samples, due to the growth reactor geometry, exhibit a radial dependence of the epilayer film thickness. Estimated to about 5% in Section 1.5, such a thickness variation can lead to an extraction maximum changing into a minimum within a displacement over the 1 inch sample radius.

Chapter 3. Impact of the underlayer on InGaN QWs grown on Si

Hopefully, the second challenge can be useful to measure a representative power-series of a given sample. For the sake of a better understanding, we need to have a deeper comprehension of the power-dependent PL measurements.

Performing PL measurements as a function of excitation irradiance (Π_{exc}) is a way to monitor the QW emission efficiency. Scanning at least three orders of magnitude of Π_{exc} is the only way to find the peak emission efficiency. At each excitation irradiance, a PL spectrum is recorded and integrated over a given spectral range positioned relatively to the emission maximum E_{PL} . This I_{PL} value is then divided by Π_{exc} , giving thereby the relative efficiency $I_{\text{PL}}/\Pi_{\text{exc}}$. For each dataset, there exists an irradiance value at which $I_{\text{PL}}/\Pi_{\text{exc}}$ reaches its maximum. We call this particular value Π_{max} : such excitation creates the carrier density yielding the maximum of IQE. The maximum can be understood by recalling the ABC model described in Section 1.1.2. At a too high carrier density, A-M processes take place, degrading the emission efficiency. Upon reducing Π_{exc} , such three-body processes are less prone to happen and two-body processes of spontaneous emission are dominating around Π_{max} . Further reduction of Π_{exc} toward very low values of the carrier density leaves mainly SRH nonradiative recombination, deleterious for the IQE. Hence, these power-dependent measurements provide a precious insight into the QW efficiency. Moreover, the power-dependent measurements allow to compare samples with very different extraction efficiencies: the lower Π_{max} , the higher the IQE.[17]

Now we understand that a power-dependent curve of a sample experiencing interference might be complicated as the QW emission energy E_{PL} can blueshift sufficiently to not coincide anymore with an extraction maximum. Consequently, the efficiency curve would be dramatically distorted. This is where the second challenge of a radial-dependent sample thickness comes into play. We choose a measurement position such that the peak emission energy variation due to carrier density changes remains within a maximum of light extraction. Such a way of choosing the right measurement position is represented in Figure 3.6. We see that double-peaked spectra, convolution of the PL emission by a destructive extraction interference, are only present when the blueshift is maximal, at Π_{exc} far from Π_{max} . The experimental points at the highest excitation irradiances are *de facto* dubious, but confirm that the other ones can be trusted.

3.1.3 Temperature dependence of the power-dependent measurements

To have a broader picture, let us consider how these measurements evolve with temperature. To do so, the samples were mounted in an open circuit liquid He cryostat (*cf* Fig. 3.1). This instrument works by injecting a liquid He flow around the main part of a copper caloduc. That copper cold finger enters a vacuum chamber to support the sample and cool it by thermal conduction. An automated controller warms the finger when higher than cryogenic temperatures are needed. Since there is a flow in the cryostat, there can be vibrations of the system as soon as the flow is turbulent. These movements can cause the sample surface to oscillate around the focus plane of the microscope objective. Therefore, care must be taken to

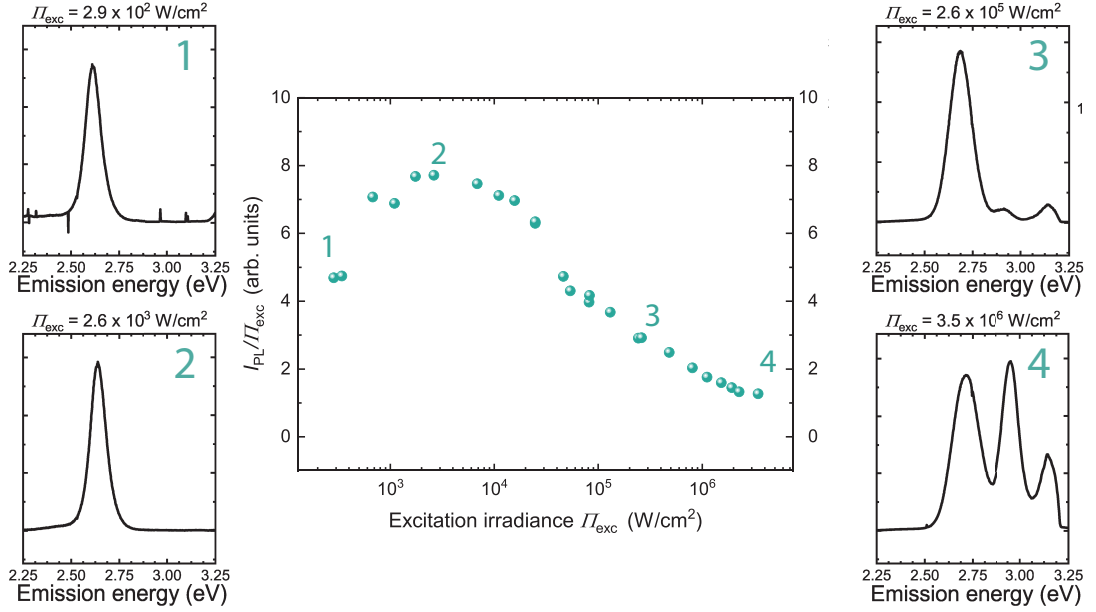


Figure 3.6: Power-dependent PL measurements at room-temperature for sample U. The top insets represent the PL spectra corresponding to selected excitation irradiances.

keep a liquid He flow high enough to stay in the laminar state.

Once the first autofocus was made, proper interference patterns were found, the temperature was stable, power series were taken. PL measurements as a function of Π_{exc} from cryogenic (8 K) to room-temperature are shown in Figure 3.7.

3.2 Results and discussion

3.2.1 Semi-quantitative considerations

Comparing the key characteristics of samples R (without UL) and U (with UL) at $T = 8\text{ K}$ reveals that both samples exhibit Π_{max} spreading over a plateau centered at an irradiance near $1 \times 10^3 \text{ Wcm}^{-2}$, which attests to a relatively high IQE as expected at low temperature (*cf* Fig. 3.7).[110] Interestingly, the raw PL intensities are roughly 40% lower for sample R, which can already be a sign of a higher density of PDs. Indeed, it has been observed that such defects can have an impact even at cryogenic temperatures.[102] When the temperature is raised to $T = 290\text{ K}$, Π_{max} for sample U slightly increases to $3 \times 10^3 \text{ Wcm}^{-2}$, whereas Π_{max} for sample R increases by a much larger amount, *e.g.* by two orders of magnitude (up to $3 \times 10^5 \text{ Wcm}^{-2}$), indicating a strong decrease of IQE with temperature.[17] In addition, the emission efficiency value at Π_{max} decreases for both R and U. Nonetheless, the decrease of the peak IQE is more pronounced for sample R, since from low- to room-temperature, the relative peak efficiency is reduced by a factor of ~ 12 for sample R, *versus* only ~ 4.6 for sample U.

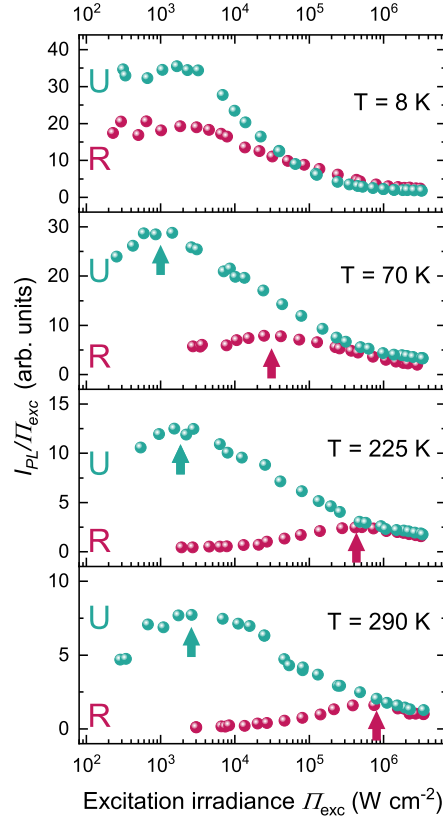


Figure 3.7: I_{PL}/Π_{exc} as a function of Π_{exc} for $T = 8, 70, 225,$ and 290 K for samples R and U. The arrows indicate Π_{max} .

From these measurements, we see that on the low-irradiance side, sample R experiences a lot more SRH nonradiative recombinations.[55] These recombinations, happening instead of radiative ones, cause sample R to have a worse IQE than U. As explained in Section 1.7, TDs can be screened by V-pits.[92, 93] Therefore, the smaller V-pits observed on sample R could lead to a reduced screening and explain the lower IQE of this sample (see Fig. 3.8(d) *versus* (e)). To verify this hypothesis, we grew a control sample with similar PD density as R and similar V-pit size as U (40 nm) (see Fig. 3.8(f)). This was achieved by growing a thin GaN interlayer at low-temperature underneath the QW active region (*cf* Fig. 3.8(c)). Indeed, growth of GaN at low-temperatures is known to promote the formation of V-pits.[99] The room-temperature efficiency curve of this sample V is shown in Figure 3.8(i). We can see a similar Π_{max} value for samples R and V, indicating that their IQE is comparable. This demonstrates that the difference between R and U is not ascribed to a change in the V-pit size, but to the presence of an UL.

The reduction of the IQE can then be attributed to the presence of PDs in the InGaN/GaN QW directly grown on the GaN buffer layer without an UL.[15, 16] We conclude that the introduction of an UL leads to a much higher efficiency. In turn, the high density of TDs ($N_{TD} > 10^{10} \text{ cm}^{-2}$) gives a rather surprising tone to the decisive role played by the introduction

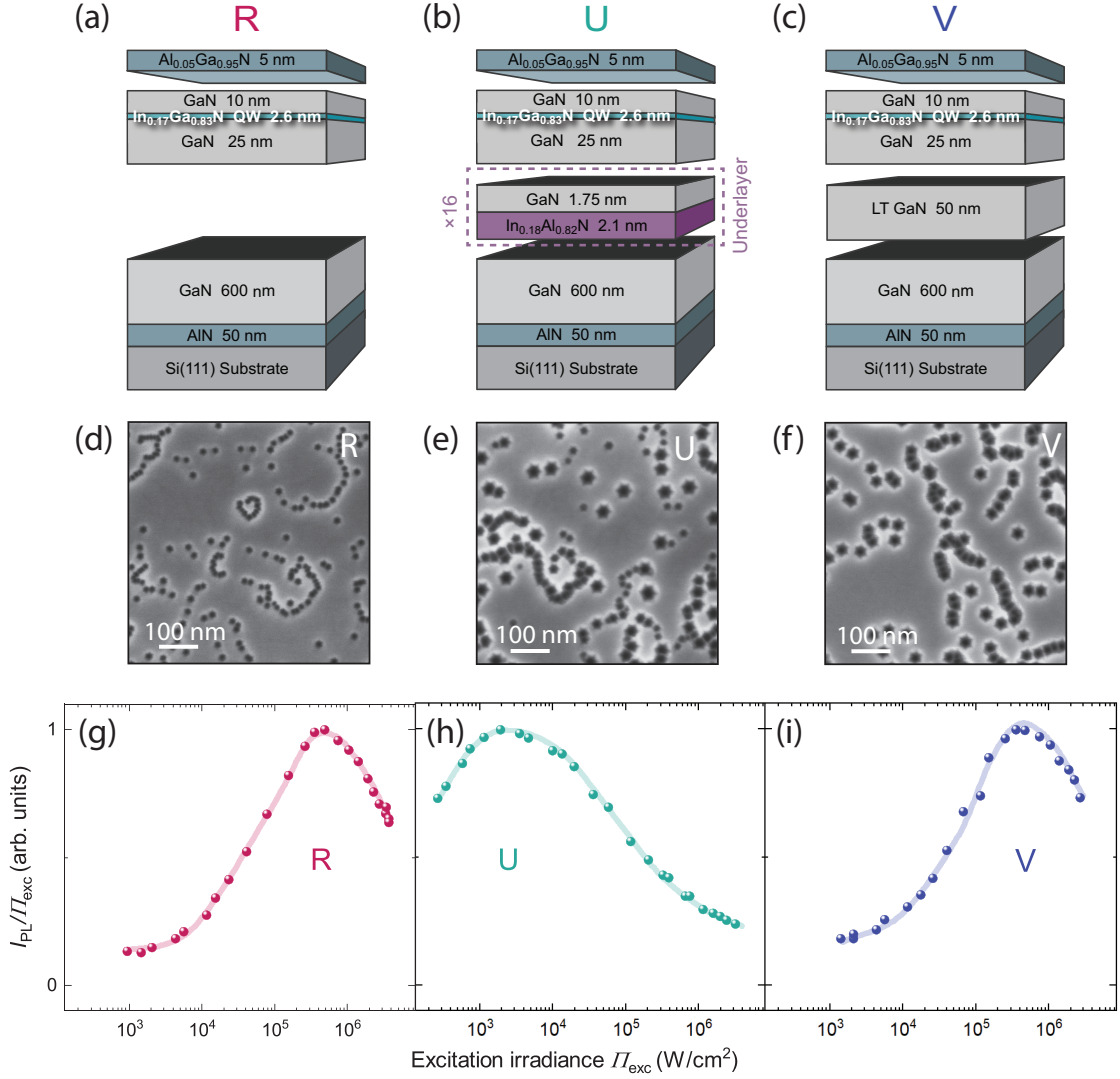


Figure 3.8: Sample structure of reference sample R (a), SL-UL sample U (b) and control sample V (c). SEM images of the three samples. Normalised $I_{\text{PL}}/I_{\text{exc}}$ as a function of I_{exc} for samples R (g), U (h) and V (i) at room-temperature.

of an In-containing UL in enhancing the efficiency of these samples. This tends to indicate the prominent role played by PDs over dislocations at room-temperature. Indeed, the elimination of PDs in sample U allows to maintain a high efficiency up to room-temperature.

Now, let us investigate why the peak efficiency in sample R shifts toward higher irradiances when the temperature is increased. Such a behaviour indicates a thermal activation of NRCs. This is expected for SRH recombination since their relaxation process involves phonons, as explained in the Section 1.4 describing the ABC model. However, this temperature-dependence is enhanced in QWs due to localisation effects. This can be explained by the fact that while the carriers are localised in the potential landscape minima of the QW, their diffusion toward PDs is hindered. When the temperature reaches a given value ($T \sim 50\text{--}70$ K) (see Sec. 2.3.3),

Table 3.3: B_0 and C_0 values from Haller [33].

B_0	$8.6 \times 10^{-11} \text{ cm}^3 \text{ s}^{-1}$
C_0	$1.6 \times 10^{-29} \text{ cm}^6 \text{ s}^{-1}$

carriers start to be delocalised and can diffuse toward NRCs, namely PDs.

3.2.2 Quantitative ABC modelling

For a deeper understanding of the temperature-dependent power-series, we tried to reproduce the data using a comprehensive ABC model described in Section 1.4. Our model takes into account the variation of the B coefficient with temperature and carrier density, as well as the inter-coupling of A , B and C , and the defect-assisted A-M processes, as proposed by David *et al.* [17]. To do so, we first need to consider a carrier injection factor: for a given CW laser excitation irradiance Π_{exc} , a carrier density $\gamma_{\text{conv}} \times \Pi_{\text{exc}}$ is generated in the QW. At first, from the room-temperature Π_{max} in sample R, we can suppose $\gamma_{\text{conv}} \sim 10^{14} \text{ W}^{-1} \text{ cm}^{-1}$ to meet previous results with high SRH recombination occurrence as reported in Haller [33]. In the same reference, ABC modelling values for similar QWs with lower In contents are reported in Table 3.3. With such starting point, we can apply the ABC model to the present data. The modelling accounts well the data from 300 K down to 80–100 K. However, it fails to reproduce the power-dependence of the relative-efficiency at lower temperatures.

This can be understood by considering that localisation phenomena were neglected in the present model. As explained in Section 1.3, the 2-dimensional energy landscape of InGaN QWs is not flat, but rather contains ~ 3 nm-typical sized variations.[46] As a consequence, the effect of localisation should be considered. We estimate these close-packed localisation centers to be present in the QWs at a density of roughly $\frac{1}{3 \times 3} \text{ nm}^{-2}$, yielding a 2D-density of $\sim 1 \times 10^{13} \text{ cm}^{-2}$ and a 3D-density of $N_{\text{loc}} \sim 4 \times 10^{19} \text{ cm}^{-3}$.

As seen in Section 2.3.3, localisation happens below $T = 70 - 80$ K. Below such temperatures, carriers will stay in potential minima. Conversely, carriers injected in the QW experience a juxtaposition of 0-dimensional centers instead of a planar energy landscape. The consequence is a dramatic increase of the local effective carrier density for the same laser excitation irradiance. To account for this physical phenomenon, we developed a model accounting for the variation of the excitation irradiance to effective carrier density conversion factor γ_{conv} . Hence, the temperature plays a role in activating localised carriers into free carriers. In our model, we also consider the variation of the ABC coefficients with carrier density, as proposed by David *et al.* [17]. The variation of B with carrier density was explained in Section 1.4. In the present situation, the Coulomb enhancement (the increase of B at low carrier densities) does not have a significant impact. At lower temperatures, two phenomena happen: the SRH recombinations are thermodynamically hindered and in the localisation centers there is a higher effective carrier density. Consequently, this high carrier density impedes the Coulomb enhancement of

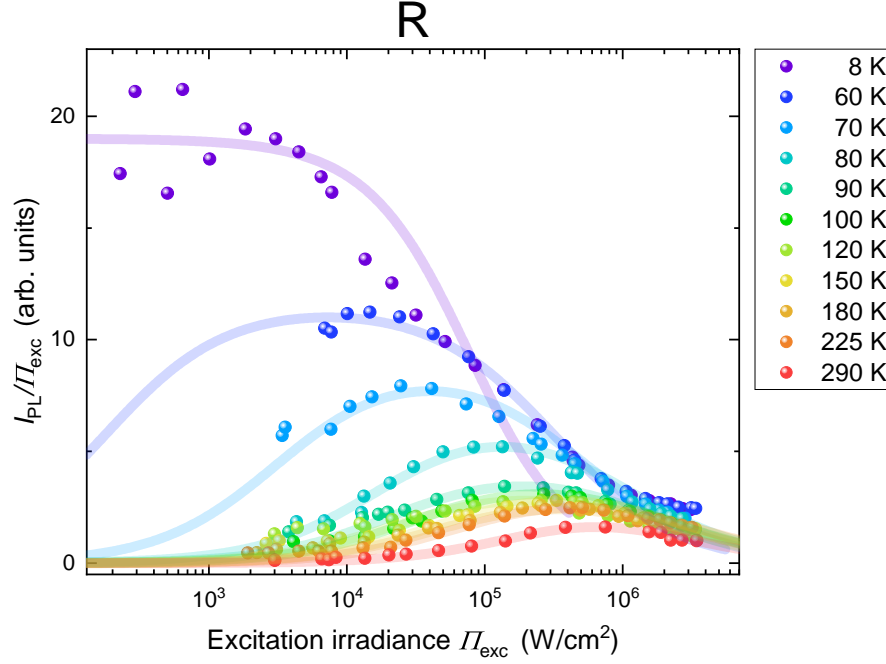


Figure 3.9: Power-dependent PL series for sample R taken at different temperatures from room-temperature down to $T = 8$ K. The colored curves are comprehensive ABC models where the only parameters are γ_{conv} and A , since (i) $B(T)$ was experimentally determined from the S-shape of $E_{\text{PL}}(T)$ shown in Figure 2.12 and (ii) $C(T)$ is linked to $A(T)$.

B . As the temperature increases, the SRH processes become more pronounced, reaching a point where Coulomb enhancement can not compensate the lower efficiency at low carrier densities. Our model is robust regarding this effect since we consider a heuristic increase in γ_{conv} : Coulomb enhancement would be seen below $\sim 2 \times 10^{17} \text{ cm}^{-3}$ which corresponds to $2 \times 10^2 \text{ W cm}^{-2}$ at low temperatures, and $2 \times 10^3 \text{ W cm}^{-2}$ at high temperatures. For both cases, the recorded data is above the Coulomb enhancement regime. This is why in the following we did not take into account this effect. From the variation of B , we deduce A and C coefficients according to $A \propto B^{0.9}$ and $C \propto B^{1.2}$. [17] Practically, we used the B temperature variations deduced from the measurements of Section 2.3.3, shown in Figure 2.13. We set C_0 to the value found by Haller [33]. In the ABC model, we included the defect-assisted A-M dependence, calculated as

$$C(T) + kA(T) \quad (3.6)$$

where k is an empirical coupling factor to account for defect-assisted A-M processes, thermally activated. We are now left with two fitting parameters, γ_{conv} and A . This modelling, shown in Figure 3.9, is able to reproduce the data behaviour down to 8 K. We report the temperature variation of γ_{conv} and A in Figure 3.10.

γ_{conv} remains at a cryogenic value of $\gamma_{\text{conv,loc}} = 1.3 \times 10^{16} \text{ W}^{-1} \text{ cm}^{-1}$ up to a delocalisation temperature of $T_{\text{del, i}} \sim 62$ K. From $T_{\text{del, i}}$, the decrease of γ_{conv} due to the delocalisation of the

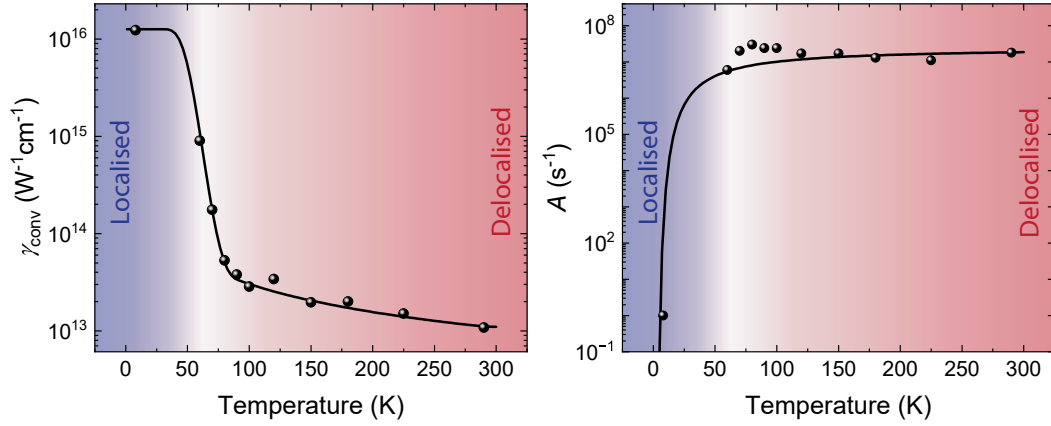


Figure 3.10: Temperature impact on (a) γ_{conv} and (b) A . Cryogenic $\gamma_{\text{conv,loc}} = 1.3 \times 10^{16} \text{ W}^{-1} \text{ cm}^{-1}$ holds until $T_{\text{del, i}} \sim 62 \text{ K}$. Above, the reduction of γ_{conv} indicates that injected carriers are no more restrained to 0D-structures associated to the localisation centers. The A coefficient increase with temperature can be modeled by an Arrhenius law, physically associated to the activation energy of SRH NRCs $E_a = 7.9 \text{ meV}$. An anomalous dip in A at 62–72 K, consistent with previous studies, suggests a complex interplay between carrier localisation and temperature.

carriers can be understood as a promotion of carriers trapped in the localisation minima.

The temperature dependence of the A coefficient follows *generally* an Arrhenius law, if we consider SRH NRCs of activation energy E_a :

$$A(T) = A_{300} \cdot \exp\left(-\frac{E_a}{k_B \cdot T}\right) \quad (3.7)$$

where $A_{300} = 2.5 \times 10^7 \text{ s}^{-1}$ and $E_a = 7.9 \text{ meV}$. The point at 8 K is assumed to present almost no nonradiative recombinations. To our knowledge, this way to access E_a has seldom been reported before. In detail, upon thermal activation of SRH recombinations — *i.e.* from 62–72 K to $\sim 100 \text{ K}$ — we observe the same A -value decrease with increasing T as observed in David *et al.* [111]. This phenomenon is not well explained, but observed in samples with very different defect densities and across different materials.[60] We tentatively propose a mechanism explaining this non-homogeneous behaviour upon decreasing the temperature:

1. From room-temperature, SRH processes first decrease following a basic Arrhenius law.
2. Below a given temperature (around 100 K), carriers start to be localised in potential minima of the QW. This enhances the interaction of carriers and NRCs, hence increasing A with decreasing T .
3. When further decreasing the temperature below the delocalisation temperature, carriers are trapped in local minima, and rely heavily on temperature to initiate their movement toward NRCs: the A coefficient decreases again with the temperature following an Arrhenius law.

3.3 Time-resolved photoluminescence

Now that we have analysed the QWs through steady-state PL experiments, we turned toward TRPL. Such measurements allow to probe the transient nature of the recombination processes.¹

To excite the samples, a pulsed laser generates $\sim 1 \mu\text{W}$ pulses at a repetition rate of 500 kHz and at a wavelength of 375 nm. Its $\sim 3 \mu\text{m}$ beam diameter allows for averaging sample local morphology fluctuations. A parabolic mirror is used to collect the resulting luminescence, and a Horiba iHR550 spectrometer with a 600 grooves/mm grating is used for analysis. The temporal resolution in this setup is estimated to be < 50 ps. The TRPL decay profiles for the two samples R and U were recorded at various temperatures and are shown in Figure 3.11. By

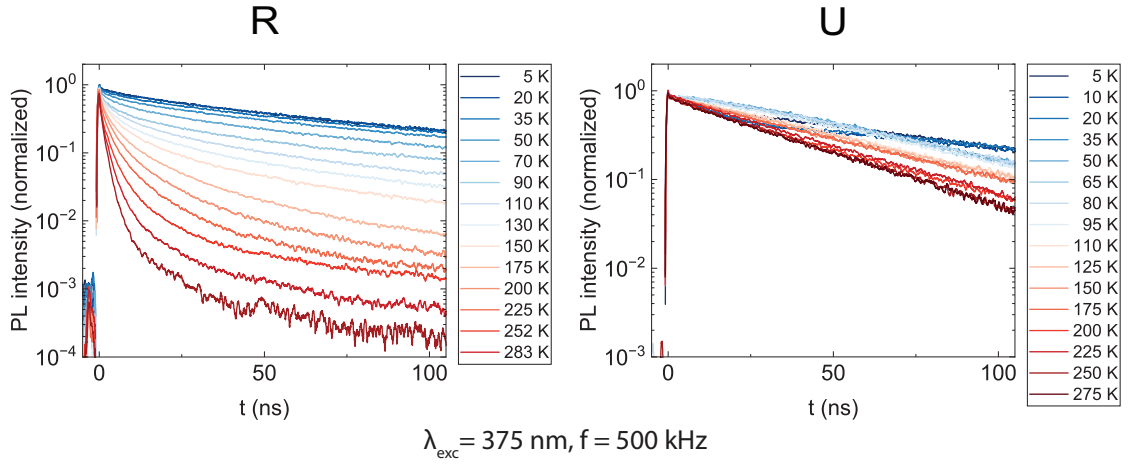


Figure 3.11: I_{PL} as a function of time for samples R and U at temperatures $T = 5 - 290$ K.

fitting the early decay time of each curve using a monoexponential fit, the effective carrier lifetimes τ_{eff} are extracted. Their dependence on temperature (5–290 K) is reported in Figure 3.12.

We define τ_{NR} and τ_{R} the carrier nonradiative and radiative lifetimes, respectively. From this, we can write their respective contribution to the effective carrier lifetime:

$$\frac{1}{\tau_{\text{eff}}} = \frac{1}{\tau_{\text{NR}}} + \frac{1}{\tau_{\text{R}}} \quad (3.8)$$

From Figure 3.12, we see that for sample R, τ_{eff} decreases from 54 ns at 20 K to 2 ns at 290 K. On the other hand, for sample U, τ_{eff} slightly declines from 75 ns at 20 K to 34 ns at 290 K. Making the hypothesis that at low temperature, nonradiative recombinations are negligible — which is not the case, but allows to define a figure of merit — translates into:

$$\tau_{\text{NR}}(\text{low } T) \gg \tau_{\text{R}}(\text{low } T) \implies \tau_{\text{eff}}(\text{low } T) \lesssim \tau_{\text{R}}(\text{low } T) \quad (3.9)$$

¹These measurements have been performed by Dr. G. Jacopin at Institut Néel, CNRS.

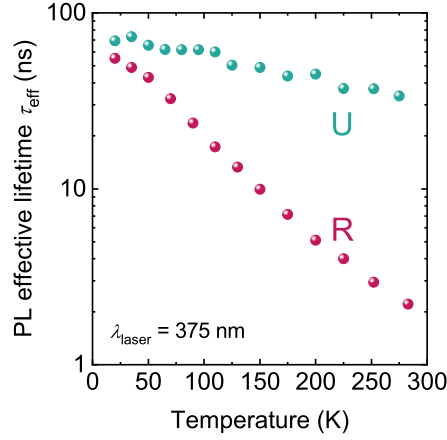


Figure 3.12: Effective lifetimes as a function of temperature for samples R and U.

which gives:

$$IQE = \frac{\tau_{NR}}{\tau_{NR} + \tau_R} \lesssim \frac{\tau_{eff}(\text{high } T)}{\tau_{eff}(\text{low } T)} \quad (3.10)$$

From the TRPL measurements, we deduced $IQE(R) \approx 4\%$ and $IQE(U) \approx 49\%$.

The TRPL measurements hence confirm that sample R suffers from much more nonradiative recombinations than sample U. Note that here, we neglect nonradiative processes at low temperature, which is a strong hypothesis. This overestimates the actual IQE value. It is especially true for sample R for which the amount of NRCs is significant.

From these macroscopic lifetime measurements, we can estimate the diffusion lengths in each sample. In the literature, D values for comparable $In_xGa_{1-x}N$ QWs at room-temperature range from $0.27 \text{ cm}^2 \text{ s}^{-1}$ ($x = 0.23$) [112] to $6 \text{ cm}^2 \text{ s}^{-1}$ ($x = 0.13$) [52], tending toward zero at low temperature. These values would yield $L_D > 1.9 \mu\text{m}$ and $L_D > 0.5 \mu\text{m}$ for samples U and R at room-temperature. Such large diffusion lengths have been recently reported in high-quality InGaN/GaN QWs grown on GaN substrates.[17, 53]

Another worth-mentioning point is that the decay times do exhibit a non-monoexponential nature, especially for sample R (*cf* Fig. 3.11). This was formerly partly explained by the presence of defect-assisted Auger processes at very high fluences.[75] In our case, it is also possible that distinct morphological QW regions were probed under the same laser excitation spot, which would explain this unexpected behaviour. Inhomogeneities were observed in the previous chapter (see Sec. 1.1.1). The current queries reveal the need for further microscopic investigation.

Summary

We have precisely described the setup used for power-dependent PL measurements and pointed out the subtleties when dealing with samples where microcavity effects are pro-

nounced. Armed with confidence about the relevance of the results, we draw the conclusion that adding an underlayer reduces the SRH nonradiative recombinations. From the temperature-dependence of the power-series, we confirm that these phenomena are thermally activated, although a portion of the nonradiative recombination centers remain active at low-temperature. This demonstrates that the ratio between high- and low-temperature PL intensities is not a reliable way to assess sample IQEs.

Our measurements also indicate that although the TD density is in the 10^{10} cm^{-2} range, the mitigation of PDs by means of an In-containing UL increases drastically the efficiency of the QWs. Conversely, the huge impact of the UL despite such a high TD density could point toward a rather low activity of TDs. This finding needs to be further investigated.

TRPL measurements confirm the power-dependent experiments. In addition, from the decay-curves, it was seen that simple exponential fits were not perfectly accurate. This was ascribed to the spatial scale of the measurement spot.

To construct a complete understanding of the optical properties of the QWs under study, we need to probe the carrier dynamics at a smaller scale. To this purpose, the next chapter will present CL mappings with nanometer scale resolution.

4 Nanoscale optical properties of InGaN quantum wells

In the previous Chapter 3, the measurements were done on areas too large to get insight into the impact of the surface morphology fluctuations induced by TDs, as presented in Chapter 2. On the other hand, macroscale PL characterisations average the sample optical properties, but we miss the understanding of the 2-dimensional carrier dynamics in the QWs. As mentioned in the conclusion remarks of Chapter 2, the growth grains delimited by V-pits and step-bunching could have an impact on carriers in the QW. In this chapter, to further investigate this aspect, we will perform a nanoscale characterisation of the QWs. The chosen tool, yielding higher spatial resolution, is CL.

4.1 Cathodoluminescence

4.1.1 Experimental method

CL is an experimental materials analysis tool based on complex phenomena. Nonetheless, since we have described PL measurements, a simplified analogy consists in stating that instead of injecting carriers in the sample by means of a pump laser, we use an electron beam, very similar to the system presented in Figure 2.4. The tool we used for the steady-state measurements is an Attolight Rosa 4364, and the data presented in this chapter were mainly acquired under an acceleration voltage of 2 kV and a probe current of 300–500 pA, to maximise the resolution. For the CL lifetime measurements, these values were 3 kV and ~ 1 pA.

Electronic injection intricacies

In CL, the fact electrons are injected does involve a few more steps compared to the interband absorption triggered by quasi-resonant optical pumping used in PL. At each position of the electron beam, the following processes happen:

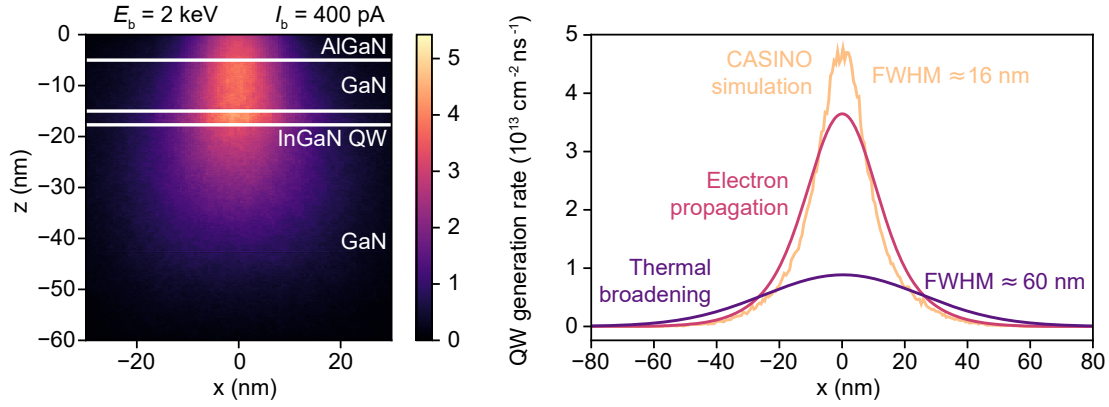


Figure 4.1: (a) Monte-Carlo simulation of the excitation volume. The simulated electron trajectories materialise the interaction space between accelerated electrons and III-N material. (b) G_{QW} radial profile ; the red and violet curves successively embed the electron transfer broadening and the thermal relaxation of the hot carriers.

i. Energy deposition

The electrons deposited by the beam are contained in an excitation volume. The diameter of this volume was estimated by Monte-Carlo simulations to be ~ 16 nm. The simulation output is reported in Figure 4.1. With beam energy, probe current, and sample design determined, the carrier generation rate in the QW during continuous CL is expressed. The number of carriers created by an incoming electron is given by the energy it deposits in the material divided by three times the material bandgap. The 3D generation rate is then given as

$$G(x, y, z) = \frac{I_p E_{\text{dep}}(x, y, z)}{q 3E_g(z)\Delta V} \quad (4.1)$$

where I_p is the probe current, E_{dep} is the deposited energy distribution, E_g is the bandgap, and ΔV is the volume element. The resulting distribution is integrated over the out-of-page direction for 2D visualisation, yielding G_{QW} expressed in units of $\text{cm}^{-2} \text{ns}^{-1}$. The probe diameter is estimated at approximately 20 nm, influencing the carrier generation rate profile throughout the sample.

ii. Electron beam scattering and relaxation

As electrons propagate in the material, their trajectories scatter laterally such that the interaction with the QW is broadened by approximately the travel distance, ~ 17 nm.¹ Additionally, the electrons are having a high kinetic energy, and being "hot carriers" they further relax over a mean distance of ~ 50 nm.[113] This effect is accounted by a gaussian profile convoluting the simulation and scattering results. The quadratic sum of these effects is another simplified

¹For this reason, positioning the QW close to the epilayer surface (15 nm below) allows to ensure a high CL resolution.

method to estimate the CL resolution limit, which in our case is:

$$\sqrt{16^2 + 50^2 + 17^2} = 55 \text{ nm} \quad (4.2)$$

This approximation is in line with the numerical modelling of Figure 4.1 providing a FWHM of 60 nm. If one neglects nonradiative recombinations in the vicinity of the injection region, the generated carriers quickly "fall" into the InGaN QW (the typical time of this process is a few ps).

iii. Carrier diffusion in the QW

While in the QW, carriers diffuse in a two-dimensional potential landscape over distances of a few tens of nanometers (low-temperature) to a few microns (room-temperature).[52] Of course, this depends on the IQE of the QW.

iv. Radiative recombination

The harvested CL light stems from carriers that did not encounter nonradiative centers on their path until they spontaneously recombine. Note that such recombinations leading to photon emissions can happen far from the e-beam dwell position and contribute to the CL signal.

For more information about the CL characterisation method, see Weatherley [35].

4.1.2 Cathodoluminescence mappings

Performing a CL mapping consists in dwelling the electron beam on one position of the sample, collecting photons, before moving to another position. By scanning the sample in this way, we construct a mapping of the sample optical properties over a few hundreds of nanometers to a few microns. Simultaneously, the system records the SE to construct the top-view of the probed area.

Intensity maps

Once the photons are emitted and collected, they are sorted by a spectrometer in the same way as during PL measurements. By integrating the spectra over the whole QW emission (*cf* Fig. 4.2(a)-(c)), we can extract the intensity maps represented in Figure 4.2.

Figure 4.2(d)-(f) displays the QW integrated intensity CL images of $3.2 \times 3.2 \mu\text{m}^2$ areas for samples R, U and V (individually normalised), recorded at cryogenic temperatures (10 K). Except for sample U, the maps show already areas of different CL intensities, with patches of typical size $0.5 \mu\text{m}$ in diameter. This phenomenon is accentuated when the temperature is

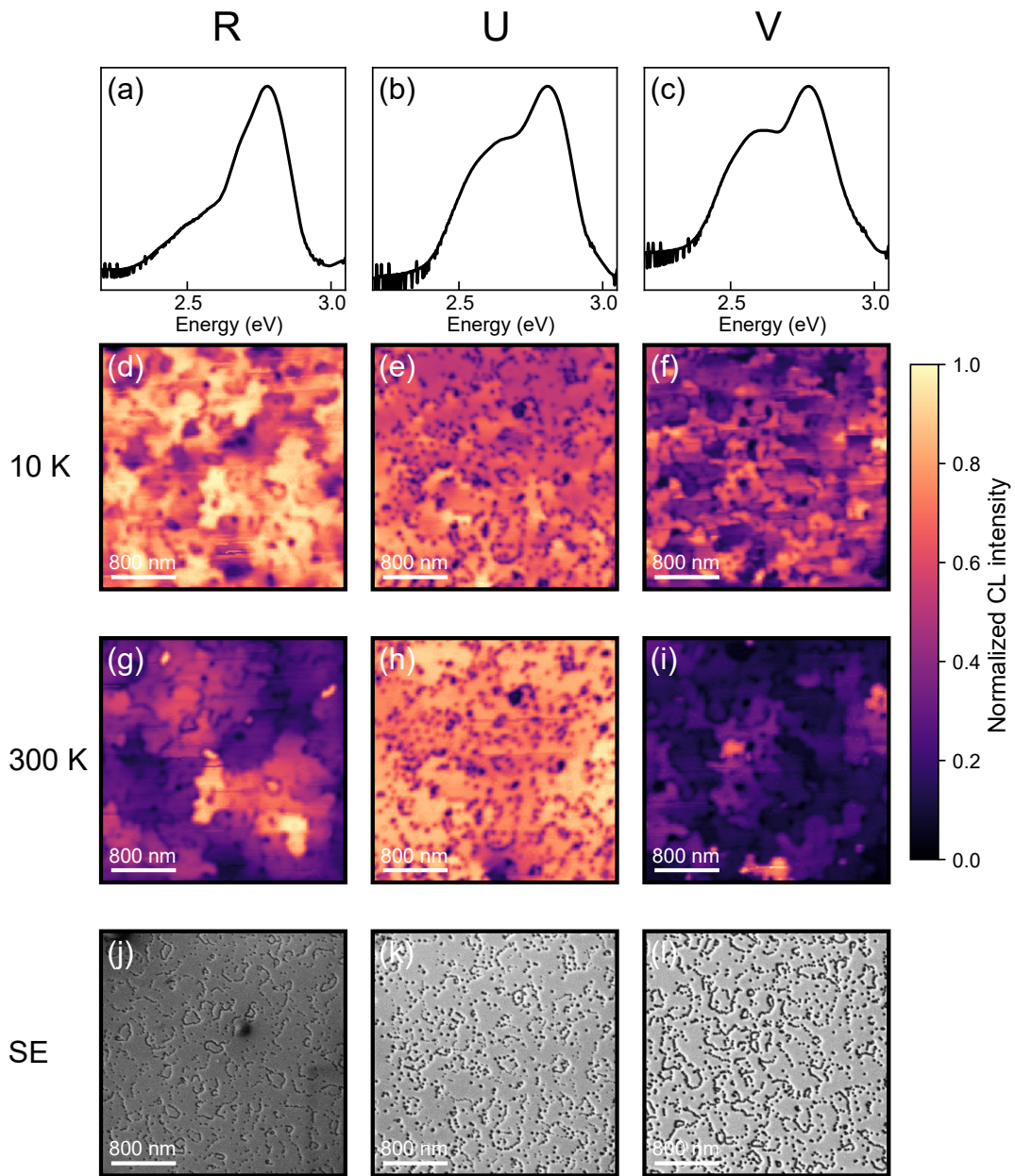


Figure 4.2: The top row represents the mean normalised CL spectra of samples R, U and V, respectively, obtained at 10 K. The abscissa limits coincide with the signal energy integration domain used for the maps represented below. The following two rows display the CL individually normalised QW integrated intensity images of $3.2 \times 3.2 \mu\text{m}^2$ areas for samples R, U and V, captured at both cryogenic and room-temperatures. Within these images, clusters of V-pits manifest as sizable dark spots. The lower row shows SE images representing corresponding areas for each sample, wherein the V-shaped pits, denoting the location of TDs, appear as dark spots.

raised to 300 K (*cf* Fig. 4.2(g)-(i)), and the prevalence of lower intensity areas (darker) increases

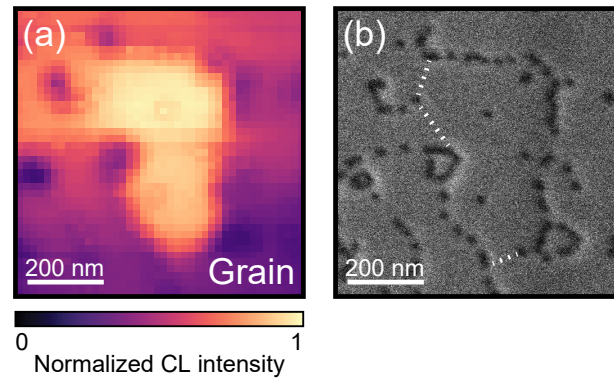


Figure 4.3: Zoom-in view of (a) the room-temperature CL map of sample R and (b) the corresponding SE image. A grain appears clearly in (a) while its boundaries are delimited by V-pits and likely step-bunching (dotted lines) as shown in (b).

— except for sample U. Macroscopically, this comes from samples R and V embedding more SRH centers in their QW, which are thermally activated. We remind that sample U features an UL which traps SDs while in samples R and V, these SDs are incorporated in the QW forming thereby PDs. Thus, the CL mappings are in line with the previous findings of Chapter 3.

Microscopically, the presence of dark spots in the CL maps is also striking. These are ascribed to V-pits, which is confirmed by the SE maps (*cf* Fig. 4.2(j)-(l)). By comparing the CL maps with the SE images, we find that there is a direct correlation between the CL intensity area surroundings and the SE dark spots materialising the V-pit arrays observed in Section 2.2.1. As concluded in Chapter 2, these TD curtains materialise growth grain boundaries. These grain boundaries translate in the vicinity of the QW as either V-pits or step-bunching, as shown in 2.2.3.

A striking aspect of these CL intensity areas is their size: from the TRPL measurements of Section 3.3, we inferred carrier diffusion lengths higher than the size of these areas. Therefore, in a QW without barriers to carrier diffusion, intensity variations on scales below the diffusion length would not appear. As an example, a grain such as depicted in Figure 4.3 has a size of $\sim 1/5$ the plausible $1\ \mu\text{m}$ -diffusion length. We conclude that carriers injected in a given domain corresponding to one growth grain do not diffuse to neighbouring areas. Interestingly, this remains true when the boundaries are not continuous V-pit arrays, as is the case of the top-left and bottom parts of the grain from Figure 4.3(a). This is ascribed to the presence of step-bunching yielding lower In content, as was discussed in Section 2.2.3. Such features present a higher energy, thereby forming barriers for the carriers. The bright grain exemplified in Figure 4.3(a) would thus correspond to an area with a low PD density. Moreover, from the local intensity fluctuations, we can conclude that the IQE is not uniform across the sample. These observations demonstrate that the optical properties of the QW are not homogeneous at a submicron scale.

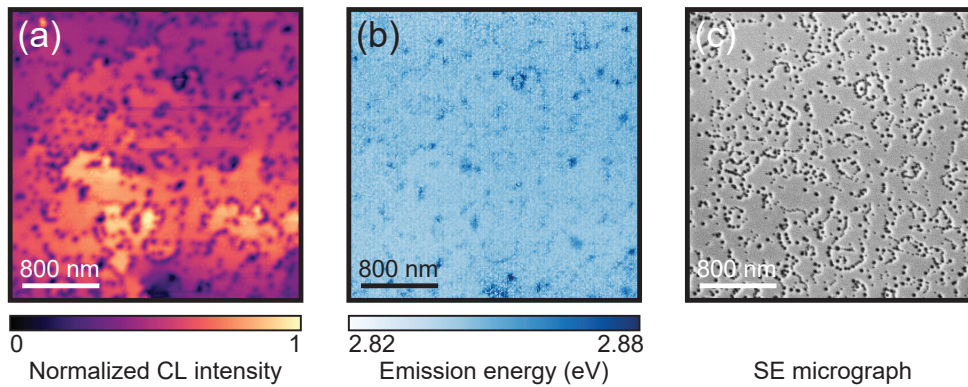


Figure 4.4: Energy maps revealing carrier confinement in sample U, measured at 300 K. (a) CL intensity map above 2.8 eV for sample U. Lower emission efficiency is observed along the domain boundaries, indicating nonradiative recombination centers concentrated between growth grains and potential broken QWs near V-pits. (b) Mean emission energy computed by integrating spectra above 2.8 eV at each position. Higher emission energies are observed near the domain limits. The qualitative correlation of $\sim 30\text{--}50$ meV emission energy increase with SEM imaged boundaries indicates that growth grain surroundings act as barriers for the carriers.

Energy maps

To find further evidence of the confinement of carriers within QW domains, we can investigate the emission energy distribution associated to the e-beam position. We search for hints of higher emission energy in the vicinity of the domain delimitation. To this purpose, we need to first select the spectral range of interest, that is, above the QW emission. Let us take the example of sample U. Its QW emission being centered on 2.67 eV, we select the energy range above 2.8 eV — stopping at 3.9 eV — yielding the CL intensity map of Figure 4.4(a). We see that when the e-beam is located on the domain boundaries, an overall lower emission efficiency is observed, in line with the previous CL intensity maps for the QW emission. A reason for these features could be the higher concentration of NRCs between growth grains and a lower QW injection due to nonradiative recombinations of carriers generated in the bulk GaN.

Second, we can integrate the spectra over this range at each position and compute the mean emission energy. This computation is represented in Figure 4.4(b). This heuristic approach allows to reveal the positions where injecting carriers leads to higher energy radiative recombinations. Qualitatively, we can attribute these emissions to carriers that recombine radiatively before diffusing away. From the comparison of the energy map and the SE image, we conclude that higher emission energies are observed preferentially on the grain boundaries. Although this technique is not a direct probing of the energy landscape within the QWs, these results point toward higher energies correlated to the surroundings of growth grains, thereby acting as barriers for the carriers. Quantitatively, we observe a mean energy shift of $\sim 30\text{--}50$ meV.

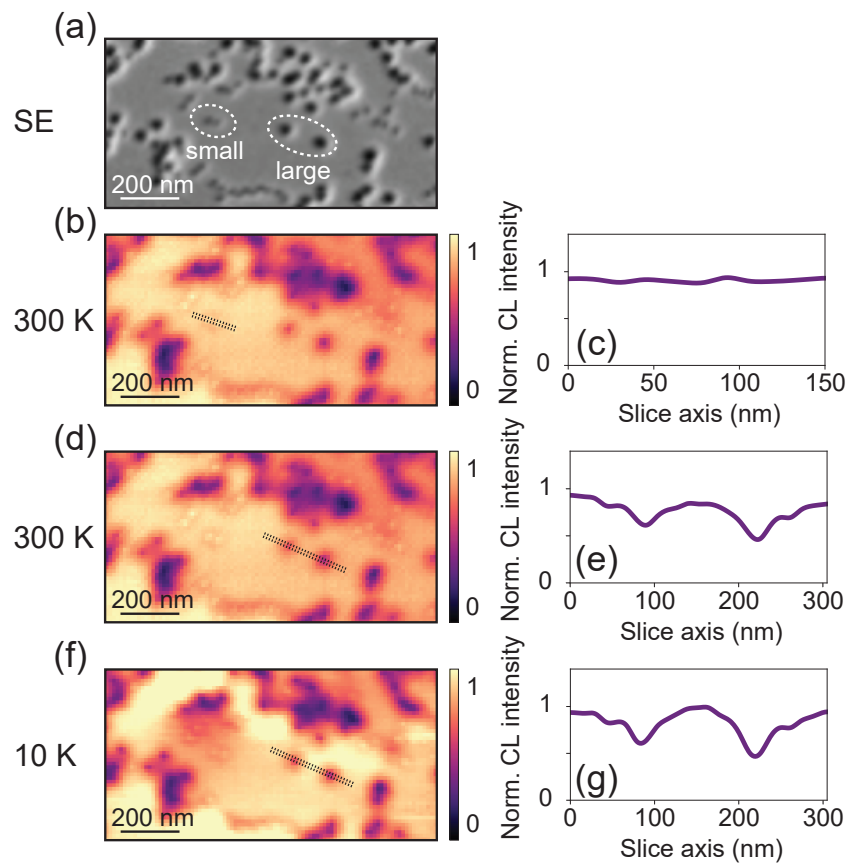


Figure 4.5: (a) SE detail view of an area from sample U, exhibiting the two different V-pit sizes. (b) & (d) respectively (f): Room-temperature resp. cryogenic CL panchromatic images revealing two types of V-pit behaviour. (c), (e), (f) Corresponding linescans.

V-pit nature

Let us now come closer to the V-pit CL signature. We represent an SE detail view of an area from sample U in Figure 4.5(a). On this image, we can see two classes of V-pit size, as identified in Section 2.2.1. From there, looking at the room-temperature CL panchromatic image (*cf* Fig. 4.5(b), (d)), we can identify two types of V-pit behaviour: one type appears bright, as seen from the linescan of Figure 4.5(c), and the other one impacts the CL intensity within an approximate diameter of 60–80 nm. This clearly requires a deeper analysis.

First, we can seek in the literature we summarised in Section 1.7. The two populations could be likely attributed to two different TD natures, namely edge or mixed (pure-screw are seldom observed). From there, a naive conclusion would be that edge-type dislocations, usually leading to smaller pits, are inactive while solely the mixed TD are NRCs. This could be supported by the fact that from a rapid counting of the bright dots in the CL mappings and comparing to the total SE pit amount, we arrive to a proportion similar to that of edge-type TDs as assessed from TEM measurements (sec. 2.2.2).

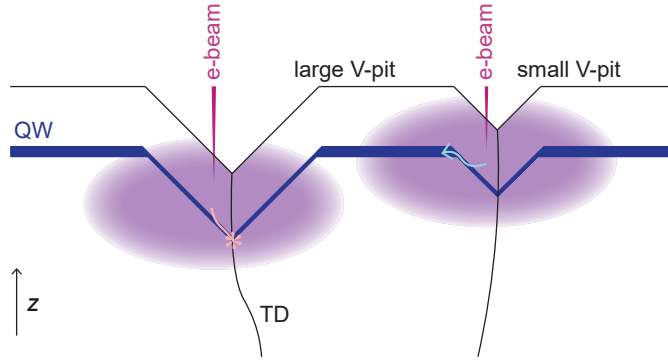


Figure 4.6: The high resolution achieved with our specially designed samples, 60 nm, is still insufficient to image the smallest V-pits. In simpler terms, TDs shielded by smaller V-pits remain beyond the resolution capabilities of the CL system.

Let us clarify that in the present results, the V-pits should all affect the QW, as the former are > 20 nm and the latter is situated 15 nm below the surface — in other words, the V-pits are formed before the QW growth. Hence, the energy barrier generated from thinner QWs in the V-pit sidewalls has to be considered. Therefore, when carriers are injected in the vicinity of the V-pit, they possess a higher energy than when injected in the surrounding QWs (*c.f.* Fig. 4.4). The pit would appear dark under two conditions:

- a major proportion of the CL generation volume coincides with the V-pit;
- the carriers nonradiatively recombine onto the TD.

We see now that the conclusion presented above neglects the first condition. Moreover, this condition is harder to reach for smaller V-pits, usually associated to edge-type TDs. The very high resolution we achieve with our specially designed samples, 60 nm (*c.f.* Fig. 4.1), is still not sufficient to ensure the excited region does not spread over the QW surrounding small V-pits, as schematised in Figure 4.6. Here, we can give an important conclusion: The literature shows that TDs cause nonradiative recombinations in bulk GaN (*cf* Sec. 1.7). The fact that some pits appear bright — because (i) the CL generation volume covers the free QW around and (ii) the V-pit screens the TD — means that the relaxation of the carriers generated in the bulk GaN toward the QW prevails their nonradiative trapping onto TDs.

4.1.3 Carrier domain simulations

To model the impact of PDs in the presented CL mappings, we first need to describe what happens during the dwell time of the e-beam at each position.

The 2D diffusion equation is typically expressed as:

$$\frac{\partial n_{x,y}}{\partial t} = D\nabla^2 n_{x,y} - \frac{n_{x,y}}{\tau} + G_{\text{QW}} \quad (4.3)$$

where:

- $n_{x,y}(r, t)$ is the 2D carrier concentration at a distance r from the e-beam position (x, y) , at time t ;
- D is the carrier diffusion coefficient;
- ∇^2 is the Laplacian operator for 2D spatial diffusion;
- τ is the carrier lifetime (recombination time);
- G_{QW} is the source term for carrier generation.

Note that the source term has been adequately replaced by the 2D generation rate in the QW determined in Section 4.1.1. The recombination of carriers can be associated to their overall lifetime τ .

To account for the impact of PDs, we can define a diffusion length in an ideal QW with no SRH processes, expressed as

$$L_D = 2\sqrt{D\tau_R} \quad (4.4)$$

and from this, count the PDs in this area.

To take into consideration the energy barriers from V-pit arrays, I developed a software enabling to draw lines similar to the energy map from Figure 4.4. The code blocks the counting of PDs situated behind these lines. Such a phenomenologic approach allows to generate a map of the impacted areas. The position of PDs is determined randomly at first, based on an expected PD density, and we then modify the position of some PDs to try to mimic the experimental CL mapping. The map of energy barriers and PDs is reproduced in Figure 4.7(a). For the output

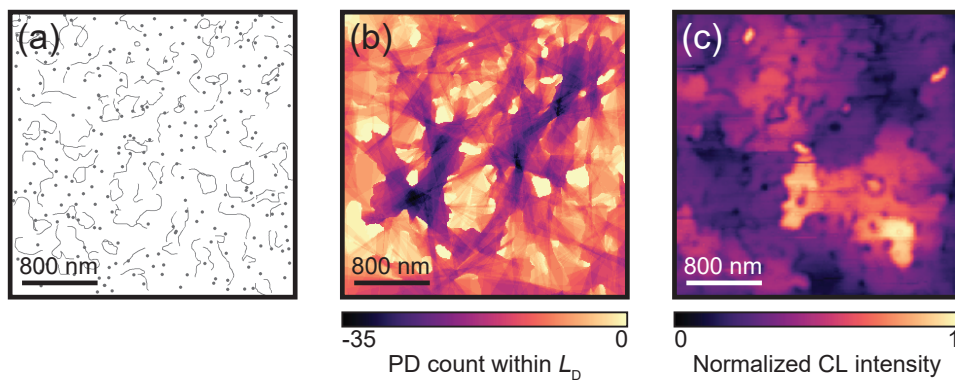


Figure 4.7: (a) QW domain boundaries assumed from the energy maps of Figure 4.4. The dots are semi-random positions for PDs to tentatively simulate the CL mapping shown in (c). (b) Result of the simulation code, which for each pixel accounts the defects in direct view.

represented in Figure 4.7(b) representing the amount of detrimental SRH centers contributing to each measurement position, the diffusion length was set to $1 \mu\text{m}$.

4.1.4 Spatially resolved cathodoluminescence and associated carrier lifetimes

Now that we have performed CL mappings, we could wish to verify if there is a relation between the defect concentration and the effective lifetime of the different domains. We know that the effective lifetime of the carriers is proportional to the inverse defect density:

$$\tau_{\text{eff}} \propto \frac{1}{N_{\text{PD}}} \quad (4.5)$$

Therefore, comparing the CL intensity mappings to CL lifetime measurements would raise another evidence of the impact of PDs. In addition to this, we could seek to quantify the impact of the PDs on the intrinsic lifetime of an ideal QW. The present section describes measurements taken by Dr. G. Jacopin at CNRS on the same samples R and U.

The physical phenomena at play are the same, the difference is that instead of simply recording the luminescence during a given integration time, a Hanbury-Brown and Twiss interferometer is used to measure the CL photon autocorrelation function $g^{(2)}$. From these $g^{(2)}$ measurements, it is possible to access the CL carrier lifetimes with the same spatial resolution as for the previously presented CL mappings.[114] In the present experiments, the acceleration voltage was set to 3 kV and the probe current was around 100 pA. In Figures 4.8(a), (d), we show the CL intensity maps at 300 K for samples R (top) and U (bottom). The mapping sizes are different for the two samples. Below the maps are histograms of the occurrence of intensities. As observed in our previous measurements, sample R has more zones with low intensities compared to sample U. This is a confirmation of the overall lower IQE when no UL is grown to prevent the generation of PDs in the QW. As it will be seen in the next section, such distributions would correspond to areas with different PD densities. To estimate the number of PDs per domain in sample R, we consider a PD concentration of $\sim 1 \times 10^{16} \text{ cm}^{-3}$, following what has already been measured in very similar QWs, although grown on sapphire or free-standing GaN, *i.e.* for different strain states and TD densities.[14, 15, 102] These results should be transposable, since another recent study highlighted the predominant role of the GaN buffer growth temperature, which is commonly $\sim 1000^\circ\text{C}$ for MOCVD growth.[13] In a 2.6 nm InGaN QW, such a density would correspond to about 5 defects over an area of $\sim 0.5 \mu\text{m}$ in diameter. Meanwhile, in sample U a PD concentration of $\sim 1 \times 10^{15} \text{ cm}^{-3}$ is expected.[14, 102] As a consequence, half of the domains are PD-free while the other half contains only one.

From the CL $g^{(2)}$ data, we can extract the carrier effective lifetimes τ at each e-beam position. The lifetime maps are shown in Figures 4.8(b), (e). Beware of the different lifetime colormaps for R and U. There exists a strong correlation between the intensity and lifetime maps, because the presence of more SRH centers solely increases the rate of nonradiative recombinations at the expense of radiative ones, as explained in the previous chapters. The radiative lifetimes should therefore be comparable for the samples under scrutiny. Hence, a longer lifetime indicates a higher IQE.

The capital letters correspond to zones from which we show the decay profiles in Figures

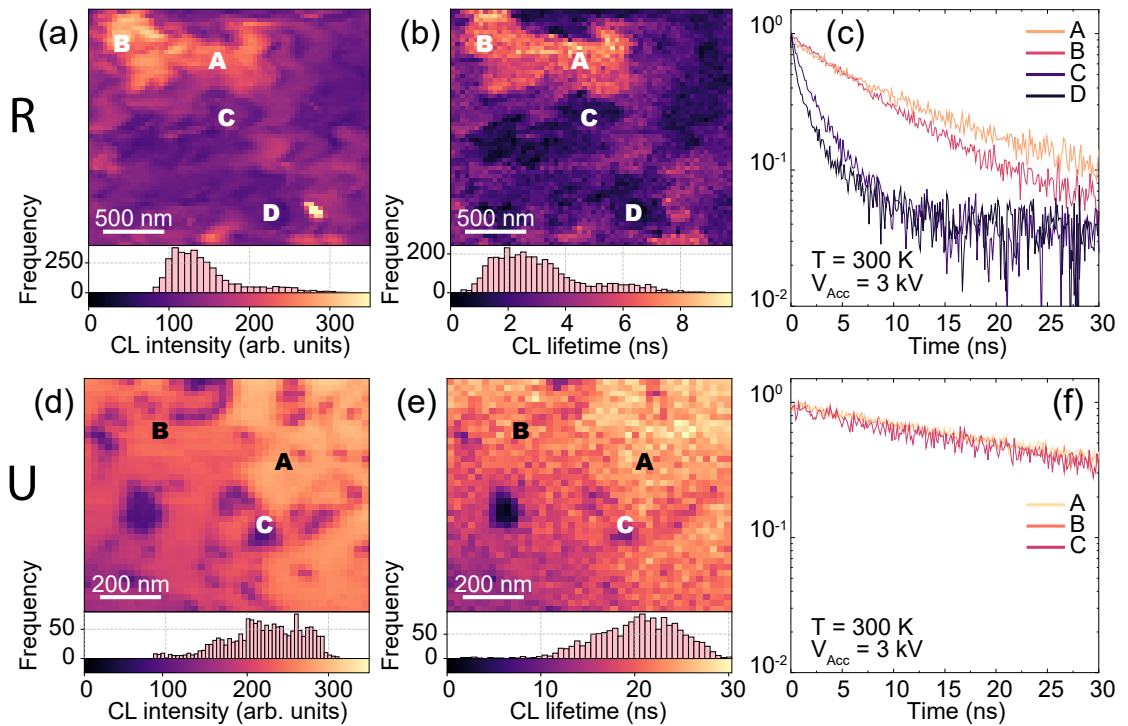


Figure 4.8: CL intensity and carrier lifetime maps for samples R (top) and U (bottom). (a) and (d): CL intensity maps with histograms illustrating intensity distributions. Sample R exhibits more zones with low intensities, indicating lower IQE due to the absence of an UL. In contrast, sample U shows mainly defect-free areas. (b) and (e): carrier lifetime maps, with different colormap scales for samples R and U. The strong correlation between intensity and lifetime maps owes to longer lifetimes being associated with better IQEs. Capital letters correspond to zones from which the decay profiles of subfigures (c) and (f) are taken.

4.8(c), (f). The longer lifetimes are measured in sample U, reaching 30 ns. These values would be close to the pure radiative lifetime τ_R , measured in areas without any PD and far from NRCs. Of course, this supposes that there is no other NRCs of different nature. In sample R, the effective lifetime strongly varies spatially. Even more striking, these variations are defined over distinct areas, which correspond to the grain domains.

4.2 Discussion

From the present nanoscale study of the QWs, we construct a comprehensive vision of the QW properties. The fact the QWs are not homogeneous in the plane is now an evidence. As a matter of fact, not only TDs create dead layers as suggested before, [85–87] but they structure the active region into a patchwork of carrier-isolated hundred-of-nm-scale QW domains. This is inherent to the growth of thin-films on Si foreign substrates, leading to numerous growth grains. In samples where PDs have not been eliminated, that is, samples with no In-containing UL, the random distribution of PDs generated in the active region [13, 15, 115] leads to QW

Chapter 4. Nanoscale optical properties of InGaN quantum wells

domains with quite different IQEs. Our understanding of the QW as a sum of independent areas reflects in the good agreement between our phenomenologic model and the CL mapping experiment of Figure 4.7.

With this vision, we can revisit previous results. The mesoscopic PL measurements do not take these variations into account, which is why setups relying on optical pumping are not able to probe the two-dimensional physical properties of such QWs, due to diffraction-limited laser spot sizes.

Summary

In this chapter, we delved into the nanoscale optical properties of InGaN QWs, building upon the broader measurements discussed in the previous chapter. While previous analyses provided averaged characterisations, we recognised the importance of a 2-dimensional nanoscale understanding of QWs and the carrier localisation by growth grain boundaries.

To this purpose, we used the CL technique on these specifically designed samples allowing a high-end resolution of 60 nm. We described the physical phenomena at play during the e-beam energy deposition and the recombination processes.

From steady-state CL intensity mappings we have shown that QWs are fragmented, while energy mappings gave evidence of carrier barriers at the growth grain boundaries.

We investigated the CL signature of different V-pit families, elucidating differences in CL intensity mapping behaviour. Very interestingly, our results demonstrate that carriers generated in the bulk GaN close to TDs prevalently relax to the neighboring QW instead of nonradiatively recombining onto the TD.

To model the impact of PDs in such a complex QW landscape, we developed a code considering area boundaries as energy barriers in the PD contribution in IQE reduction. The results align well with the experimental CL mappings.

Nanoscale CL lifetime experiments were carried out to probe the QWs and comparatively analyse the distribution of CL intensities and lifetimes. Their correlation emphasised the role of PD density in affecting carrier dynamics.

This analysis, by giving a novel vision of QW landscapes, provided insights into carrier confinement within QW domains and highlighted the influence of growth grain boundaries on emission characteristics.

5 GaN on Si photonic devices

To fabricate specific photonic devices, Si substrates can be very interesting. For instance, it is possible to fabricate suspended III-N membranes by using selective gas-phase etching. In the present chapter, we will build on our deep understanding of GaN-on-Si systems to incorporate InGaN/GaN QWs with decent efficiencies in photonic devices.

5.1 Nanobeams

The aim of the present application devices is to study the quantum optical properties of nanobeam semiconductor lasers. A laser consists of an active region embedded in a cavity, providing enough gain to exceed the optical losses of the latter. Beyond conventional macroscopic lasers, nanolasers present a cavity whose size is close to the diffraction limit (*i.e.* where the volume of the optical mode V approaches $\left(\frac{\lambda}{n}\right)^3$, where λ and n are the emission wavelength and the refractive index of the embedding medium). Over the past few years, the progress made in terms of nanofabrication of photonic crystals (PhCs) and suspended semiconductor membranes has led to the emergence of a new class of nanolasers with high spontaneous emission coupling factors (β). [116] Such structures differ from their conventional counterparts by the absence of any sharp threshold. Experimentally, there is no strong increase in the emitted light intensity and no pronounced narrowing of the emission linewidth when input-output power-dependent excitation measurements are led. Instead, power-dependent second-order correlation function at zero time delay ($g^{(2)}(0)$) measurements are required to observe the progressive transition from the spontaneous to the stimulated emission regime. [117, 118] In this regard, one-dimensional PhC nanobeam cavities appeared to be a first-choice testbed for exploring the related physics thanks to their peculiar light confinement features; namely the specificity of the transition from thermal to coherent light emission under CW excitation operating conditions, due to the high β -factor. [118–120] In addition, this small-footprint design is suitable for integration in lab-on-a-chip photonics; needle-like biosensors are another promising application, [121] and photonic integrated circuits would benefit from devices exhibiting low-threshold coherent emission features. Among these nanostructures, blue emitting high-

quality factor (Q) III-N nanobeam PhC cavities containing an InGaN/GaN QW gain medium belong to the few such devices that exhibit low threshold CW lasing at room-temperature.[118, 119] This is made possible when the fabricated nanostructures simultaneously exhibit a high Q value¹ and a high β (> 0.1) in an almost diffraction limited volume. In such a case, photons are efficiently funneled into the supported optical modes of the nanobeam.

These suspended membrane structures can be fabricated using a one-step pattern transfer method,[122] enabling a better precision in the PhC manufacturing, yielding higher Q factors than previous works.[123] The fabrication, detailed and illustrated in Appendix B, relies on the nanolithography of a hard mask of hydrogen silsesquioxane (HSQ) atop the III-N epilayers; once the latter are etched, their growth on Si(111) allows a quick underetch to release the semiconductor membrane. The drawback is a rather poor crystal quality due to both the obligation of using Si substrate for the air-gap creation, and the need for a thin membrane to support a few optical modes only. The MOCVD heteroepitaxial growth of the III-N membrane thus yields a high density of threading dislocations, as characterised in Chapter 2.

However, the needed $g^{(2)}(0)$ statistical measurements, justified by the blurred onset of coherence in the nanobeam light emission, critically depend on the amount of collected light. To tackle this, we particularly worked on the III-N growth structure and on the PhC design. These new developments enable a study of a new kind, namely the impact of the excitation source coherence on the quantum optical emission properties of the nanobeam platform, which remains to be explored.

After introducing the objectives of the intended study, we present the first results in four themes: the growth of the semiconductor membrane, the design and simulation of the PhC cavity, the nanofabrication process, and the characterisation of the nanobeams.

5.1.1 Growth

Nanobeam lasers, exactly like their conventional edge-emitting counterparts, consist of an active region embedded in a cavity; the in-plane light confinement relies on Bragg mirrors made of nanoholes drilled in a suspended semiconductor membrane acting as a waveguide;[124, 125] the out-of-plane confinement is due to total internal reflection.

The active region, providing gain, has to meet a number of requirements:

First, the need to create an air gap below the membrane implies to under-etch the substrate on which the semiconductor layers are grown. The growth on Si(111) enables this under-etching thanks to the high selectivity of the etching gas (XeF_2) with regard to III-Ns.[126]

Second, to emit in the blue spectral range, we rely on InGaN/GaN QWs. The main requirement from the semiconductor structure is to provide bright luminescence, ideally having its

¹The Q -factor quantifies the damping of an oscillator. In the framework of optical cavities, it is the ratio of the stored energy to the energy lost per cycle and can be expressed as: $Q = \frac{\text{Resonance Frequency}}{FWHM}$.

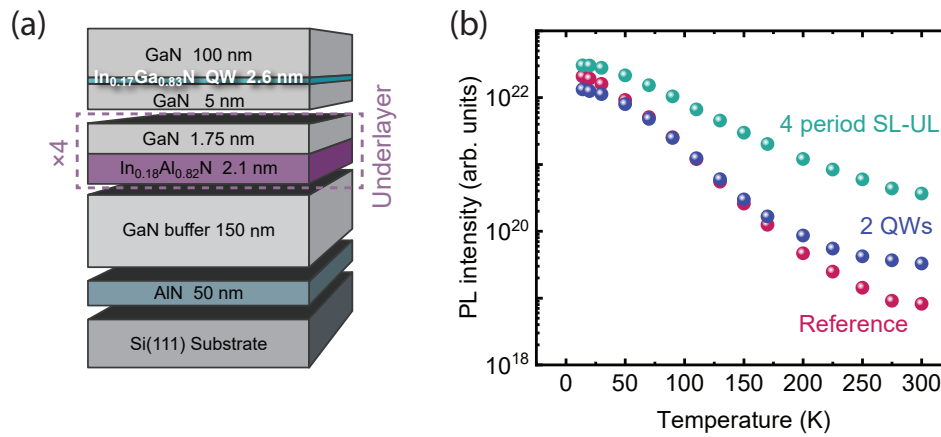


Figure 5.1: (a) Epilayer structure for nanobeam lasers. (b) Temperature-dependent PL measurements revealing surprising efficiency in the UL sample compared to the reference. Its reduced sensitivity to temperature increase proves enhanced IQE. Changes in extraction are less critical from one sample to the other than in the previous chapters, making intensities roughly comparable between samples. Note the efficiency increase upon adding a second QW, indicating the beneficial PD trapping effect of the deepest QW.

emission peak centered on the intended mode wavelength — in our case, 450 nm to 460 nm.

Third, it is also of great importance to locate the QWs close to the geometric center of the membrane; this ensures that the electron-hole pairs from the QW couple maximally to the transverse electric (TE) mode optically guided in the membrane.

Fourth, since the membrane acts as a waveguide, its total thickness has to remain below ~ 400 nm, to limit the number of supported optical modes. Here, we face the compromise between material quality (*e.g.*, thicker epilayers allow to manage strain better) and mode selectivity. 300 nm is found to be an optimum value for $\lambda \sim 450$ nm.[122]

We added a SL-UL in our samples, even though the density of dislocations was thought to limit the emission (total membrane thickness ≈ 330 nm). We report this structure in Figure 5.1(a). Here again, the UL sample is much more efficient than the reference one, as can be seen from the temperature-dependent measurements shown in Figure 5.1(b). This can be seen from the reduced impact of temperature on the PL intensity. Note that for these measurements, the change in extraction from one sample to the other is less critical than for higher vertical cavity orders, making the intensities roughly comparable. We can also conclude from these measurements that adding a second QW without UL increases a bit the IQE; this is due to the fact that the first QW partly buries the PDs and is thus beneficial to the upper QW. The design kept for the PhCs is the one sketched in Figure 5.1(a). The main consequence for the present application of nanobeams is that the experiments will require less pumping power, thus allowing to explore further the lasing regime.

5.1.2 Photonic crystal simulation

In parallel to the development and characterisation of the epilayer, I worked on the design of the PhC cavity. The aim of the structure is to provide optimum light confinement — *i.e.*, a high Q factor, and a small mode volume — yet with bright enough luminescence emitted in the out-of-plane direction, to ease the quantum optical characterisation.

The design of the Bragg grating allowing for longitudinal confinement is based on a PhC. The principle is based on the same phenomena as for the electronic bands described in Section 1.1.2. A periodic variation of the refractive index, generated by the holes drilled in the membrane, forbids the existence of photonic states. This is called the photonic bandgap. By adding a local change in the periodicity — *e.g.*, the absence of a hole, larger or smaller holes, etc. — a defect state can be created in the photonic bandgap. This state is where optical confinement appears.

Simulating such complex photonic structures requires softwares for the sake of accuracy. The structure is decomposed in a mesh of varying size, and at each cell, calculations can be conducted. We used the method of finite-difference time-domain (FDTD) to simulate our structures. A set of dipolar emitters is randomly placed in the QW region. From there, the discretised simulation cells are used to recursively compute the electronic and magnetic fields, by using their time and space interdependence.

We report on a design leading to an overall increase in the vertical light output of 1D PhC nanobeam cavities while preserving their Q factor. First, a nanobeam hole design less sensitive to fabrication errors is implemented.[125] Second, in the absence of any countermeasure, holes printed as circular actually present a 1.16:1 aspect ratio, and hence an elliptical shape — with the long axis parallel to the nanobeam axis — at the end of the fabrication process, which likely results from anisotropic strain present in the negative tone e-beam lithography (EBL) resist as the latter dries. We have evaluated the impact of such fabrication disorder with 3D-FDTD simulations. These have predicted an undesired blueshift (by ~ 15 nm) in the supported mode wavelength, from about 460 nm down to ~ 445 nm, accompanied by a $\sim 20\%$ decrease in the Q values. We thus implemented countermeasures by compensating the uniaxial strain introduced by the EBL resist through the printing of elliptical holes having their long axis perpendicular to the strain field, thus drastically reducing the ellipticity. The result is shown in Figure 5.2.

5.1.3 Clean-room fabrication

Once the design is chosen and simulated, I carried out the whole process flow in the clean-rooms of the EPFL Center of MicroNanoTechnology (CMi) and in the III-V cleanrooms of the Institute of Physics (IPHYS). The technical steps of this process are detailed in appendix B.

Since the PhC is intended for the blue spectral range, the Q -factor is highly sensitive to fabrication imperfections. The critical step is to create the HSQ hard mask by EBL, which

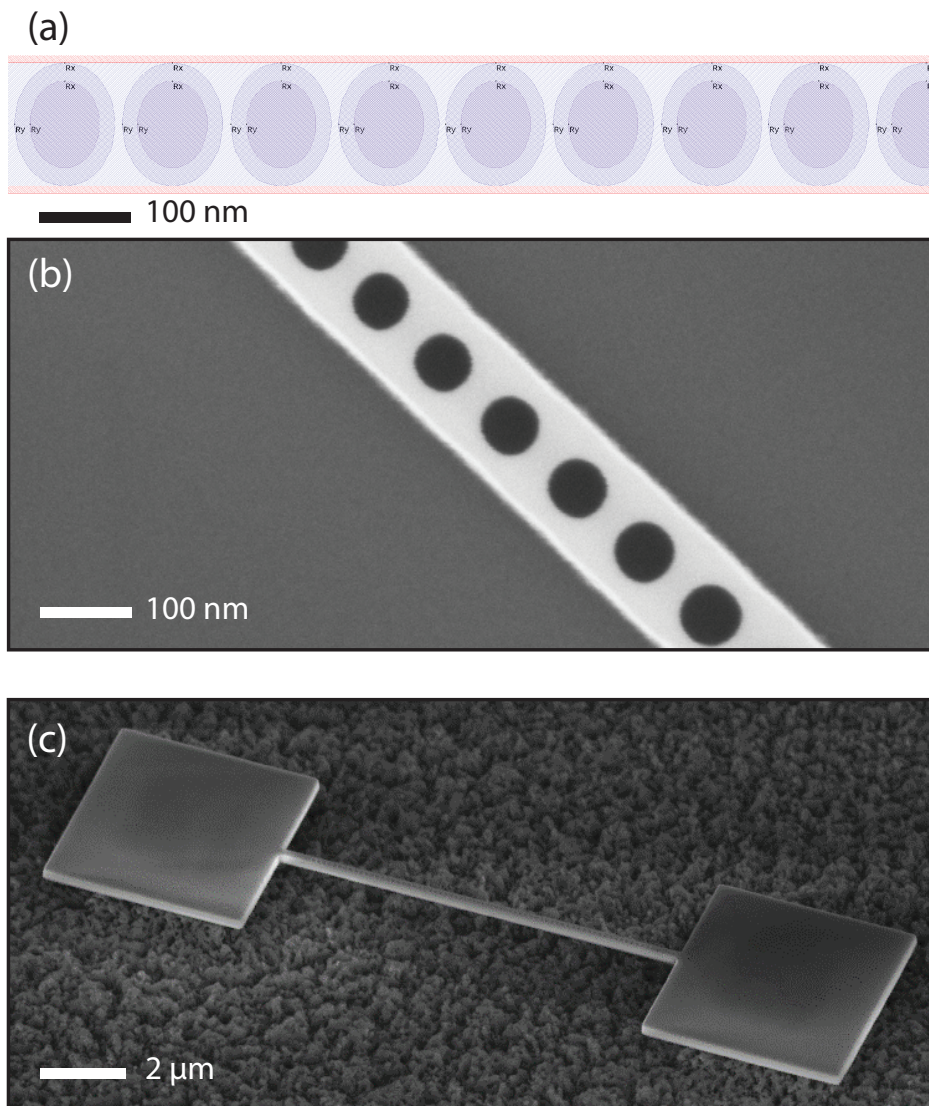


Figure 5.2: (a) Mask design with ellipticity precompensation. We show the SEM images of (b) the resulting printed EBL mask after development and (c) the complete suspended nanobeam PhC cavity after the whole fabrication process.

protects the III-N compounds during the one-step dry-etching pattern transfer.[122] This is an improvement compared to a more classical two-step process,[119] where the pattern was first transferred to the hard mask before the etching step. It allows maintaining the precision of hole positioning and regularity below 2 nm, which is primordial to achieve high Q nanobeams supporting blue photonic modes. We implemented an O_2 plasma mask hardening step after the EBL to enhance the pattern transfer precision.

After the pattern transfer, the membrane is released by XeF_2 gas-phase selective under-etching of the Si substrate (*cf* Fig. 5.2(c)). Finally, the HSQ mask is removed with buffered oxide etch. This step, depositing fluor atoms on the surface and removing oxides, justifies the need to

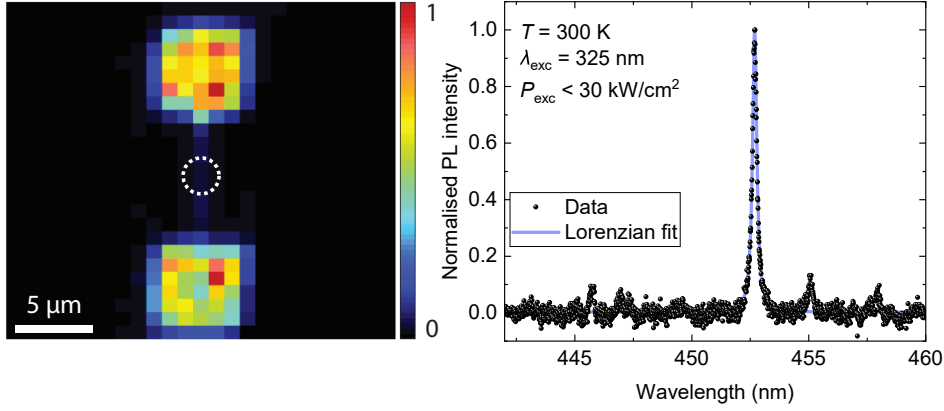


Figure 5.3: (a) Hyperspectral map obtained using the μ PL setup detailed in Appendix A. The map reveals the spatial distribution of PL intensity from the fabricated nanobeam sample excited with a CW $\lambda_{\text{exc}} = 325$ nm HeCd laser. (b) μ PL spectrum taken from the encircled area of (a), displaying the optical mode. The Lorentzian fitting yielded a Q factor of ~ 2040 at an emission wavelength of 452.7 nm.

clean and passivate the surface of the devices, because oxygen-rich surfaces proved to yield higher Q -factors: trials yielded the optimum treatment to be ammonia and oxygen rapid thermal annealing.[122]

5.1.4 Micro-photoluminescence

By using the micro-photoluminescence (μ PL) setup detailed in appendix A, we excite the fabricated samples with a CW $\lambda_{\text{exc}} = 325$ nm HeCd laser and collect the emitted light through the same 80x microscope objective. The microscope objective, mounted on a piezo-stage, allows to scan the sample for both excitation and light collection. The generated signal is analysed in a spectrometer, creating a hyperspectral map; we present the intensity map from such a measurement in Figure 5.3(a). The μ PL spectrum displayed in Figure 5.3(b) presents an optical mode whose Lorentzian fitting yielded a Q factor of ~ 2040 at an emission wavelength of 452.7 nm.

This mode is assumed to be of TE polarisation; the resonance is in good agreement with the simulation — run with the dimensions measured from a SEM characterisation. The simulation, including a standard deviation of 2 nm for the disorder on the hole positioning and size, yields a Q factor of ~ 9980 . Since fabrication disorder (modeled by Q_{fab}) is already taken into account in the simulation, the discrepancy is likely due to absorption and scattering losses, respectively modeled by Q_{abs} , and Q_{sr} . [127] These effects impact the theoretical quality factor Q_{th} and yield $Q_{exp}^{-1} = Q_{th}^{-1} + Q_{abs}^{-1} + Q_{sr}^{-1} + Q_{fab}^{-1}$.

Among other measurements, to validate the present development in nanobeam PhCs, time-stability needs to be verified. To this purpose, spectra have been recorded on such structures over longer times, at excitation irradiances on par with the intended characterisation ones.

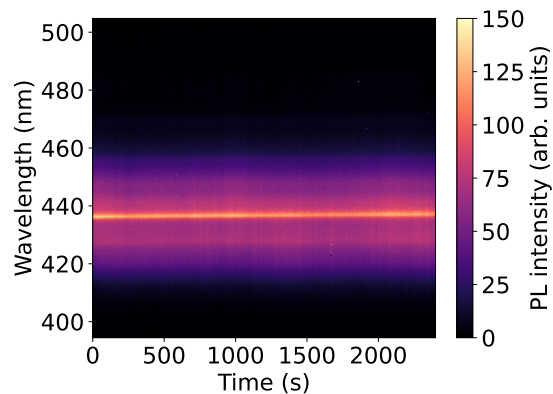


Figure 5.4: Spectral stability measurements of a nanobeam PhC. The bright horizontal line represents the spectral position of the nanobeam resonance over time, with a mean wavelength of 436.9 nm. The nanobeam in this figure is distinct from the one featured in Figure 5.3. The standard deviation of the resonance wavelength is 2.26 nm, demonstrating excellent stability over a duration as long as 2400 s. This robustness confirms the suitability of these nanobeams for applications in quantum photonics, paving the way for integrated blue quantum sources on silicon.

We report the time-data in Figure 5.4. The bright horizontal line is the spectral position of the nanobeam resonance over time, at a mean wavelength of 436.9 nm — this nanobeam is different from the one documented in Figure 5.3. The standard deviation of the resonance wavelength is 2.26 nm, proving a good stability over times as long as 2400 s. This confirms that the present nanobeams meet the requirements for being used for quantum photonics, opening the way to integrated blue quantum sources on Si.

Due to limited time, we did not pursue the research around this topic further, but future developments could involve electrical injection. From a more fundamental point of view, it could be of high interest to build such a PhC around a single photon emitter for studying *e.g.* cavity quantum electrodynamics.

5.2 Thin buffer LEDs

Capitalising on the results of Chapters 3 and 4 that show the beneficial impact of the In-containing UL on high TD density samples, we investigated thin LEDs where cavity effects are strongly pronounced. Not only we introduce such a layer into the epilayer design, but we go further and take advantage of cavity effects we have experienced in Chapter 3, this time aiming to engineer optimal extraction patterns.

5.2.1 Growth

The technical specifications for such devices are:

1. Optical constraints: the total thickness of the III-Ns and the position of the QWs need to be designed to generate the intended emission pattern.
2. Electronic constraints: to allow electrical injection of the carriers into the active region, a p-n junction is needed (see Sec. 1.6) which requires doped layers, and finally, p- and n-contacts need to be added.

With these specifications, such devices can represent a very complete example of what photonic engineering can be.

Historically, the issue of light extraction from semiconductors was tackled by redirecting all six light cones of the basic parallelepipedic structures externally. This allowed to compensate for not optimal light extraction. The breakthrough came from the principle of recycling light such that photons can, after several reabsorptions and reemissions in the active region, *in fine* fall into the light cone and contribute to the extracted light.[128] This method worked for optically pumped high-quality samples ($IQE = 99.7\%$) at a point where the extraction efficiency was multiplied by 36.[129] The authors mentioned in another publication that such an approach was very sensitive to material and mirror qualities, hence not compatible with electrical injection. Researchers demonstrated another way to randomize the direction of the trapped photons, by surface roughening texturation.[130, 131] In the same direction of adding wavelength scale material texturing, the use of surface or embedded PhCs can fold back the guided modes into the light cone, thereby greatly enhancing η_{extr} . [132] In the method of resonant cavity LEDs (RCLEDs), photon recycling can be provided either by simple refractive index contrast to the surrounding media or by the use of specifically designed distributed Bragg reflectors (DBRs).[133–136] For the present applications, we turn toward the simplest approach based on the high index contrast to both air (top) and Si (bottom).[137]

To design a microcavity LED, we need to fit into a thin film of material a set of building blocks, listed from the substrate to the surface (see Fig. 5.5(b)):

1. To start the growth on Si substrates, an AlN buffer is needed.

2. n-doped GaN follows to provide electrons as excess carriers.
3. We insert an 8-period SL-UL to bury the PDs below the active region.
4. The active region chosen consists in 3 QWs, separated by 5 nm barriers.
5. To keep carriers in the active region in order to maximise radiative recombinations, an EBL prevents electron overflow toward the p-type material; typically 15–20 nm $\text{Al}_{0.05}\text{Ga}_{0.95}\text{N}$ serves this purpose due to the slightly increased bandgap.
6. After this layer, the p-n junction is closed with the p-doped GaN (usually, ~ 60 nm is considered to be an acceptable thickness).

The design of the epi-structure is hence a compromise between minimal thicknesses of the above-mentioned layers and the optical thickness associated to extraction patterns. The thickness of the structure is calculated to maximize the vertical extraction for sample A4367 and to add a dephasing for sample A4368. To this purpose, we use an open-source software developed by the university of Ghent: CAMFR.[138] In contrast to the previously mentioned FDTD solvers based on spatial discretisation and calculations at each simulation cell, CAMFR is using eigenmode expansions to solve the Maxwell equations. This allows to run faster simulations by relying on index homogeneities in, *e.g.*, stacked layers. In each of these layers, the fields are written as a superposition of the eigenmodes. This allows to exploit periodicity in a much more efficient way than with FDTD calculations. Though, for computing a finite amount of modes, the structure needs to be encapsulated, similarly to FDTD spatial limits. To prevent parasitic reflections, these frameworks make use of perfectly matched layers (PMLs), that can absorb the energy thanks to their thickness written as a complex number. The resulting angular emission patterns simulated with CAMFR are shown in Figure 5.5(a). Note the compromise made in terms of both the EBL and the p-type GaN thicknesses, slightly below the ideal values, to maximise vertical light extraction from sample A4367.

Once the layers were fabricated, their emission was characterised by use of the PL mapping setup (*cf* Fig. 2.9). The wavelength of the samples is centered at 446 nm (A4367) and 456 nm (A4368). We report the intensity mappings in Figures 5.5(c)-(d) along with the Fabry-Perot coupling efficiencies to the PL setup (*cf* Figs. 5.5(e)-(f)).

To efficiently model the PL mappings, the NA of the setup was considered to be

$$NA \approx \frac{n_{\text{ext}}D}{2f} = 0.085 \quad (5.1)$$

where $D = 25.4$ mm and $f = 300$ mm are the entrance pupil (or first collection lens diameter) and focal length of the first collection lens. This very low value — compared to typical values of $NA = 0.5$, *e.g.*, for the microscope objective used in the setup of 3.1 — shows that we only collect a thin cone of light emitted very close to the sample normal. The modelling of Figure 5.5 takes this into account. Matching the measured mappings was only possible by considering a

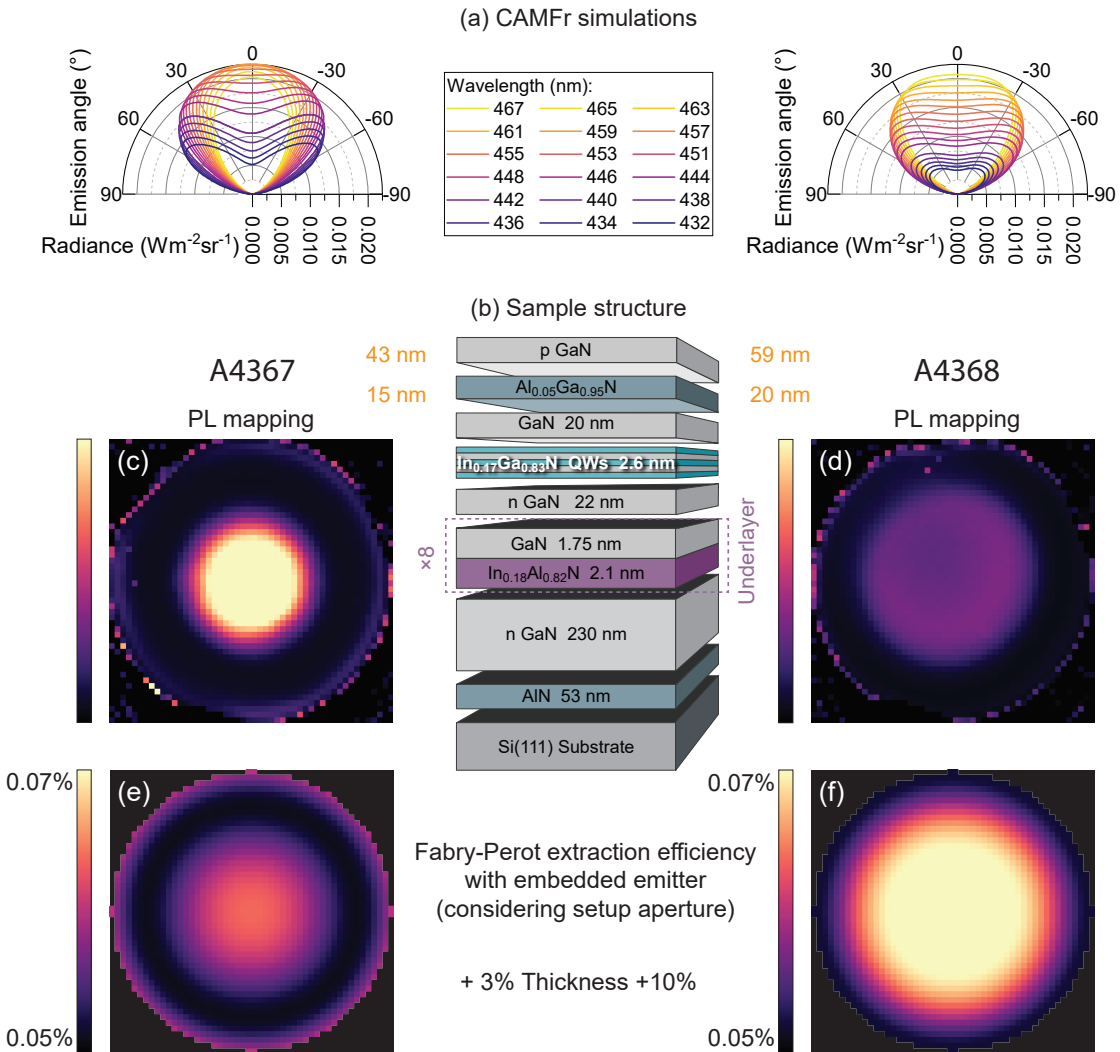


Figure 5.5: Simulation and characterisation of fabricated epi-structures for samples A4367 and A4368. (a) Simulated angular emission patterns using CAMFR, illustrating the compromise in the thickness of the EBL and p-type GaN layers to optimize vertical light extraction for A4367. (b) Thickness of the layers in both samples. Notice the critically thin EBL and p-type GaN layer of sample A4367. (c)-(d) Intensity mappings obtained from PL mappings for samples A4367 and A4368, respectively. (e)-(f) Corresponding Fabry-Perot coupling efficiencies to the PL setup. The low NA of the setup (0.085) selects light emitted close to the sample normal. The thickness adaptation over the wafer radius accounts for interference effects, with at least one constructive and one destructive interference observed over one radius.

+25% thickness variation from the center to the side of the wafers. Compared to the nominal growth thicknesses, the centers of the wafers needed to be adapted by +3% and +10% for A4367 and A4368, respectively. Note that over one radius, we observe at least one constructive and one destructive interference.

5.2.2 Clean-room fabrication

We present here some information worthy to be explained about the fabrication process.

The Si substrate adds a main constraint to the fabrication process: since light cannot be extracted through a transparent substrate, the top p-contact needs to be semi-transparent. We use a Ni-Au contact, made by evaporating successively the metals to form 5 nm-thick layers on top of the p-doped GaN. This was done after acid cleaning of the surface. After deposition, the layers are heated in an oven to make the metal atoms to diffuse for reducing the resistivity.[139–141] After the mesa etching step, we observed burnt resist, leaving residues. We solved this issue by implementing shorter and intermittent etching pulses (16 × 35 s instead of 750 s, dry etching with 8 mTorr Ar at 200 W). This was due to the presence of Ni, a hardly etched material needing longer times.

Over the semi-transparent p-contacts, we perform a lift-off to add a more resistant contact grid for spreading the current across the whole device. This step relies on so-called resist inversion, very sensitive to the inversion baking time and temperature. The recipe presented in Appendix C reports the optimal conditions found after numerous tests.

Post-fabrication optical micrographs are shown in Figure 5.6.

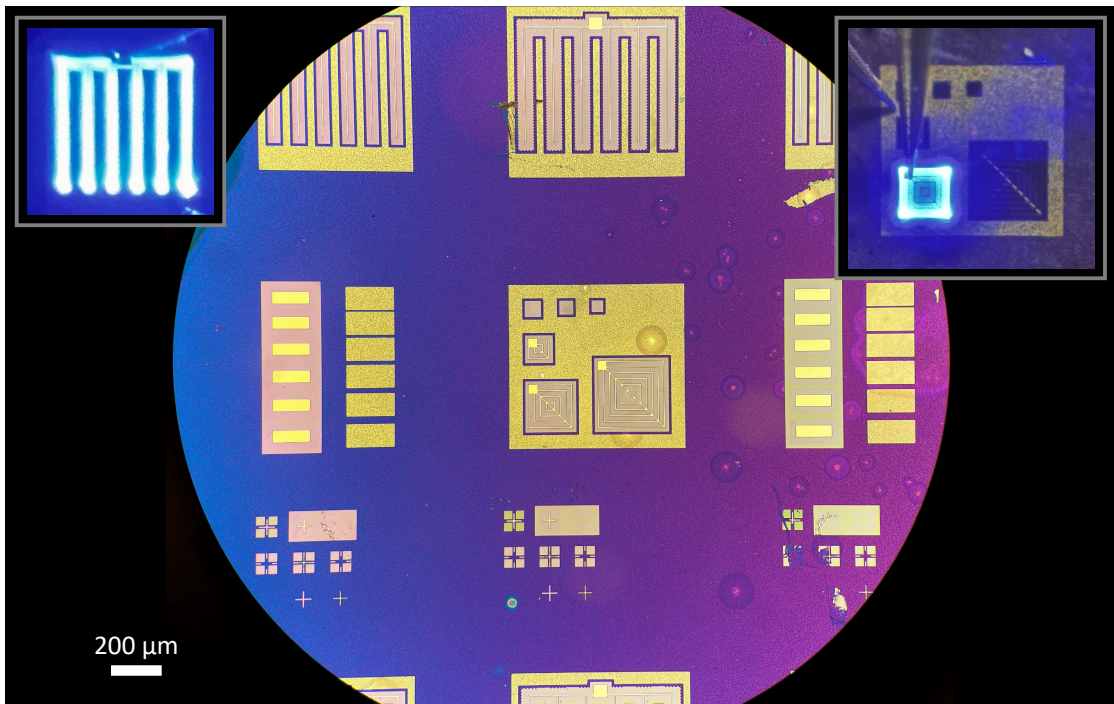


Figure 5.6: Optical microscopy characterisation. The insets showcase functioning devices, with electroluminescence irregularities in the upper right inset attributed to the lateral position of the contact needle and current crowding. The upper left inset reveals an alternative LED design, featuring an interdigitated format for enhanced current spreading.

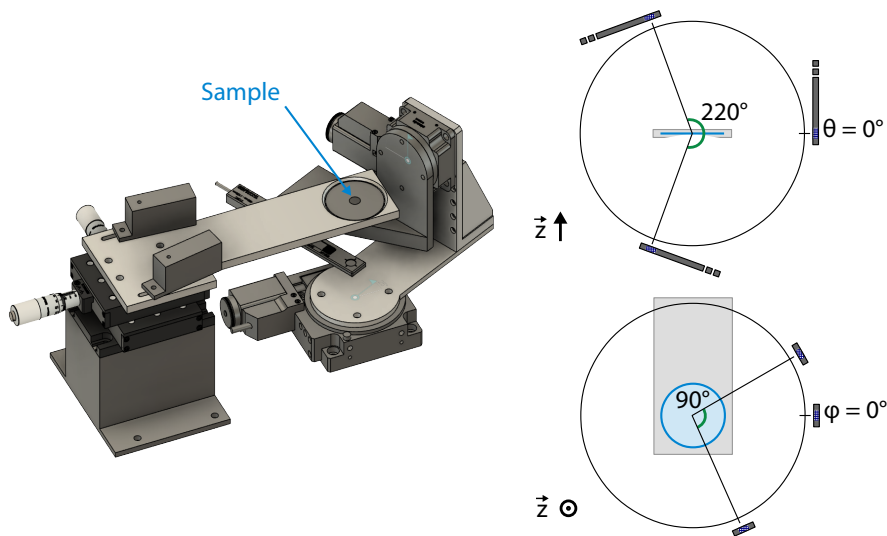


Figure 5.7: Angle-resolved EL system. Left: CAD hardware design incorporating two motors enabling the scanning of at least a quarter sphere, applicable to both top- and bottom-emitting devices. The entire half-space reconstruction is achieved through data symmetrisation. Right: accessible latitudes θ and longitudes ϕ .

5.2.3 Electroluminescence

To perform electroluminescence measurements, we designed and built a system allowing for angle-resolved EL measurements. The stage computer assisted design (CAD) is shown in Figure 5.7. Two motors allow to scan at least a quarter sphere, for both top- and bottom-emitting devices. We reconstruct the whole half-space by symmetrising the data.

During the experiments, it is important to find a processed device in a representative place of the inhomogeneous wafer (*cf* Fig. 5.5). A first rapid test of the LEDs can point toward the device of choice. We show in Figure 5.6 two insets of operating devices; inhomogeneities of luminescence are observable in the upper right inset. This is inherent to the lateral position of the contact needle, to minimise the shading on the light extraction pattern. Nonetheless, we perform the following measurements on such device shapes. The upper left inset pictures an alternative design of the LED, allowing better current spread thanks to the interdigitated format. Once a device is selected and connected to the power supply, we perform automated angle-dependent acquisition of the emitted power, at a list of current-voltage couples. Such measurements are eased through the in-house developed software I created for controlling the Standa positioning motors, the ThorLabs powermeter and the Keithley 2450 power supply.

In Figure 5.8, we report the results of angular EL measurements, for samples A4367 (left) and A4368 (right). The dashed line is the symmetrised datapoints. The good correlation between the simulated (top row) and measured (bottom row) angular emission patterns fosters our ability to accurately design and fabricate these devices.

The non-conventional p-contact, added to the presence of two orders of magnitude more

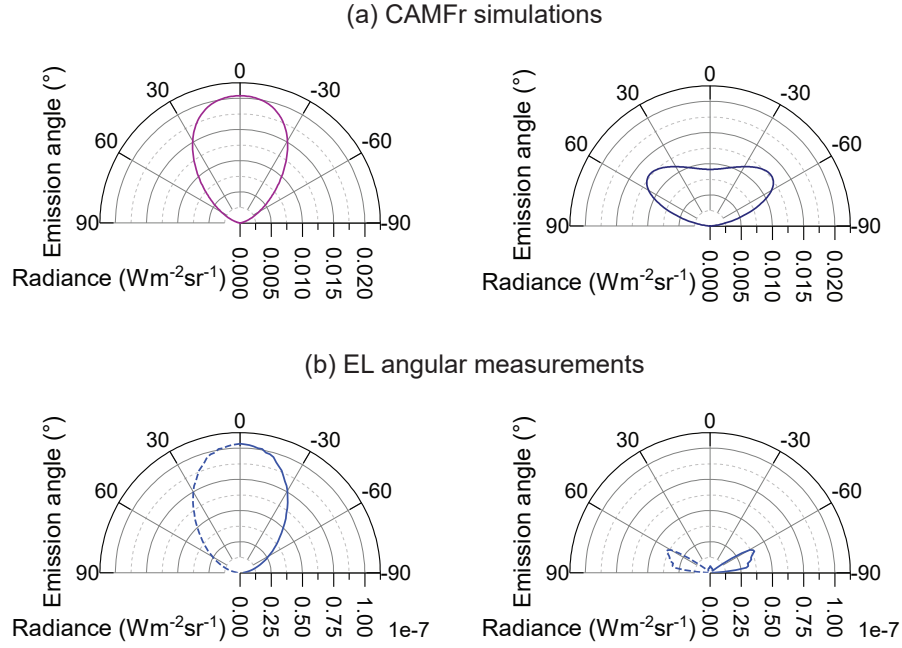


Figure 5.8: Correspondance between (a) CAMFr simulations and (b) angular EL measurements for samples A4367 (left) and A4368 (right). The symmetrised datapoints, depicted by the dashed line, enhance clarity. The alignment between the simulated and measured angular emission patterns underscores the precision in the design and fabrication of these devices.

TDs compared to standard devices, could degrade quantitatively the performance of those microcavity LEDs. To verify this, we compared the present samples to a reference grown on sapphire. For a quantitative comparison, we used the angle-dependent power measurements to calculate the whole emitted power. At each position (i, j) of the motors performing discrete steps of $\delta\theta$ and $\delta\phi$ (*cf* Fig. 5.7), the raw measure of power $p_{i,j}$ does not contain physical meaning unless it is converted into a *radiant intensity* (Wsr^{-1}), related to the detector solid angle Ω_{det} . Now we can extrapolate the overall power extracted in the discrete region of space associated to $(\delta\theta, \delta\phi)$:

$$\delta P_{i,j} = p_{i,j} \frac{\delta\Omega}{\Omega_{\text{det}}} \quad (5.2)$$

where the element of solid angle $\delta\Omega$ writes:

$$\delta\Omega = \cos(\theta)\delta\theta\delta\phi \quad (5.3)$$

This allows to access a precise measure of the total extracted power:²

$$P = \sum_{i,j} \delta P_{i,j} \quad (5.4)$$

²Here, we consider the whole emission of one light-emitting device. We could easily extract a *radiant exitance* (Wm^{-2}) because the present quantity relates to a surface $S_{\text{LED}} = 220 \times 220 \mu\text{m}^2$ from which light is emitted.

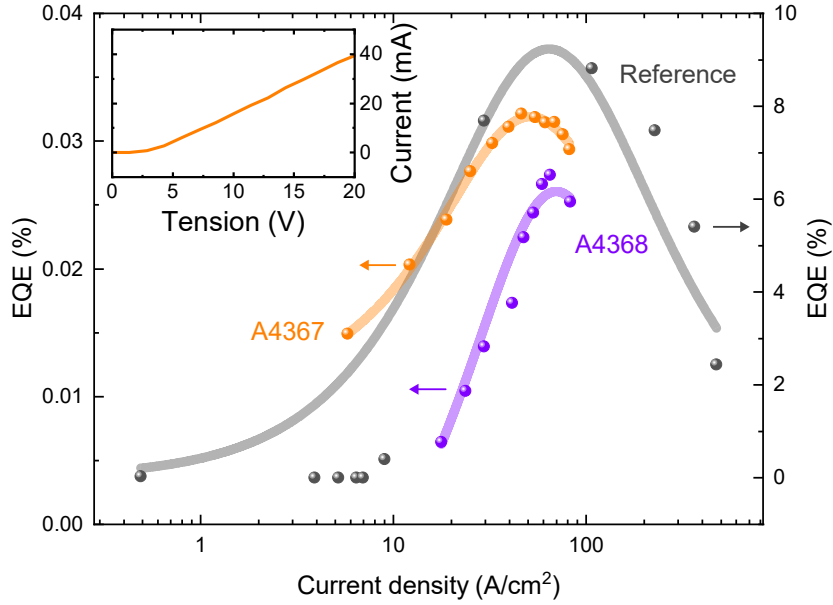


Figure 5.9: Experimental EQE against current density for three devices (surface area $S_{\text{LED}} = 220 \times 220 \mu\text{m}^2$). The consistent peaking of EQE in the $40\text{--}70 \text{ A cm}^{-2}$ range indicates similar efficiencies for all samples under scrutiny, attributed to the omnipresent In-containing UL. Differences among samples lie in extraction efficiency.

In fine, the EQE is expressed as:

$$EQE = P \frac{\lambda}{hc} \frac{q}{i} \quad (5.5)$$

From this rigorous treatment, we plot the experimental EQE *versus* current density for three devices of surface $S_{\text{LED}} = 220 \times 220 \mu\text{m}^2$ in Figure 5.9. From the present data, we see that all the samples present peaking of EQE roughly in the same region of $40\text{--}70 \text{ A cm}^{-2}$. The fact all three samples have their peak EQE at the same current density is due to the ubiquitous presence of an In-containing UL. In conclusion, these samples share a similar IQE, but differ through their injection and extraction efficiencies. From our simulations, we compute a maximum extraction efficiency of $\eta_{\text{extr}} = 8\%$ on the GaN-on-Si samples. We have to consider that the semi-transparent Ni-Au contact has only a transparency of $\sim 70\%$. [141] Under these conditions, to meet the $IQE \approx 49\%$ value measured in Chapter 3, we deduce an injection efficiency of $\eta_{\text{inj}} \sim 1\%$. The low value of η_{inj} is in line with the need for higher voltages to access similar current densities on GaN-on-Si samples compared to sapphire ones. We attribute this to both the imperfect current spreading in semi-transparent p-contacts (*cf* right inset of Fig. 5.6) and the eventual presence of shunts from TDs. This shows that there is room for improvement with regard to the electrical carrier injection.

With these results, we demonstrate the possibility of engineering GaN-on-Si blue emitters, paving the way for their integration as key building blocks in silicon photonic circuits.

Summary

In the present chapter, we presented two main applications for InGaN/GaN QWs grown on Si(111) substrates.

With the necessity for optically thin membranes to support precise photonic modes, the PhC nanobeam lasers are excellent demonstrators of how In-containing SL-ULs can be brought to their limits while maintaining high-class defect mitigation capabilities.

To illustrate how such a technology can benefit a wide range of developments, we accurately designed UL-embedding microcavity LED epistuctures. Here again, the fabricated devices were characterised and validated, showing a second example of how photonic engineering coupled to sharp material science know-how can push boundaries, opening new horizons for integrated silicon photonics.

Conclusion

To conclude this thesis, we will first summarize the main findings before analysing the methodology and closing the present work with an outlook on the opened perspectives.

Through SEM and cross-sectional TEM morphological assessments, we found in Chapter 2 that the V-pit surface density corresponds well to the density of TDs in the sample. Additional SEM and AFM measurements pointed toward the presence of growth grains delimited by V-pits and step-bunching; these grains were further investigated in Chapter 4.

Harnessed with high-resolution CL mappings, we answered the question of the consequences of such boundaries on the optical properties of QWs. This is how we discovered that QWs with high TD density QWs ($N_{\text{TD}} > 10^{10} \text{ cm}^{-2}$), rather than being quasi-2D landscapes with localisations centers and defects, are in fact an ensemble of subsystems of $\sim 0.5 \mu\text{m}$ in diameter. These subsystems, formed from growth grains, are delimited by arrays of TDs generating V-pits or by step-bunching inducing low In content regions. Both create energy barriers for the carriers.

Chapter 2 also investigated temperature-dependent PL, raising the questions of efficiency improvement by mitigation of PDs. Although originally thought to be shaded by the presence of TDs, we demonstrated in Chapter 3 that the introduction of an In-containing UL dramatically increases the IQE of the active region from a few percents to $\sim 40 - 50 \%$.

In the last chapter, we used our fundamental understanding of such epilayers to investigate cavity-based light-emitters. We fabricated devices with high efficiencies and transformed the curse of Si-induced interference effects into a blessing for microcavity LEDs design. Added to the explored ability to integrate our findings into nanophotonic designs, the present work is a further step toward efficient and versatile integrated silicon photonics.

Methodology

The experimental methodology was carefully chosen in order to create realistic testbeds appropriate for the theoretical questions whilst accommodating the performance of the available equipment — and in some cases, enhancing it. The investigation of the interplay between the surface morphology and the defects was led with high-end equipments allowing to probe

Conclusion

exactly what was needed — sometimes, needing collaboration with specialised platforms. An example of this is TEM: to access such high cross-sectional resolution of the sample structures, we needed to interact with the Interdisciplinary Centre for Electron Microscopy of EPFL. Apart being extremely complex and time-consuming, this method had the main limitation of probing the samples with the uncertainty on the feature overlay through the lamella thickness.

By the choice of Si substrates for the generation of high TD density testbeds, the optical investigations were intensely complexified due to added cavity effects, substrate absorption and the impossibility of substrate light outcoupling. To circumvent this limitation, we took advantage of serendipitous sample radial thickness variations, to tune the epilayer cavity to the QW emission wavelength. The interference Fabry-Perot modeling, although already satisfactory to predict and model the experiments, still has some limitations owing to the complex nature of epistructures. What was done in Chapter 5 by using the framework of CAMFR could be used to complete our platform-adapted, in-house developed software.

The nanoscale investigation by use of CL was already criticised in Section 4.1.2, with regard to the resolution limitation and the constraints it places on the epilayer design with a single, shallow QW. Simulating the CL mappings was a feasibility demonstration, and the presently created software still has limitations: a strong simplification to mention is the sole consideration of direct-view PDs — in other words, we need to further complexify the modeling to take into account carriers that could undergo scattering processes.

Finally, there remains room for improvement in our EL setup. Indeed, what is currently probed is a panchromatic light emission by means of a powermeter. By adding a fibered spectrometer to the rotating arm, we could bring our system to highest standards.

Apart from the methodological compromises, we can step back to evaluate the scientific method. The present study was led on samples where the TD density was constantly in the same range. We chose this condition to be able to probe in-depth the PD impacts in the high-TD density regime. This explicit limitation of the thesis can be the starting point of a further high-impact study. Indeed, repeating a selection of the present investigations while adding a TD-density variation in the samples could add another dimension to the current understanding of the interplay between PDs and TDs.

Perspectives

Apart from the extension of the present experiments to a range of different TD densities, the path for subsequent research starts with tackling more fundamental questions, like the depth and exact nature of the PDs.

To deepen our understanding of the QW domains, we could try to engineer artificial systems to simulate boundaries with varying PD densities.

Finally, we point out that the field of V-pit engineering has a bright future, as it will not solely

permit better controlled electrical carrier injection:[97, 98, 100] we are on the verge of shaping QWs at the nanoscale.

Closing remark

The outcomes of this work have enlightened the impact of point defects in the regime of high threading dislocation density. By delving deeper into this unexpected finding, nanoscale studies and experiments reshaped our understanding of InGaN/GaN quantum wells when subjected to high dislocation density.



Appendices

A μ PL setup

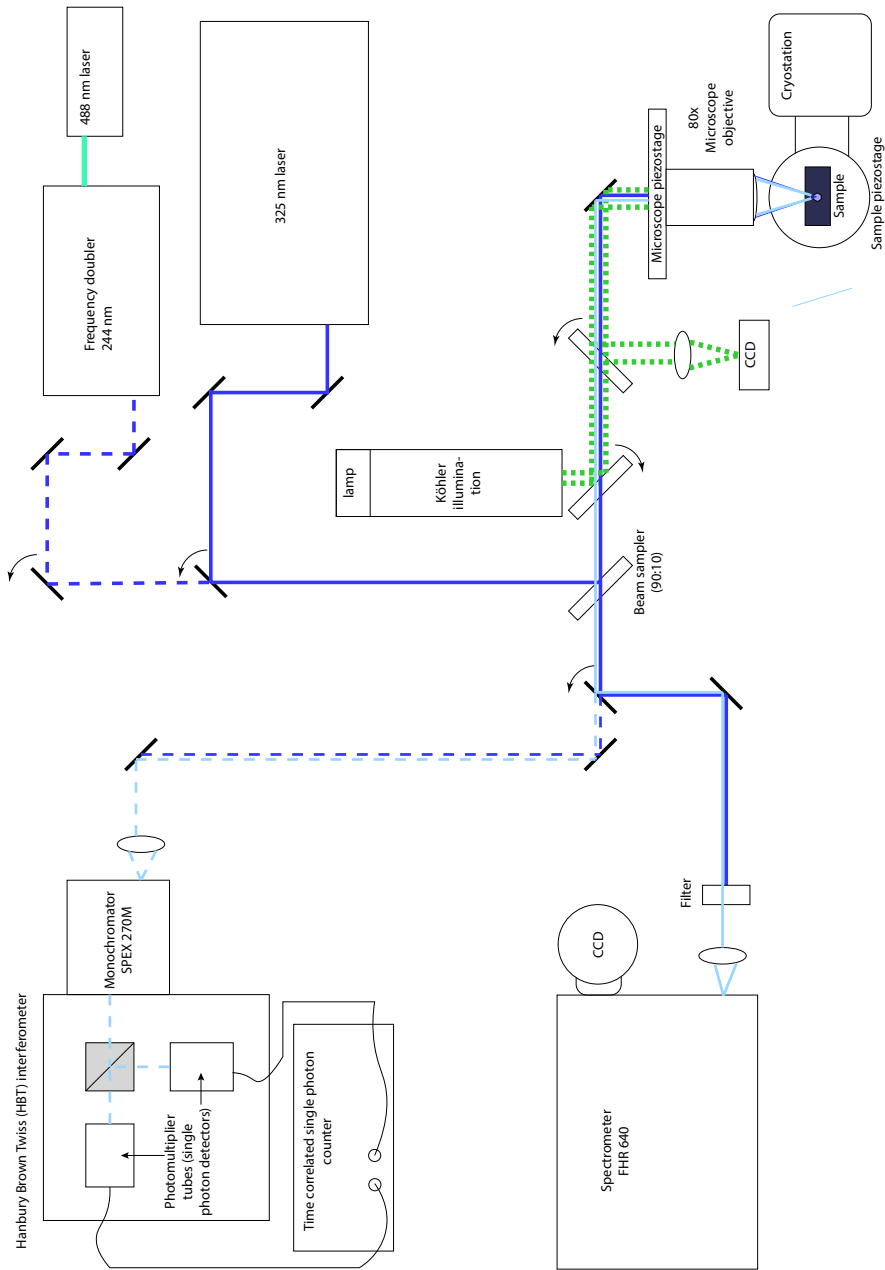


Figure A.1: μ PL setup.

B Process flow: Photonic Crystals

Semestral Project Master Project Thesis Other

III-Nitride Photonic Crystal Nanocavity Laser

Description

The goal of the project is to explore the quantum optical properties of nanolasers in an optical resonator based on a III-nitride photonic crystal. The gain medium is a single InGaN quantum well grown by metal-organic vapor phase epitaxy in the middle of the III-nitride epilayers.

The most critical aspects of the process are:

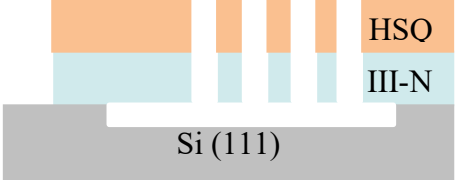
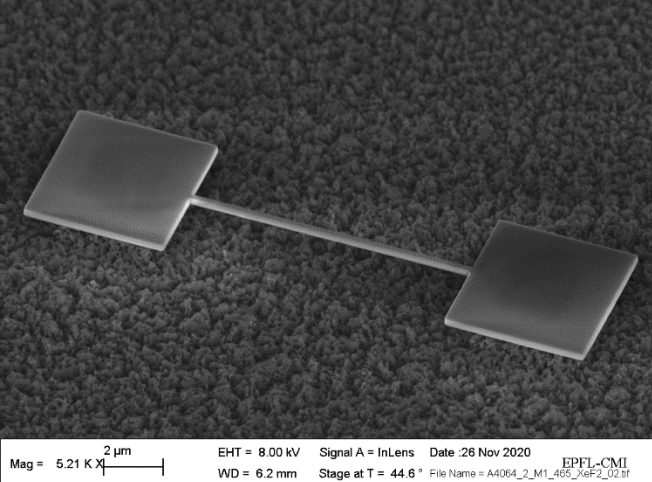
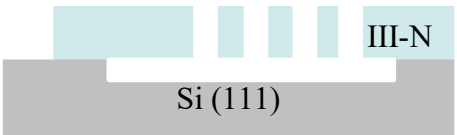
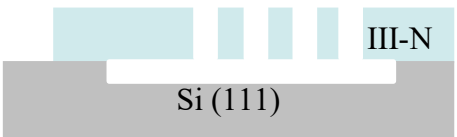
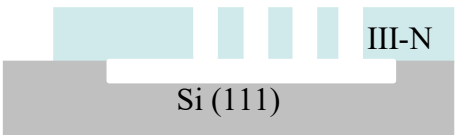
- few nanometer critical dimension control during electron beam lithography;
- subsequent pattern transfer with a high aspect ratio (>5);
- dry etch of sub-100 nm features;
- maintenance of a good sidewall surface quality.

Technologies used			
MOVPE, PECVD, O ₂ plasma, e-beam lithography, negative resist (HSQ/TMAH25%), III-V dry etching (Cl-N ₂), XeF ₂ vapor phase etching, HF, SEM, AFM, TMAH, spectroscopic ellipsometry, RTP			
Electron beam lithography masks			
Mask #	Critical Dimension	Critical Alignment	Remarks
1	30 nm	x	Dry etch mask for photonic crystal
Substrate Type			
Silicon <111>, Ø2'', 280±25µm thick			

Process outline

Step	Process description	Cross-section after process
01	<p><i>III-nitride growth</i> Machine: III-N MOVPE LASPE Thickness: Si (111) substrate/ AlN (50 nm)/GaN (110 nm)/InGaN quantum well (2 nm)/GaN (140 nm) Size: 2" wafer</p>	
02	<p><i>Dicing</i> Machine: Disco DAD Protective coating: 100 nm PECVD SiO₂ Chip size: 2" wafer -> 7.5 mm x 7.5 mm chips</p>	
03	<p><i>SiO2 removal</i> Bench: Z14 Wetbench Arias Acide Chemical: BHF</p>	
04	<p><i>Surface clean</i> Machine: Z2 Tepla GiGAbatch Process: O₂ plasma, High Power 7'</p>	
05	<p><i>E-beam lithography</i> <i>Photonic crystal</i> Machine: EBPG5000 Resist: HSQ 6% (90 nm) CD = < 30nm Base dose = 1800 μC/cm² PEC: η = 2.2 Developer: TMAH 25%, 2'</p>	

<p>06</p>	<p><i>HSQ mask hardening</i> Machine: Z2 Tepla GiGAbatch Process: O₂ plasma, High Power 5'</p>		
<p>07</p>	<p><i>III-nitride photonic crystal etch</i> Machine: Sentech ICP-RIE SI 500 (III-V cleanroom) Gases: Cl-N₂ (7.5-8', 80 nm/min)</p>		

<p>08</p>	<p><i>Membrane release</i> Chemical: XeF₂ Machine: Z11 Si Etcher Etch depth: 500 nm – 1 micron (3x18'', 2500 mTorr)</p>	
		
<p>09</p>	<p><i>HSQ strip and post-XeF₂ fluorine byproduct removal</i> Bench: Z14 Wetbench Arias Acide Chemical: BHF</p>	
<p>10</p>	<p><i>Surface clean</i> Machine: Jetfirst 200 RTP Process: RTA at 750°C and/or RTN at 750°C</p>	
<p>11</p>	<p><i>Surface passivation by oxidation</i> Machine: Jetfirst 200 RTP Process: RTO at 750°C</p>	

C Process flow: LEDs

Semestral Project Master Project Thesis Other

III-Nitride Blue-Emitting LEDs on Silicon Substrates

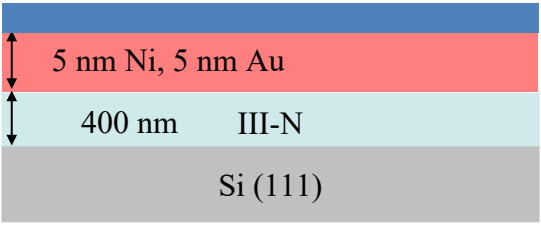
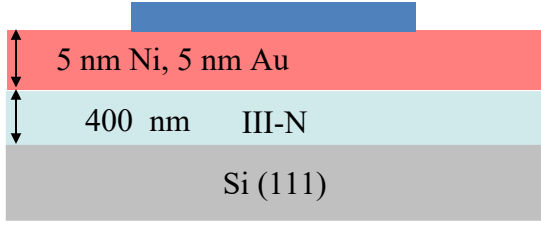
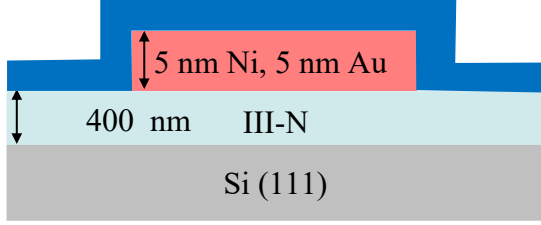
Description

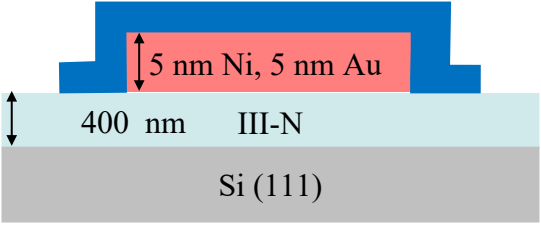
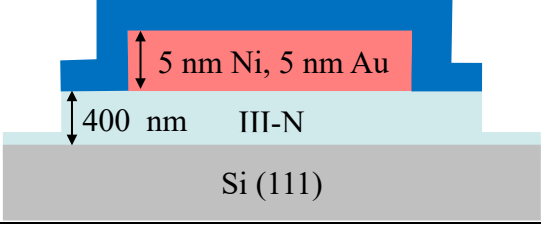
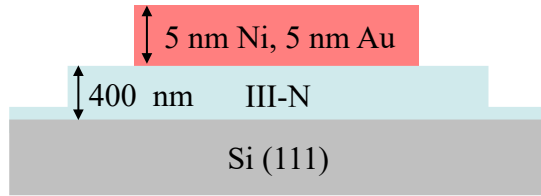
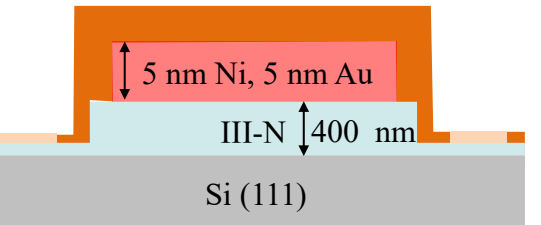
The goal of the project is to explore the efficiency improvement of Si(111)-grown LED structures based on III-Nitrides (III-N) thanks to an In-containing underlayer. The active region is a single InGaN quantum well grown by metal-organic vapor phase epitaxy in the middle of the III-N epilayers. The most critical aspects of the process are a precise photolithography patterning of both p- and n-type contacts and a critical depth control during III-N etching.

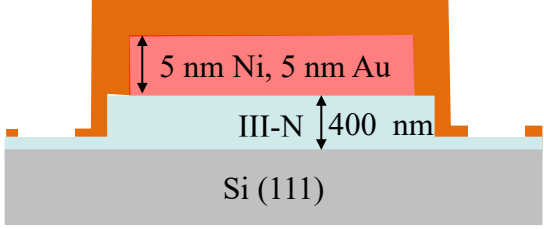
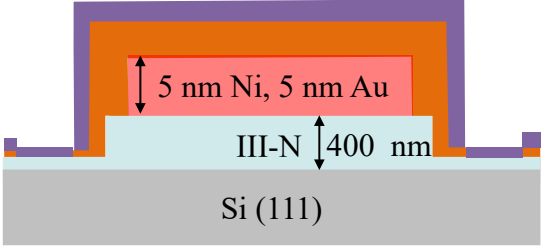
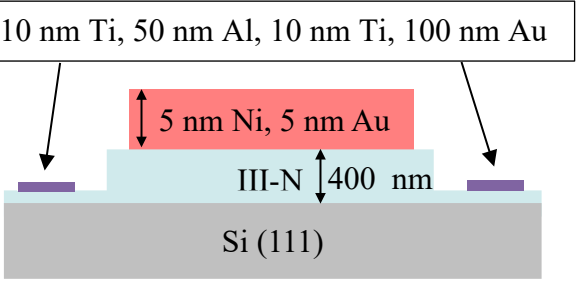
Technologies used			
MOVPE, RTP, HF, e-beam PVD, photolithography, positive inversible resist (AZ5214), RIE (O ₂ , Ar), ICP-RIE dry etching (Cl-N ₂), SEM, AFM, confocal microscopy			
Photolithography masks			
Mask #	Critical Dimension	Critical Alignment	Remarks
1	? nm	x	Masks for p-type contacts, mesa etching, n-type contacts
Substrate Type			
Silicon <111>, Ø2", 280um thick			

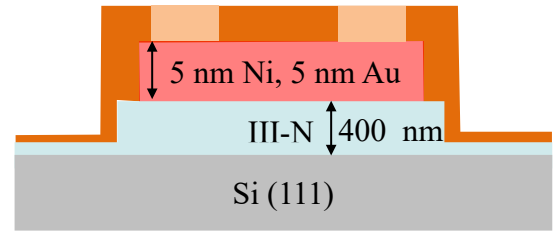
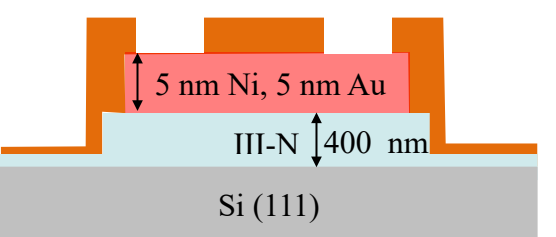
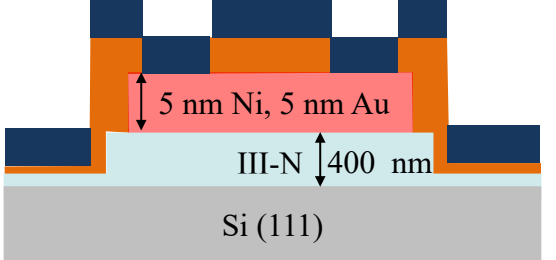
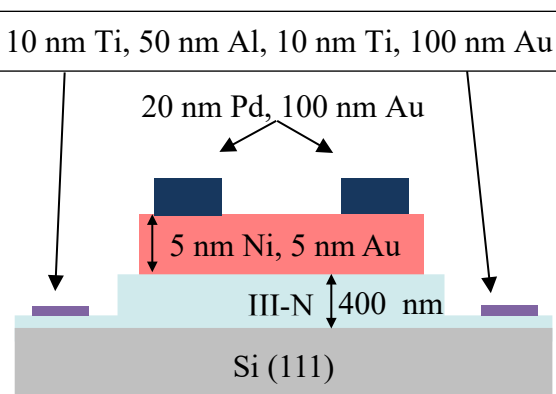
Process outline

Step	Process description	Cross-section after process
01	<p><i>III-nitride growth</i> Machine: III-N MOVPE LASPE Thickness: Si (111) substrate/ AlN (53 nm)/GaN (313 nm)/ 8x[InAlN/GaN (2.05/1.7)]/ GaN (20 nm)/ 3x[InGaN quantum well/GaN (2.6 nm/5nm)]/AlGaIn (20nm)/ GaN (150 nm) Size: 2" wafer</p>	
02	<p><i>p-type GaN activation</i> Machine: RTP AS-One Process: 750°C, 20' with N₂</p>	
f03	<p><i>Surface deoxidation and surface cleaning</i> Bath: HCL (16%) (90°C) (10') + BHF (10')</p>	
04	<p><i>Metal evaporation for p-type contacts</i> Machine: Alliance-Concept EVA-451 Process: e-beam physical vapor deposition Metals: 5 nm Ni, 5 nm Au</p>	
04	<p><i>Annealing p-type contacts</i> Machine: RTP AS-One Process: 550°C, 15' with 100% Oxygen</p>	
Patterning of semi-transparent metal contacts		

<p>05</p>	<p><i>Photolithography</i> Machine: Süss MicroTec Labspin 6BM Resist: AZ5214 (1.3 μm) Developer: MF319, 1'</p>	
<p>06</p>	<p><i>Oxygen plasma etching (removal of photoresist residues)</i> Machine: Z11 Tepla 300 Process: 50 mTorr O₂, 100W, 1'</p>	
<p>07</p>	<p><i>p-type metal contact etch</i> Machine: Gases: Ar RIE, O₂ cleaning Process: a. 8 mTorr Ar, 200W, 16x35" b. 50 mTorr O₂, 100W, 1'</p>	
<p>08</p>	<p><i>Photoresist strip</i> Remove: 1165 (N-Methylpyrrolidone) Acetone, ultrasonic bath</p>	
<p>Patterning of mesas (with same mask as before due to of a specific mask set)</p>		
<p>09</p>	<p><i>Photolithography</i> Machine: Resist: AZ5214 (1.3 μm – Dehydration 5'; 160°C – Enduction 42"; 5000 rpm; acceleration: 800 – Postbake 3'; 90 [°C]) Exposure: 2", hard contact Developer: MF319, 1'</p>	

<p>10</p>	<p><i>Oxygen plasma etching (removal of photoresist residues)</i> Machine: Z11 Tepla 300 Process: 50 mTorr O₂, 100W, 1'</p>	
<p>11</p>	<p><i>III-nitride etch</i> Machine: Sentech ICP-RIE SI 500 (III-V cleanroom) Gases: Cl-N₂ (90", 80 nm/min)</p>	
<p>12</p>	<p><i>Photoresist strip</i> Remove: 1165 (N-Methylpyrrolidone) Acetone, ultrasonic bath</p>	
<p>Lift-off for n-type metal contacts</p>		
<p>13</p>	<p><i>AZ5214 spin-coating and soft-bake</i> Machine: Resist: AZ5214 (1.3 μm – Dehydration 5'; 160°C – Enduction 42"; 5000 rpm; acceleration: 800 – Postbake 3'; 90 [°C])</p>	
<p>14</p>	<p><i>UV exposure, inversion and development</i> Exposure: 2", hard contact Inversion bake: 120°C, 1' Inversion exposure: 25", flood Developer: MF319, 1'</p>	

<p>15</p>	<p><i>Oxygen plasma etching (removal of photoresist residues)(optional)</i> Machine: Z11 Tepla 300 Process: 50 mTorr O₂, 100W, 1'</p>	
<p>16</p>	<p><i>Metal evaporation for n-type contacts</i> Machine: Alliance-Concept EVA-451 Process: e-beam physical vapor deposition Metals: 10 nm Ti, 50 nm Al, 10 nm Ti, 100 nm Au</p>	<p>10 nm Ti, 50 nm Al, 10 nm Ti, 100 nm Au</p> 
<p>17</p>	<p><i>Photoresist strip</i> Remover: 1165 (N-Methylpyrrolidone) Acetone, ultrasonic bath (optional)</p>	<p>10 nm Ti, 50 nm Al, 10 nm Ti, 100 nm Au</p> 
<p>Lift-off for p-type metal contacts</p>		
<p>18</p>	<p><i>AZ5214 spin-coating and soft-bake</i> Machine: Resist: AZ5214 (1.3 μm – Dehydration 5'; 160°C – Enduction 42'; 5000 rpm; acceleration: 800 – Postbake 3'; 90 [°C])</p>	 <p style="text-align: right;">n-type not represented</p>

<p>19</p>	<p><i>UV exposure, inversion and development</i> Exposure: 2", hard contact Inversion bake: 120°C, 1' Inversion exposure: 25", flood Developer: MF319, 1'</p>	 <p>n-type not represented</p>
<p>20</p>	<p><i>Oxygen plasma etching (removal of photoresist residues)</i> Machine: Z11 Tepla 300 Process: 50 mTorr O₂, 100W, 1'</p>	 <p>n-type not represented</p>
<p>21</p>	<p><i>Metal evaporation for n-type contacts</i> Machine: Alliance-Concept EVA-451 Process: e-beam physical vapor deposition Metals: 20 nm Pd, 100 nm Au</p>	 <p>n-type not represented</p>
<p>22</p>	<p><i>Photoresist strip</i> Remover: 1165 (N-Methylpyrrolidone) Acetone, ultrasonic bath</p>	

D Sample list

In this Appendix we provide a list of the samples investigated in the present thesis. All the samples listed here were grown on Si(111) substrates in the horizontal Aixtron 200/4 RF-S reactor (prefix "A") except for the reference LED structure C1069 grown on a sapphire substrate in a showerhead Aixtron 3 × 2" CCS reactor.

Table D.1: Sample list.

Sample	Chapter	Underlayer	Active region
A4286 aka. R	2, 3, 4	none	SQW 2.6 nm @ 17% In
A4287 aka. U	2, 3, 4	×16 InAlN/GaN SL	SQW 2.6 nm @ 17% In
A4289 aka. V	2, 3, 4	low-temperature GaN	SQW 2.6 nm @ 17% In
A3992	5	none	SQW 2.6 nm @ 17% In
A3993	5	none	×2 MQW 2.6 nm @ 17% In
A3994	5	×4 InAlN/GaN SL	SQW 2.6 nm @ 17% In
A4367	5	×8 InAlN/GaN SL	×3 MQW 2.6 nm @ 17% In
A4368	5	×8 InAlN/GaN SL	×3 MQW 2.6 nm @ 17% In
C1069	5	none	×3 MQW 2.3 nm

Bibliography

- [1] S. Nakamura *et al.*, “Candela-class high-brightness InGaN/AlGaN double-heterostructure blue-light-emitting diodes”, *Applied Physics Letters* **64**, 1687–1689 (1994).
- [2] S. Nakamura *et al.*, “Superbright Green InGaN Single-Quantum-Well-Structure Light-Emitting Diodes”, *Japanese Journal of Applied Physics* **34**, L1332–L1335 (1995).
- [3] S. D. Lester *et al.*, “High dislocation densities in high efficiency GaN-based light-emitting diodes”, *Applied Physics Letters* **66**, 1249–1251 (1995).
- [4] F. A. Ponce and D. P. Bour, “Nitride-based semiconductors for blue and green light-emitting devices”, *Nature* **386**, 351–359 (1997).
- [5] A. Herzog *et al.*, “High-Efficiency Zn-Diffused GaAs Electroluminescent Diodes”, *Journal of Applied Physics* **43**, 600–608 (1972).
- [6] R. J. Roedel *et al.*, “The Effect of Dislocations in $\text{Ga}_{1-x}\text{Al}_x\text{As} : \text{Si}$ Light-Emitting Diodes”, *Journal of The Electrochemical Society* **126**, 637–641 (1979).
- [7] S. Nakamura *et al.*, *The blue laser diode: the complete story*, 2nd updated and extended ed (Springer, Berlin ; New York, 2000).
- [8] S. Chichibu *et al.*, “Spontaneous emission of localized excitons in InGaN single and multi-quantum well structures”, *Applied Physics Letters* **69**, 4188–4190 (1996).
- [9] S. F. Chichibu *et al.*, “Origin of defect-insensitive emission probability in In-containing (Al,In,Ga)N alloy semiconductors”, *Nature Materials* **5**, 810–816 (2006).
- [10] M. Filoche *et al.*, “Localization landscape theory of disorder in semiconductors. I. Theory and modeling”, *Physical Review B* **95**, 144204 (2017).
- [11] A. M. Armstrong *et al.*, “Contribution of deep-level defects to decreasing radiative efficiency of InGaN/GaN quantum wells with increasing emission wavelength”, *Applied Physics Express* **7**, 032101 (2014).
- [12] C. Haller *et al.*, “GaN surface as the source of non-radiative defects in InGaN/GaN quantum wells”, *Applied Physics Letters* **113**, 111106 (2018).
- [13] Y. Chen *et al.*, “GaN buffer growth temperature and efficiency of InGaN/GaN quantum wells: The critical role of nitrogen vacancies at the GaN surface”, *Applied Physics Letters* **118**, 111102 (2021).

Bibliography

- [14] F. Piva *et al.*, “Defect incorporation in In-containing layers and quantum wells: experimental analysis via deep level profiling and optical spectroscopy”, *Journal of Physics D: Applied Physics* **54**, 025108 (2021).
- [15] A. M. Armstrong *et al.*, “Defect-reduction mechanism for improving radiative efficiency in InGaN/GaN light-emitting diodes using InGaN underlayers”, *Journal of Applied Physics* **117**, 134501 (2015).
- [16] C. Haller *et al.*, “InAlN underlayer for near ultraviolet InGaN based light emitting diodes”, *Applied Physics Express* **12**, 034002 (2019).
- [17] A. David *et al.*, “Review—The Physics of Recombinations in III-Nitride Emitters”, *ECS Journal of Solid State Science and Technology* **9**, 016021 (2020).
- [18] P. Lottigier *et al.*, “Investigation of the Impact of Point Defects in InGaN/GaN Quantum Wells with High Dislocation Densities”, *Nanomaterials* **13**, 2569 (2023).
- [19] S. Limpijumnong and W. R. L. Lambrecht, “Homogeneous Strain Deformation Path for the Wurtzite to Rocksalt High-Pressure Phase Transition in GaN”, *Physical Review Letters* **86**, 91–94 (2001).
- [20] I. Vurgaftman *et al.*, “Band parameters for III–V compound semiconductors and their alloys”, *Journal of Applied Physics* **89**, 5815–5875 (2001).
- [21] R. Butté and N. Grandjean, “Effects of Polarization in Optoelectronic Quantum Structures”, in *Polarization Effects in Semiconductors*, edited by C. Wood and D. Jena (Springer US, Boston, MA, 2008), pp. 467–511.
- [22] M. A. Herman *et al.*, *Epitaxy: Physical Principles and Technical Implementation*, edited by R. Hull *et al.*, Vol. 62, Springer Series in MATERIALS SCIENCE (Springer Berlin Heidelberg, Berlin, Heidelberg, 2004).
- [23] V. Fiorentini *et al.*, “Evidence for nonlinear macroscopic polarization in III–V nitride alloy heterostructures”, *Applied Physics Letters* **80**, 1204–1206 (2002).
- [24] A. Dadgar *et al.*, “MOVPE growth of GaN on Si(111) substrates”, *Journal of Crystal Growth* **248**, 556–562 (2003).
- [25] D. Zhu *et al.*, “Prospects of III-nitride optoelectronics grown on Si”, *Reports on Progress in Physics* **76**, 106501 (2013).
- [26] F. Semond, “Epitaxial challenges of GaN on silicon”, *MRS Bulletin* **40**, 412–417 (2015).
- [27] E. Feltin, “Hétéro-épitaxie de Niture de Gallium sur substrat de silicium (111) et applications”, fr, PhD thesis (Université de Nice - Sophia-Antipolis, Nice, France, Jan. 2003).
- [28] M. Fleck, *Burgers Vector and dislocations (screw and edge type)*, 2020.
- [29] C. G. Van De Walle, “Interactions of hydrogen with native defects in GaN”, en, *Physical Review B* **56**, R10020–R10023 (1997).
- [30] P. Bogusławski and J. Bernholc, “Doping properties of C, Si, and Ge impurities in GaN and AlN”, *Physical Review B* **56**, 9496–9505 (1997).

-
- [31] J. Neugebauer and C. G. Van De Walle, “Chemical trends for acceptor impurities in GaN”, *Journal of Applied Physics* **85**, 3003–3005 (1999).
- [32] H. Wang and A.-B. Chen, “Calculation of shallow donor levels in GaN”, *Journal of Applied Physics* **87**, 7859–7863 (2000).
- [33] C. Haller, “Elucidating the role of the InGaN UL in the efficiency of InGaN based light-emitting diodes”, PhD thesis (École Polytechnique Fédérale de Lausanne, 2019).
- [34] A. Polyakov *et al.*, “Deep traps in InGaN/GaN single quantum well structures grown with and without InGaN underlayers”, *Journal of Alloys and Compounds* **845**, 156269 (2020).
- [35] T. F. K. Weatherley, “The nanoscale impact of individual nonradiative point defects on InGaN/GaN quantum wells”, PhD thesis (École Polytechnique Fédérale de Lausanne, 2023).
- [36] J. Wu *et al.*, “Temperature dependence of the fundamental band gap of InN”, *Journal of Applied Physics* **94**, 4457–4460 (2003).
- [37] M. Feneberg *et al.*, “Sharp bound and free exciton lines from homoepitaxial AlN”, *physica status solidi (a)* **208**, 1520–1522 (2011).
- [38] M. Leroux *et al.*, “Temperature quenching of photoluminescence intensities in undoped and doped GaN”, *Journal of Applied Physics* **86**, 3721–3728 (1999).
- [39] K. Kornitzer *et al.*, “Photoluminescence and reflectance spectroscopy of excitonic transitions in high-quality homoepitaxial GaN films”, *Physical Review B* **60**, 1471–1473 (1999).
- [40] Y. P. Varshni, “Temperature dependence of the energy gap in semiconductors”, *Physica* **34**, 149–154 (1967).
- [41] E. Rosencher and B. Vinter, “Quantum Mechanics of the Electron”, in *Optoelectronics* (Cambridge University Press, Cambridge, 2004), pp. 1–28.
- [42] M. Leroux *et al.*, “Quantum confined Stark effect due to built-in internal polarization fields in (Al,Ga)N/GaN quantum wells”, *Physical Review B* **58**, R13371–R13374 (1998).
- [43] N. Grandjean *et al.*, “Built-in electric-field effects in wurtzite AlGaIn/GaN quantum wells”, *Journal of Applied Physics* **86**, 3714–3720 (1999).
- [44] A. Hangleiter, “Optical properties of nitride heterostructures”, *physica status solidi (c)*, 1816–1834 (2003).
- [45] M. Glauser, “InGaIn alloys and heterostructures: impact of localization effects on light-matter interaction in planar microcavities”, PhD thesis (École Polytechnique Fédérale de Lausanne, 2014).
- [46] M. Piccardo *et al.*, “Localization landscape theory of disorder in semiconductors. II. Urbach tails of disordered quantum well layers”, *Physical Review B* **95**, 144205 (2017).
- [47] B. A. Ruzicka *et al.*, “Ambipolar diffusion of photoexcited carriers in bulk GaAs”, *Applied Physics Letters* **97**, 262119 (2010).

Bibliography

- [48] P. Ščajev *et al.*, “Carrier dynamics in bulk GaN”, *Journal of Applied Physics* **111**, 023702 (2012).
- [49] O. Brandt *et al.*, “Carrier Diffusion in Ga N : A Cathodoluminescence Study. II. Ambipolar versus Exciton Diffusion”, *Physical Review Applied* **17**, 024018 (2022).
- [50] G. Callsen *et al.*, “Probing Alloy Formation Using Different Excitonic Species: The Particular Case of InGaN”, *Physical Review X* **9**, 031030 (2019).
- [51] Y. Narukawa *et al.*, “Recombination dynamics of localized excitons in In_{0.20}Ga_{0.80}N-In_{0.05}Ga_{0.95}N multiple quantum wells”, *Physical Review B* **55**, R1938–R1941 (1997).
- [52] A. David, “Long-Range Carrier Diffusion in (In , Ga) N Quantum Wells and Implications from Fundamentals to Devices”, *Physical Review Applied* **15**, 054015 (2021).
- [53] C. Becht *et al.*, “Diffusion Analysis of Charge Carriers in InGaN/GaN Heterostructures by Microphotoluminescence”, *physica status solidi (b)*, 2200565 (2023).
- [54] M. Sarzyński *et al.*, “Lateral Control of Indium Content and Wavelength of III–Nitride Diode Lasers by Means of GaN Substrate Patterning”, *Applied Physics Express* **5**, 021001 (2012).
- [55] W. Shockley and W. T. Read, “Statistics of the Recombinations of Holes and Electrons”, *Physical Review* **87**, 835–842 (1952).
- [56] R. N. Hall, “Electron-Hole Recombination in Germanium”, *Physical Review* **87**, 387–387 (1952).
- [57] A. Alkauskas *et al.*, “First-principles theory of nonradiative carrier capture via multiphonon emission”, *Physical Review B* **90**, 075202 (2014).
- [58] C. E. Dreyer *et al.*, “Gallium vacancy complexes as a cause of Shockley-Read-Hall recombination in III-nitride light emitters”, *Applied Physics Letters* **108**, 141101 (2016).
- [59] S. M. Sze and K. K. Ng, *Physics of semiconductor devices*, Third edition (Wiley-Interscience, Hoboken, NJ, 2007).
- [60] C. H. Henry and D. V. Lang, “Nonradiative capture and recombination by multiphonon emission in GaAs and GaP”, *Physical Review B* **15**, 989–1016 (1977).
- [61] A. Einstein, “Strahlungs-Emission und Absorption nach der Quantentheorie”, *Deutsche Physikalische Gesellschaft* **18**, ADS Bibcode: 1916DPhyG..18..318E, 318–323 (1916).
- [62] G. Lasher and F. Stern, “Spontaneous and Stimulated Recombination Radiation in Semiconductors”, *Physical Review* **133**, A553–A563 (1964).
- [63] G. W. 'T Hooft and C. Van Opdorp, “Temperature dependence of interface recombination and radiative recombination in (Al, Ga)As heterostructures”, *Applied Physics Letters* **42**, 813–815 (1983).
- [64] Y. Arakawa *et al.*, “Recombination lifetime of carriers in GaAs-GaAlAs quantum wells near room temperature”, *Applied Physics Letters* **46**, 519–521 (1985).

- [65] T. Matsusue and H. Sakaki, "Radiative recombination coefficient of free carriers in GaAs-AlGaAs quantum wells and its dependence on temperature", *Applied Physics Letters* **50**, 1429–1431 (1987).
- [66] L. V. Asryan, "Spontaneous radiative recombination and nonradiative Auger recombination in quantum-confined heterostructures", *Quantum Electronics* **35**, 1117–1120 (2005).
- [67] S. Chatterjee *et al.*, "Excitonic Photoluminescence in Semiconductor Quantum Wells: Plasma versus Excitons", *Physical Review Letters* **92**, 067402 (2004).
- [68] S. W. Koch *et al.*, "Semiconductor excitons in new light", *Nature Materials* **5**, 523–531 (2006).
- [69] W. Chow *et al.*, "Microscopic theory of optical nonlinearities and spontaneous emission lifetime in group-III nitride quantum wells", *Physical Review B* **60**, 1947–1952 (1999).
- [70] J. Hader *et al.*, "Interband Transitions in InGaN Quantum Wells", in *Nitride Semiconductor Devices: Principles and Simulation*, edited by J. Piprek, 1st ed. (Wiley, Jan. 2007), pp. 145–167.
- [71] M. Shahmohammadi *et al.*, "Enhancement of Auger recombination induced by carrier localization in InGaN/GaN quantum wells", *Physical Review B* **95**, 125314 (2017).
- [72] A. David and M. J. Grundmann, "Influence of polarization fields on carrier lifetime and recombination rates in InGaN-based light-emitting diodes", *Applied Physics Letters* **97**, 033501 (2010).
- [73] E. Kioupakis *et al.*, "Interplay of polarization fields and Auger recombination in the efficiency droop of nitride light-emitting diodes", *Applied Physics Letters* **101**, 231107 (2012).
- [74] A. David *et al.*, "Compensation between radiative and Auger recombinations in III-nitrides: The scaling law of separated-wavefunction recombinations", *Applied Physics Letters* **115**, 193502 (2019).
- [75] W. Liu *et al.*, "Impact of defects on Auger recombination in *c*-plane InGaN/GaN single quantum well in the efficiency droop regime", *Applied Physics Letters* **116**, 222106 (2020).
- [76] D. Ochoa *et al.*, "Device simultaneous determination of the source and cavity parameters of a microcavity light-emitting diode", *Journal of Applied Physics* **85**, 2994–2996 (1999).
- [77] E. F. Schubert, *Light-emitting diodes*, eng, 2nd ed (Cambridge university press, Cambridge, 2006).
- [78] W. Shockley, "The Theory of *p-n* Junctions in Semiconductors and *p-n* Junction Transistors", *Bell System Technical Journal* **28**, 435–489 (1949).
- [79] X. Wu *et al.*, "Dislocation generation in GaN heteroepitaxy", *Journal of Crystal Growth* **189-190**, 231–243 (1998).

Bibliography

- [80] T. Hino *et al.*, “Characterization of threading dislocations in GaN epitaxial layers”, *Applied Physics Letters* **76**, 3421–3423 (2000).
- [81] N. Yamamoto *et al.*, “Cathodoluminescence characterization of dislocations in gallium nitride using a transmission electron microscope”, *Journal of Applied Physics* **94**, 4315–4319 (2003).
- [82] M. Albrecht *et al.*, “Nonradiative recombination at threading dislocations in n-type GaN: Studied by cathodoluminescence and defect selective etching”, *Applied Physics Letters* **92**, 231909 (2008).
- [83] M. A. Moram *et al.*, “On the origin of threading dislocations in GaN films”, *Journal of Applied Physics* **106**, 073513 (2009).
- [84] G. Naresh-Kumar *et al.*, “Coincident Electron Channeling and Cathodoluminescence Studies of Threading Dislocations in GaN”, *Microscopy and Microanalysis* **20**, 55–60 (2014).
- [85] F. C.-P. Massabuau *et al.*, “Optical and structural properties of dislocations in InGaN”, *Journal of Applied Physics* **125**, 165701 (2019).
- [86] N. Sharma *et al.*, “Chemical mapping and formation of V-defects in InGaN multiple quantum wells”, *Applied Physics Letters* **77**, 1274–1276 (2000).
- [87] D. Cherns *et al.*, “Edge and screw dislocations as nonradiative centers in InGaN/GaN quantum well luminescence”, *Applied Physics Letters* **78**, 2691–2693 (2001).
- [88] K. Watanabe *et al.*, “Formation and structure of inverted hexagonal pyramid defects in multiple quantum wells InGaN/GaN”, *Applied Physics Letters* **82**, 718–720 (2003).
- [89] S. J. Henley and D. Cherns, “Cathodoluminescence studies of threading dislocations in InGaN/GaN as a function of electron irradiation dose”, *Journal of Applied Physics* **93**, 3934–3939 (2003).
- [90] S. Tomiya *et al.*, “Atomic scale characterization of GaInN/GaN multiple quantum wells in V-shaped pits”, *Applied Physics Letters* **98**, 181904 (2011).
- [91] H. Takahashi *et al.*, “Effect of Intentionally Formed ‘V-Defects’ on the Emission Efficiency of GaInN Single Quantum Well”, *Japanese Journal of Applied Physics* **39**, L569–L571 (2000).
- [92] A. Hangleiter *et al.*, “Suppression of Nonradiative Recombination by V-Shaped Pits in GaInN / GaN Quantum Wells Produces a Large Increase in the Light Emission Efficiency”, *Physical Review Letters* **95**, 127402 (2005).
- [93] C. Netzel *et al.*, “Emission and recombination characteristics of Ga_{1-x}In_xN / GaN quantum well structures with nonradiative recombination suppression by V-shaped pits”, *PHYSICAL REVIEW B* **76**, 155322 (2007).
- [94] N. Okada *et al.*, “Controlling potential barrier height by changing V-shaped pit size and the effect on optical and electrical properties for InGaN/GaN based light-emitting diodes”, *Journal of Applied Physics* **117**, 025708 (2015).

- [95] A. Bojarska-Cieślińska *et al.*, “Role of dislocations in nitride laser diodes with different indium content”, *Scientific Reports* **11**, 21 (2021).
- [96] S. Usami *et al.*, “Correlation between dislocations and leakage current of p-n diodes on a free-standing GaN substrate”, *Applied Physics Letters* **112**, 182106 (2018).
- [97] J. Ewing *et al.*, “Influence of Superlattice Structure on V-Defect Distribution, External Quantum Efficiency and Electroluminescence for Red InGaN Based μ LEDs on Silicon”, *Crystals* **12**, 1216 (2022).
- [98] Z. Quan *et al.*, “Roles of V-shaped pits on the improvement of quantum efficiency in InGaN/GaN multiple quantum well light-emitting diodes”, *Journal of Applied Physics* **116**, 183107 (2014).
- [99] S. Zhou *et al.*, “The effect of nanometre-scale V-pits on electronic and optical properties and efficiency droop of GaN-based green light-emitting diodes”, *Scientific Reports* **8**, 11053 (2018).
- [100] C.-H. Ho *et al.*, “Efficiency and Forward Voltage of Blue and Green Lateral LEDs with V-shaped Defects and Random Alloy Fluctuation in Quantum Wells”, *Physical Review Applied* **17**, 014033 (2022).
- [101] H. Amano *et al.*, “Metalorganic vapor phase epitaxial growth of a high quality GaN film using an AlN buffer layer”, *Applied Physics Letters* **48**, 353–355 (1986).
- [102] T. F. K. Weatherley *et al.*, “Imaging Nonradiative Point Defects Buried in Quantum Wells Using Cathodoluminescence”, *Nano Letters* **21**, 5217–5224 (2021).
- [103] E. Oveisi, “Three-Dimensional STEM Imaging of Dislocations”, fr, PhD thesis (École Polytechnique Fédérale de Lausanne, 2015).
- [104] E. Oveisi *et al.*, “Insights into image contrast from dislocations in ADF-STEM”, *Ultramicroscopy* **200**, 139–148 (2019).
- [105] R. Butté *et al.*, “Optical absorption edge broadening in thick InGaN layers: Random alloy atomic disorder and growth mode induced fluctuations”, *Applied Physics Letters* **112**, 032106 (2018).
- [106] E. Berkowicz *et al.*, “Measured and calculated radiative lifetime and optical absorption of $\text{In}_x\text{Ga}_{1-x}\text{N}/\text{GaN}$ quantum structures”, *Physical Review B* **61**, 15 (2000).
- [107] Y.-H. Cho *et al.*, ““S-shaped” temperature-dependent emission shift and carrier dynamics in InGaN/GaN multiple quantum wells”, *Applied Physics Letters* **73**, 1370–1372 (1998).
- [108] B. E. A. Saleh and M. C. Teich, *Fundamental of Photonics*, 3rd ed. (Wiley, 2019).
- [109] K. Purvis *et al.*, “New Activity for Instrumental Analysis: Laser Beam Profiling”, *J. Chem. Educ.*, 5 (2019).
- [110] C. A. Hurni *et al.*, “Bulk GaN flip-chip violet light-emitting diodes with optimized efficiency for high-power operation”, *Applied Physics Letters* **106**, 031101 (2015).

Bibliography

- [111] A. David *et al.*, “Thermal droop in high-quality InGaN LEDs”, *Applied Physics Letters* **115**, 223502 (2019).
- [112] H.-M. Solowan *et al.*, “Direct Observation of Charge Carrier Diffusion and Localization in an InGaN Multi Quantum Well”, *Japanese Journal of Applied Physics* **52**, 08JK07 (2013).
- [113] U. Jahn *et al.*, “Carrier Diffusion in Ga N : A Cathodoluminescence Study. I. Temperature-Dependent Generation Volume”, *Physical Review Applied* **17**, 024017 (2022).
- [114] S. Finot *et al.*, “Surface Recombinations in III-Nitride Micro-LEDs Probed by Photon-Correlation Cathodoluminescence”, *ACS Photonics* **9**, 173–178 (2022).
- [115] C. Haller *et al.*, “Burying non-radiative defects in InGaN underlayer to increase InGaN/-GaN quantum well efficiency”, *Applied Physics Letters* **111**, 262101 (2017).
- [116] Y. Zhang *et al.*, “Photonic crystal nanobeam lasers”, *Appl. Phys. Lett.* **97**, 051104 (2010).
- [117] S. Strauf *et al.*, “Self-Tuned Quantum Dot Gain in Photonic Crystal Lasers”, *Physical Review Letters* **96**, 127404 (2006).
- [118] S. T. Jagsch *et al.*, “A quantum optical study of thresholdless lasing features in high- β nitride nanobeam cavities”, *Nature Communications* **9**, 564 (2018).
- [119] N. V. Triviño *et al.*, “Continuous Wave Blue Lasing in III-Nitride Nanobeam Cavity on Silicon”, *Nano Letters* **15**, 1259–1263 (2015).
- [120] Y. Gong *et al.*, “Nanobeam photonic crystal cavity quantum dot laser”, *Optics Express* **18**, 8781 (2010).
- [121] G. Shambat *et al.*, “Single-Cell Photonic Nanocavity Probes”, *Nano Letters* **13**, 4999–5005 (2013).
- [122] I. M. Rousseau, “III-Nitride Semiconductor Photonic Nanocavities on Silicon”, PhD thesis (École Polytechnique Fédérale de Lausanne, 2018).
- [123] V. Triviño, “GaN-based photonic crystal cavities on silicon for visible and near infrared applications”, PhD thesis (École Polytechnique Fédérale de Lausanne, 2015).
- [124] P. Lalanne and J. P. Hugonin, “Bloch-wave engineering for high-Q, small-V microcavities”, *IEEE Journal of Quantum Electronics* **39**, 9 (2003).
- [125] M. W. McCutcheon and M. Loncar, “Design of a silicon nitride photonic crystal nanocavity with a Quality factor of one million for coupling to a diamond nanocrystal”, *Optics Express* **16**, 19136 (2008).
- [126] S. Vicknesh *et al.*, “Fabrication of deeply undercut GaN-based microdisk structures on silicon platforms”, *Applied Physics Letters* **90**, 071906 (2007).
- [127] D. Parrain *et al.*, “Origin of optical losses in gallium arsenide disk whispering gallery resonators”, *Optics Express* **23**, 19656 (2015).
- [128] H. Benisty *et al.*, “Impact of planar microcavity effects on light extraction-Part II: selected exact simulations and role of photon recycling”, *IEEE Journal of Quantum Electronics* **34**, 1632–1643 (1998).

- [129] I. Schnitzer *et al.*, “Ultrahigh spontaneous emission quantum efficiency, 99.7% internally and 72% externally, from AlGaAs/GaAs/AlGaAs double heterostructures”, *Applied Physics Letters* **62**, 131–133 (1993).
- [130] I. Schnitzer *et al.*, “30% external quantum efficiency from surface textured, thin-film light-emitting diodes”, *Applied Physics Letters* **63**, 2174–2176 (1993).
- [131] A. David, “Surface-Roughened Light-Emitting Diodes: An Accurate Model”, *Journal of Display Technology*, 16 (2013).
- [132] E. Matioli *et al.*, “High extraction efficiency light-emitting diodes based on embedded air-gap photonic-crystals”, *Applied Physics Letters* **96**, 031108 (2010).
- [133] E. F. Schubert *et al.*, “Resonant cavity light-emitting diode”, *Applied Physics Letters* **60**, 921–923 (1992).
- [134] A. Dutta *et al.*, “High-brightness, AlGaInP-based, visible light-emitting diode for efficient coupling with POF”, *IEEE Photonics Technology Letters* **7**, 1134–1136 (1995).
- [135] A. Dutta *et al.*, “High brightness and reliable AlGaInP-based light-emitting diode for POF data links”, *IEEE Photonics Technology Letters* **9**, 1567–1569 (1997).
- [136] R. H. Horng *et al.*, “AlGaInP light-emitting diodes with mirror substrates fabricated by wafer bonding”, *Applied Physics Letters* **75**, 3054–3056 (1999).
- [137] C. Hums *et al.*, “Fabry-perot effects in ingan/gan heterostructures on si-substrate”, *Journal of Applied Physics* **101**, 033113 (2007).
- [138] P. Bienstmann *et al.*, *CAMFR*, 2012.
- [139] J.-K. Ho *et al.*, “Low-resistance ohmic contacts to p-type GaN”, 4 (1999).
- [140] B. Liu *et al.*, “Effects of a Ni cap layer on transparent Ni/Au ohmic contacts to p-GaN”, *Journal of Vacuum Science & Technology B: Microelectronics and Nanometer Structures* **20**, 1394 (2002).
- [141] Y. Lin *et al.*, “InGaN/GaN light emitting diodes with Ni/Au, Ni/ITO and ITO p-type contacts”, *Solid-State Electronics* **47**, 849–853 (2003).



Pierre Lottigier

Physicist Engineer

PROFILE

- Passion for Light & Photonics
- Collaborative Team-Player
- Results-Driven

CONTACT

 Rue de l'Industrie 26
1030 Bussigny

+41 78 212 95 69

 pierreltg@gmail.com

French
16.6.1995
Driving licence B

EXPERIENCE

2019 – 2024 | Doctoral Researcher

EPFL, Advanced Semiconductors for Photonics and Electronics, Lausanne

- * Identified a way to enhance light emission in highly defective semiconductor materials, explaining their nanoscale structure
- * Designed and fabricated optimized photonic structures on Si

2019 – 2024 | Teaching Assistant, Mechanics & Thermodynamics

EPFL, Lausanne

- * Received an award for outstanding teaching competences

2016 – 2019 | Engineering Apprentice in Laser Science

Ecole Polytechnique, Laboratoire de Physique des Plasmas, Paris

- * Developed high-precision lasers for gas and plasma sensing

EDUCATION

2019 – 2024 | PhD in Photonics and Semiconductor Science

EPFL, Lausanne

- * Courses: Photovoltaics, MOEMS, Micro- & Nanooptics

2018 – 2019 | Master in Fundamental Physics

Université Paris-Saclay, France

- * Laser – Optics – Matter
- * Nonlinear Optics, Nanophotonics, Quantum Optics

2016 – 2019 | Master in Engineering: Optics and Photonics

Institut d'Optique Graduate School ParisTech, France

French Grandes-Ecoles Engineer diploma

- * Optical Systems Design, Fourier & Beam Optics, Radiometry
- * Electronics Prototyping and Computer Science

SKILLS

- * Light-Matter Interaction
- * Semiconductor Science
- * Laser Physics and Spectroscopy
- * Extensive Experience in Nano- and Micro- Photonic Device Design and Simulation
- * Extensive Experience in Clean-Room Fabrication
- * Proficiency in Electron Microscopy Techniques
- * Autonomous and Collaborative Work Style
- * Excellent Communication Abilities

LANGUAGES

French	Native
German	Bilingual
English	Advanced C1+

SOFTWARES

Python, MatLab, Ansys Lumerical, gdsSpy, KLayout, L-Edit IC, GenlSys BEAMER
Origin Pro, Adobe Illustrator, Latex, Microsoft Office

INTERESTS

Sports	Climbing, Sailing Teacher, Yoga
Alpinism	Swiss Alpine Club Group Leader
Paragliding	Swiss Pilot License
Literature	Personal development

Publications

Posters

A. S. Morillo-Candas, B. L. M Klarenaar, P. Lottigier, J.-P. Booth, V. Guerra, C. Drag and O. Guaitella. O atom kinetics in CO₂ plasmas, Cold Plasma day of LPP (Laboratoire de Physique des Plasmas), Paris, France, May 2017

P. Lottigier and C. Drag. Wavelength selection in a pulsed Ti:Sapphire laser for high resolution plasma spectroscopy, Congress of the French Optical Society, Toulouse, France, July 2018

C. Drag, C. Blondel and P. Lottigier. Single-mode nanosecond Ti:sapphire laser for high-resolution two-photon absorption laser-induced fluorescence, PALM Labex poster day, Palaiseau, France, February 2019

Articles

P. Lottigier, A. Jucha, L. Cabaret, C. Blondel and C. Drag. Single-mode scannable nanosecond Ti:Sapphire laser for high resolution Two-photon Absorption Laser Induced Fluorescence (TALIF), *Appl. Phys. B* **125**(1), 14 (2019) <https://doi.org/10.1007/s00340-018-7124-5>

P. Lottigier, D. M. Di Paola, D. T. L. Alexander, T. F. K. Weatherley, P. Saenz-De-Santa-María-Modroño, D. Chen, G. Jacopin, J.-F. Carlin, R. Butté, N. Grandjean, Investigation of the impact of point defects in InGa_N/Ga_N quantum wells with high dislocation densities. *Nanomaterials* **13**(18), 2569 (2023) <https://doi.org/10.3390/nano13182569>

Conferences

C. Drag, P. Lottigier, D. Marinov, C. Blondel, J.-P. Booth and O. Guaitella. Single-mode nanosecond Ti:Sapphire laser for high resolution Two-photon Absorption Laser Induced- Fluorescence, Conference on Lasers and Electro-Optics Europe CLEO, Munich, June 25-29 2017

C. Drag, P. Lottigier, D. Marinov, C. Blondel, J.-P. Booth and O. Guaitella. High resolution Two-photon Absorption Laser-Induced Fluorescence (TALIF) with a single-mode nanosecond Ti:Sapphire laser, 18th Laser Aided Plasma Diagnostics conference, Prague, September 24-28 2017

P. Lottigier, D. M. Di Paola, D. T. L. Alexander, Y. Wang, D. Chen, T. F. K. Weatherley, J.-F. Carlin, R. Butté, N. Grandjean. Impact of point defects on the efficiency of InGa_N/Ga_N quantum wells grown on Ga_N-on-Si epilayers with high dislocation density, International Workshop on Nitride Semiconductors, Berlin, Germany, October 09-14 2022

P. Lottigier, T. F. K. Weatherley, D. T. L. Alexander, D. M. Di Paola, Y. Wang, P. Saenz-De-Santa-María-Modroño, G. Jacopin, J.-F. Carlin, N. Grandjean. Using cathodoluminescence for nonradiative recombination path analysis in InGa_N/Ga_N QWs on Si(111) substrate, Cathodoluminescence and Electron Beam Induced Current of Semiconductor Nanostructures, Grenoble, France, March 22-24 2023

P. Lottigier, T. F. K. Weatherley, D. T. L. Alexander, D. M. Di Paola, P. Saenz-De-Santa-María-Modroño, G. Jacopin, J.-F. Carlin, N. Grandjean, Nanoscale investigation of non-radiative recombination paths in InGa_N/Ga_N quantum wells, International Conference on Nitride Semiconductors, Fukuoka, Japan, November 12-17 2023